

2015

# Vibrational spectroscopy of an optogenetic rhodopsin: a biophysical study of molecular mechanisms

---

<https://hdl.handle.net/2144/16343>

*Boston University*

BOSTON UNIVERSITY  
GRADUATE SCHOOL OF ARTS AND SCIENCES

Dissertation

**Vibrational Spectroscopy of Optogenetic Rhodopsins:  
A Biophysical Study of Molecular Mechanisms**

by

**John I. Ogren**

B.S., University of New Mexico, 2008  
M.A., Boston University, 2010

Submitted in partial fulfillment of the  
requirements for the degree of  
Doctor of Philosophy  
2015

Approved by

First Reader

---

Kenneth J. Rothschild, Ph.D.  
Professor of Physics  
Boston University

Second Reader

---

Shyamsunder Erramilli, Ph.D.  
Professor of Physics  
Boston University

*For my family, without whom I would not strive.*

*For my friends, without whom I would not persevere.*

*For Maddie, without whom I could not thrive.*



## Acknowledgments

My profound thanks and admiration go to my advisor, Prof. Kenneth J. Rothschild. I truly appreciate the patience and tenacity it must have taken to turn me into a Biophysicist, no easy task, to be sure. I have learned an immeasurable amount from you, my sincerest thanks.

None of my work would have been possible without the other members of the Biophysics community at BU. First among these is Dr. Sergey Mamaev who, singlehandedly produced the vast majority of the samples represented as data in this thesis. His knowledge is encyclopedic, his skills are razor sharp, and his stories are legendary. Thank you to the other members of the MBL during my tenure; Dr. Joel Kralj, Dr. Jason Amsden, Dr. Erica Saint Clair, Dan Russano, and Adrian Yi. Thanks are also due to a true mentor, Prof. Shyam Erramilli, as well as a good friend, Joe Hardcastle.

I must also thank the many additional scientists and experts with whom I have had the pleasure of working. Namely, Dr. Justin Torgerson and Dr. Martin Schauer provided my first opportunity to perform research, a difficult task for them but an absolutely essential experience for me. My time at Los Alamos shaped my mind and caudified my curiosity. In addition, my work at SLAC with Dr. Matt Coleman and Dr. Mark Hunter led by Dr. Matthias Frank introduced me to new methods and motivations. The late nights and early mornings preparing samples, believe it or not, are very fond memories. And to my collaborators in Texas, especially Dr. Spudich, thank you so much for your time and effort working with me to publish my results. You are an incredible resource for a young scientist trying to understand a very mature field.

Finally, to all the friends I've made at BU and in Boston, wherever we all end up, my everlasting gratitude for talking, cooking, drinking, living, working, and being with me.

**Vibrational Spectroscopy of an Optogenetic Rhodopsin:  
A Biophysical Study of Molecular Mechanisms**

(Order No.                    )

**John I. Ogren**

Boston University Graduate School of Arts and Sciences, 2015

Major Professor: Kenneth J. Rothschild, Professor of Physics

ABSTRACT

In this dissertation, the membrane protein channelrhodopsin-1 from the green flagellate algae *Chlamydomonas agustae* (*CaChR1*) is studied using a variety of spectroscopic techniques developed in the Rothschild Molecular Biophysics Laboratory at Boston University.

Over the last decade, channelrhodopsins have proven to be effective optogenetic tools due to their ability to function as light-gated ion channels when expressed in neurons. This ability allows neuroscientists to optically activate an inward directed photocurrent which depolarizes the neuronal membranes and triggers an action potential. Although a variety of channelrhodopsins with different properties have been used, the underlying mechanisms of channelrhodopsin functionality is not yet fully understood.

The protein studied here has several advantageous properties compared to the more extensively studied channelrhodopsin-2 from *Chlamydomonas reinhardtii* including a red shifted visible absorption and slower light inactivation despite having a lower channel current. Elucidating the internal molecular mechanisms underlying the function of *CaChR1* provides critical insight into the large class of channelrhodopsin proteins leading toward improved bioengineering for specific optogenetic applications.

Here near-IR pre-resonance Raman spectroscopy of *CaChR1* provides information on the structure of the unphotolyzed ( $P_0$ ) retinal chromophore, the Schiff base protonation state, and presence of carboxylic acid residues interacting with the Schiff base. Low-temperature

FTIR difference spectroscopy combined with site-directed mutagenesis and isotope labeling provide information on changes occurring in the retinal chromophore and protein during the primary phototransition ( $P_0 \rightarrow P_1$ ). This includes information about changes involving protonation state of binding-pocket residues, protein backbone structure, and internal water molecules. Further experiments combining low-temperature and time-resolved FTIR-difference spectroscopy reveal additional information about structural changes during the transition from the unphotolyzed state to the active (open channel) state of the protein ( $P_0 \rightarrow P_2$ ).

This work has resulted in an initial model that describes key proton transfer events which occur between the Schiff base and carboxylic acid residues inside the active site of *CaChR1*. The model raises the possibility that ion channel gating and ion specificity is regulated by the protonation changes of two key residues (Glu 169 and Asp299) located near the Schiff base.

## Contents

<b>1</b>	<b>Introduction</b>	<b>1</b>
1.1	The Type I Opsin Family . . . . .	1
1.2	Light Driven Proton Pumps: Bacteriorhodopsin from <i>Halobacterium Sali-</i> <i>narium</i> as the Standard Model for Type I Opsins . . . . .	1
1.2.1	The Bacteriorhodopsin Photocycle . . . . .	2
1.2.2	Sensory Rhodopsin II from <i>Natronobacterium pharaonis</i> . . . . .	7
1.3	Channelrhodopsins . . . . .	8
1.4	Theory of Vibrational Spectroscopy . . . . .	9
1.4.1	Absorption Cross Section . . . . .	9
1.4.2	The Beer-Lambert Law . . . . .	13
1.4.3	Raman Scattering . . . . .	15
<b>2</b>	<b>Materials and Methods: Biophysical Spectroscopy</b>	<b>20</b>
2.1	Microbial-Rhodopsin Expression, Purification, and Reconstitution . . . . .	20
2.1.1	Channelrhodopsin Expression and Purification . . . . .	20
2.2	FTIR Spectroscopy and Difference Spectroscopy . . . . .	21
2.2.1	Time Resolved FTIR Difference Spectroscopy . . . . .	23
2.2.2	Low Temperature FTIR Difference Spectroscopy . . . . .	26
2.3	Near-Resonance Raman Spectroscopy . . . . .	28
2.4	UV-Vis Laser Induced Transient Absorption Spectroscopy . . . . .	30
<b>3</b>	<b>The P<sub>0</sub> state of CaChR1: Retinal Conformation, Schiff Base Protonation, and the Counterion Complex</b>	<b>35</b>
3.1	Raman Spectroscopy of the CaChR1 P <sub>0</sub> unphotolyzed state. . . . .	35
3.1.1	Similarity of the Raman Spectra of CaChR1, BR, and NPSRII . . . . .	35
3.1.2	Assignment of the CaChR1 Ethylenic C=C Stretching Vibration . . . . .	40

3.1.3	Assignment of the <i>CaChR1</i> SB C=N Stretching Mode and Strength of Hydrogen Bonding . . . . .	43
3.1.4	Effects of pH and Anions on the Resonance Raman Spectrum of <i>CaChR1</i> . . . . .	44
3.1.5	The Effects of Anion Exchange on the PSB . . . . .	46
3.1.6	Effects of Substitution of Glu169 and Asp299 . . . . .	47
3.2	Conclusions from Raman Studies . . . . .	49
3.2.1	Light-Adapted <i>CaChR1</i> has an All- <i>Trans</i> Retinal Composition Similar to That of BR and <i>NpSR11</i> in Contrast to That of <i>CrChR2</i> . . .	50
3.2.2	The Schiff Base Has Hydrogen Bonding Stronger Than That of BR .	51
3.2.3	Glu169 Exists in a Neutral Form at Neutral pH . . . . .	52
3.2.4	Asp299 Serves as the Predominant SB Counterion over a Broad pH Range . . . . .	53
<b>4</b>	<b>The P<sub>0</sub> to P<sub>1</sub> phototransition: The Initial Photoproduct and the Assignment of Chromophore, Protein, and Water Vibrations.</b>	<b>56</b>
4.1	FTIR Difference Spectroscopy of <i>CaChR1</i> at 80 K . . . . .	56
4.1.1	The Primary Phototransition of <i>CaChR1</i> Involves all- <i>trans</i> to 13- <i>cis</i> chromophore isomerization . . . . .	57
4.1.2	Assignment of the Schiff Base C=N Stretch and Amide I Bands . . .	60
4.1.3	Evidence for Changes in the Amide II Protein Mode in the Primary Phototransition of <i>CaChR1</i> . . . . .	64
4.1.4	Detection of Bands in the Carboxylic Acid C=O Stretching Region .	67
4.1.5	Detection of Weakly Hydrogen Bonded Internal Water Molecules . .	69
4.1.6	Detection of Cysteine Vibrations . . . . .	72
4.1.7	Effects of Mutations at Glu169 and Asp299 in the Carboxylic Acid C=O Stretch Region . . . . .	73
4.1.8	Effects of Mutations at Glu169 and Asp299 in other Spectral Regions	76

4.2	Conclusions from Low-Temperature FTIR Studies of <i>CaChR1</i> . . . . .	78
4.2.1	Chromophore Structural Changes in the primary phototransition of <i>CaChR1</i> are more similar to BR than to <i>CrChR2</i> . . . . .	79
4.2.2	Structural changes which involve the protein backbone are different in <i>CaChR1</i> , <i>CrChR2</i> , and BR . . . . .	80
4.2.3	Structural changes of weakly hydrogen bonded internal water molecules are different in <i>CaChR1</i> and <i>CrChR2</i> . . . . .	80
4.2.4	Asp299 protonates during the primary phototransition . . . . .	81
4.2.5	Interactions of Glu169 and Asp299: a Model for Early Photocycle Proton Transfer . . . . .	82
<b>5</b>	<b>The <math>P_0 \rightarrow P_2</math> phototransition: a Model for Proton Transfer into the Con- duction State of <i>CaChR1</i>.</b>	<b>86</b>
5.1	FTIR Difference Spectroscopy of the <i>CaChR1</i> $P_0 \rightarrow P_2^{380}$ phototransition . .	86
5.1.1	Band Assignments in the Carboxylic Acid C=O Stretch Region . . .	90
5.2	Conclusions from 270 K FTIR Difference Spectroscopy and a Model for the <i>CaChR1</i> $P_0 \rightarrow P_1 \rightarrow P_2^{380}$ Phototransition . . . . .	97
5.2.1	A Proton Transfer Model . . . . .	100
	<b>Bibliography</b>	<b>106</b>
	<b>Curriculum Vitae</b>	<b>121</b>

## List of Figures

1.1	Bacteriorhodopsin Photocycle . . . . .	2
1.2	Bacteriorhodopsin Structure . . . . .	3
1.3	BR Unphotolyzed versus K photoproduct . . . . .	6
1.4	<i>CaChR1</i> Sequence in a Transmembrane Model . . . . .	8
1.5	Schematic Description of Raman Spectroscopy . . . . .	17
1.6	Schematic Description of Raman, Pre-Resonance Raman, and Resonance Raman Spectroscopy . . . . .	18
2.1	Schematic of Flashlamp Output and Camera Acquisition . . . . .	24
2.2	Schematic Drawing of the Optistat DN2 Cryostat System used for Low Temperature FTIR Difference Spectroscopy . . . . .	27
2.3	Schematic Drawing LITAS System . . . . .	31
2.4	Schematic of Flashlamp Output and Camera Acquisition . . . . .	33
2.5	UV-Vis LITAS Data acquired on a Liquid Suspension of BR . . . . .	34
3.1	RRS Measurements of <i>CaChR1</i> , <i>CrChR2</i> , <i>NpSRII</i> , and BR. . . . .	36
3.2	Visible Absorption and Curve Fitting of Light and Dark-Adapted <i>CaChR1</i> . . . . .	38
3.3	<i>CaChR1</i> Raman Spectra with Different Excitation Intensities and Illumination Conditions. . . . .	39
3.4	Inverse Linear Correlation Between Ethylenic Frequency and Visible Absorption in Microbial Rhodopsins . . . . .	41
3.5	Curve Fit of <i>CaChR1</i> RRS Ethylenic Region . . . . .	42
3.6	Comparison of BR and <i>CaChR1</i> RRS data in H <sub>2</sub> O and D <sub>2</sub> O . . . . .	44
3.7	Peak Frequencies of the Two Ethylenic Components as Functions of pH. . . . .	45
3.8	RRS Spectra for pH Titration of <i>CaChR1</i> . . . . .	46
3.9	Effects of salt concentration and anion species on the RRS of <i>CaChR1</i> at pH3. . . . .	47
3.10	RRS of <i>CaChR1</i> WT and the E169Q and D299N Mutants . . . . .	48

4.1	80 K FTIR Difference Spectra of <i>CaChR1</i> , BR, and <i>CrChR2</i> . . . . .	58
4.2	Effects of Lipids on <i>CrChR2</i> Difference Spectra at 80 K . . . . .	60
4.3	<i>CaChR1</i> and <i>CrChR2</i> First Push Difference Spectra . . . . .	61
4.4	<i>CaChR1</i> and <i>CaChR1</i> with Regenerated Retinals in the Amide I Region . .	62
4.5	BR and BR with Regenerated Retinals over the Region from 800 – 1800 $\text{cm}^{-1}$ . 63	
4.6	<i>CaChR1</i> and <i>CaChR1</i> with Regenerated Retinals in the Ethylenic Region .	65
4.7	<i>CaChR1</i> and <i>CaChR1</i> with Regenerated Retinals in the Amide II' Region .	66
4.8	<i>CaChR1</i> and <i>CaChR1</i> with Regenerated Retinals in the C=O Stretch Region	67
4.9	Ca and <i>CrChR2</i> over the C=O Stretch Region . . . . .	69
4.10	<i>CaChR1</i> and <i>CrChR2</i> in $\text{H}_2\text{O}$ and $\text{H}_2^{18}\text{O}$ Over the Weak O–H Stretch Region. 70	
4.11	<i>CaChR1</i> and <i>CaChR1</i> with Regenerated Retinals in the Weak O–H Stretch Region . . . . .	71
4.12	<i>CaChR1</i> and <i>CaChR1</i> with Regenerated Retinals in the Weak O–D Stretch Region . . . . .	72
4.13	<i>CaChR1</i> and Mutants over the 800–1800 $\text{cm}^{-1}$ Region. . . . .	74
4.14	<i>CaChR1</i> and Mutants over the Ethylenic Region . . . . .	75
4.15	O–H stretch region for <i>CaChR1</i> and Mutants in $\text{H}_2\text{O}$ and $\text{D}_2\text{O}$ . . . . .	77
4.16	Schematic Model of the Binding Pocket Region in the Initial Phototransition. 83	
5.1	Static and Time Resolved Difference Spectra for <i>CaChR1</i> . . . . .	87
5.2	SVD Basis Spectra from Time Resolved FTIR with 270K Static Difference Spectra . . . . .	88
5.3	<i>CaChR1</i> Photoreversal Spectra . . . . .	89
5.4	<i>CaChR1</i> LITAS Measurement . . . . .	90
5.5	<i>CaChR1</i> Difference Spectra at 270K in $\text{H}_2\text{O}$ and $\text{D}_2\text{O}$ over the C=O region	91
5.6	270K Difference Spectra of <i>CaChR1</i> and Mutants . . . . .	92
5.7	Ground State Schematic Comparison of BR and <i>CaChR1</i> . . . . .	93
5.8	<i>CaChR1</i> and E169Q Comparison over the C=O Region . . . . .	95



5.9	<i>CaChR1</i> and D299E Comparison over the C=O Region . . . . .	96
5.10	<i>CaChR1</i> and D299N Comparison over the C=O Region . . . . .	98
5.11	<i>CaChR1</i> and F139K Comparison over the C=O Region . . . . .	99
5.12	C1C2 Structure Surrounding the Binding Pocket . . . . .	100
5.13	Proposed Model for the <i>CaChR1</i> $P_0 \rightarrow P_1 \rightarrow P_2$ Phototransition . . . . .	102

## List of Abbreviations

7TM	Seven Trans-Membrane Helices
Arg / R	Arginine
Asn / N	Asparagine
Asp / D	Aspartic Acid
BaF	Barium Fluoride
BR	Bacteriorhodopsin
<i>CaChR1</i>	channelrhodopsin-1 from <i>Chlamydomonas agustae</i>
CaF	Calcium Fluoride
ChRs	Channelrhodopsins
<i>CrChR2</i>	channelrhodopsin-2 from <i>Chlamydomonas reinhardtii</i>
DDG	Digital Delay Generator
DDM	n-Dodecyl $\beta$ -D-maltoside
DDS	double difference spectra

DM	Decyl- $\beta$ -D-maltoside
DMPC	1,2-dimyristoyl-sn-glycero-3-phosphocholine
ECPL	<i>E. Col</i> Polar Lipids
FSD	Fourier self deconvolution
FTIR	Fourier-transformed infrared
FWHM	Full Width at Half Maximum
Gln / Q	Glutamine
Glu / E	Glutamic Acid
LITAS	Laser Induced Transient Absorption Spectroscopy
Lys / K	Lysine
<i>Np</i> SRII	sensory rhodopsin-II from <i>Natronomonas pharaonis</i>
OG	$\beta$ -D-Octyl glucoside
Phe / F	Phenylalanine
(P)SB	(protonated) Schiff base

SVD	singular value decomposition
UV-Vis	Ultraviolet-Visible
WT	wild type
X <sub>nnn</sub> Y	Amino Acid X at position nnn mutated to Amino Acid Y

## Chapter 1

### Introduction

#### 1.1 The Type I Opsin Family

Opsins are a diverse family of proteins present throughout bacteria and archaea as well as within many kingdoms of eukarya. Although diverse, these proteins appear to have co-evolved to fulfill a large number of evolutionary functions and the family is identifiable by several key features namely the seven trans-membrane alpha helical backbone structure as well as the formation of a retinylidene Schiff base during post translational modification [1]. Within the family, opsins are grouped into two broad categories; type I and type II. Type I opsins are found primarily in prokarya although there are instances of type I opsins being present in algae, as in the main subject of this work, while type II opsins are found exclusively in animals. Each opsin type is also subcategorized into multiple sub-families based upon function. Within type II opsins, these families include the visual pigments [2], Go / Gs opsins [1], and Neuropsins [1] to name only a few. The entirety of this thesis will focus upon Type I rhodopsins derived from microbial sources including archaea, and algae which have played especial interest in the nascent field of optogenetics.

#### 1.2 Light Driven Proton Pumps: Bacteriorhodopsin from *Halobacterium Salinarium* as the Standard Model for Type I Opsins

Since its discovery in the 1970s [3,4] Bacteriorhodopsin (BR) has been a model protein used by biophysicists, crystallographers, biochemists, and many more disciplines to help investigate questions of primary importance in their fields. Such questions include examination of protein structure [5, 6], folding [7], membrane protein grouping and incorporation [8], active ion transportation [9], membrane electrical gradients [10], as well as many more. Of primary interest to many biophysicists including the Rothschild Laboratory at Boston University is the molecular mechanism governing photoactivation and the photocycle of BR. Human rhodopsin has been of extreme interest since its discovery in the late 19th century

both for its roll in light sensing (vision) as well as an example *par excellence* of a GPCR. Unfortunately, human rhodopsin is difficult to study both *in vivo* and *in vitro* due to its inability to readily clone into alternate expression systems as well as its “single shot” deactivation pathway [2]. BR, however, is readily expressed in large quantities and thus is not only of interest for understanding of membrane proton pumps but also as a surrogate to understand GPCR function.

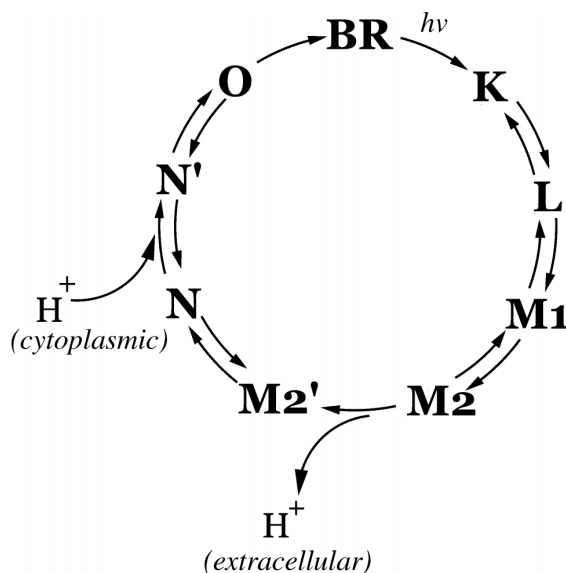


Figure 1.1: Bacteriorhodopsin photocycle adapted from [11] showing the photoinitiation event ( $BR \rightarrow K$ ); the release of a proton to the extracellular medium ( $M_2 \rightarrow M_2'$ ); the uptake of a proton to Asp96 from the cytoplasm ( $N \rightarrow N'$ ); and the completed resetting of the mechanism ( $O \rightarrow BR$ ). Many additional molecular events are well understood and are described in this section.

### 1.2.1 The Bacteriorhodopsin Photocycle

As briefly mentioned above, upon photoactivation, BR undergoes a series of structural changes, internal protonation and deprotonation events, and changes in hydrogen bonding. In addition, the retinal molecule undergoes several isomeric changes. The cumulative effect of all of the changes are to eject a proton to the extracellular medium, re-load a proton into the protein, and reset the mechanism responsible for these events. This process is known as

the photocycle and is depicted in figure 1.1 a description of which is found in the following sections.

### The Unphotolyzed State of BR

The unphotolyzed structure of bR is composed of seven transmembrane  $\alpha$ -helices as shown in Figure 1.2 (PDB 1C3W [6]) and an all-*trans* retinal molecule attached to the G-helix at Lys216 by means of a protonated Schiff base. The retinal is very near the center of the barrel formed by the hepta-helical structure and is surrounded by mostly hydrophobic residues with the exception of several residues which form the proton transportation pathway.

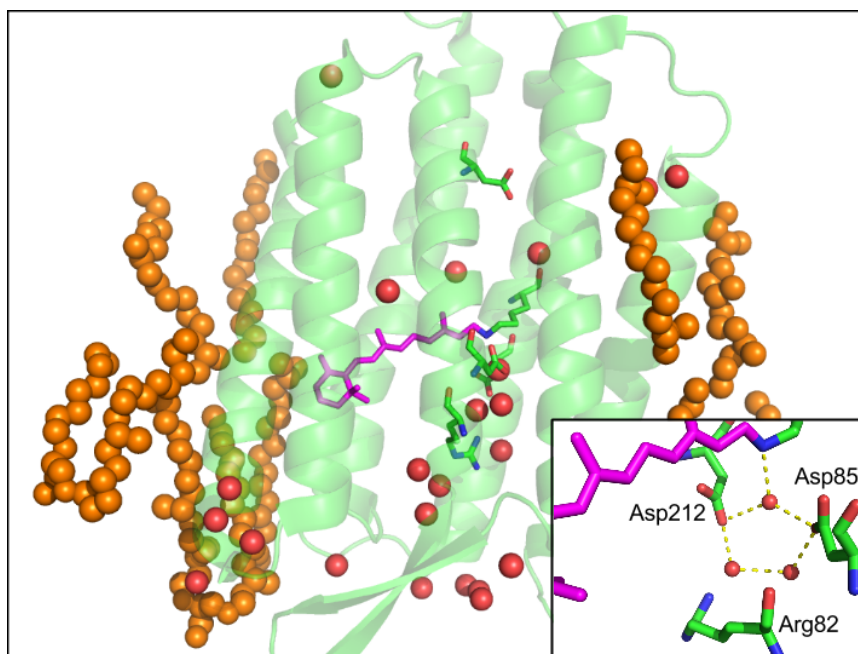


Figure 1.2: Bacteriorhodopsin unphotolyzed structure showing the seven, trans-membrane helicies as green ribbons; the lipid bilayer as orange spheres; the oxygen atoms from resolved water molecules as red spheres; the retinal molecule in pink with its protonated Schiff base linker to Lys 216; and several important residues discussed in the text including Asp85, Asp212, Arg82, and Asp96. Insert: the pentagonal water cluster formed by the PSB, Asp212, Asp85, and waters 401, 402, and 406. PDB 1C3W [6]

The Protonated Schiff Base (PSB) begins with an extracellular orientation toward two

aspartic acid residues (Asp85 and Asp212), an arginine residue (Arg82), and several water molecules which have been shown via protein crystallography experiments to form a pentagonal water cluster [11–13]. This pentagonal arrangement stabilizes the pKa of the PSB around 13.5 while the nearby proton acceptor group, Asp85 remains deprotonated with a pKa near 2.5 [14]. There are additional glutamic acid residues on the extracellular side (Glu194 and Glu204 not shown in Figure 1.2) which, in conjunction with Arg82, form the proton release complex (PRC) [13,14]. The cytoplasmic side of the active site is dominated by hydrophobic residues and, in the crystal structure, contains very few resolved water molecules [11–14]. This indicates that the hydrophobic region has developed to prevent “leakage” in this proton pump, thus improving the mechanism. One protonated residue on the cytoplasmic side, Asp96, serves to reprotonate the Schiff base later in the photocycle via a “water wire” [12].

In this configuration, BR has a visible absorption of  $\lambda_{\max} = 570$  nm which is of interest given that retinal dissolved in ethanol has a visible absorption of  $\lambda_{\max} = 380$  nm and a protonated Schiff base has an absorption of  $\lambda_{\max} = 470$  nm. The difference in absorbance is known as the “opsin shift” and is thought to be the result of the electrostatic interactions of the side-chains within bR, especially those residues located around the  $\beta$ -ionone ring [11,13], and the electronic structure of the PSB bound retinal.

Upon absorption of a photon, the all-*trans* retinal isomerizes into a 13-*cis* conformation which triggers a series of protein conformational changes resulting in the extracellular translocation of a proton as well as the resetting of the mechanism and, ultimately, a return to the unphotolyzed state. During this process, the proteins proceeds through several energy minimized conformationally meta-stable states which are identified by their transient UV-Visible absorption and are termed photointermediates. In order, bR proceeds from its unphotolyzed state, bR<sub>570</sub>, into J<sub>625</sub>, K<sub>590</sub>, L<sub>550</sub>, M1<sub>412</sub>, M2<sub>412</sub>, N<sub>560</sub>, and O<sub>640</sub>. [11,13] It is important to note that the M1 and M2 states, although identical in the UV-Vis, have been separated by their conformational state which is vital to the pumping mechanism, as described below.



## The Early Photocycle

The K intermediate is formed within several picoseconds of the photoabsorption event and is canonically referred to as the primary photo-reaction in BR as the initial photo-isomerization of the retinal chromophore is complete into a 13-*cis*, 15-*anti* configuration. In this configuration, the PSB remains in an extracellular orientation but the disruption of the dissociation of the electrons across the all-trans chain causes a red shift in the absorption spectrum out to  $\lambda_{\max} = 590$  nm. [11,13] In addition, as seen in figure 1.3, this rotation causes the PSB to pull away from the W402 and the pentagonal complex as well as the Asp 85 counterion [11,13]. Although the K intermediate rises in picoseconds and decays in microsecond, it is possible to isolate this photointermediate at cryogenic temperatures (80K) using CW illumination as described in the Materials and Methods section. This result allows for the study of the vibrational modes of the K intermediate using FTIR spectroscopy as well as the changes in these vibrational modes compared to the unphotolyzed state using FTIR Difference spectroscopy. In addition, it is possible to do near-IR, near-Resonance Raman spectroscopy under similar conditions although such experiments are not part of this work.

The L intermediate is formed upon decay of the K intermediate in several microseconds and is blue shifted from both the unphotolyzed absorption and the K intermediate absorption to about  $\lambda_{\max} = 550$  nm. Like the K intermediate, L can be isolated at low temperatures; approximately 135K. Conformationally, the L intermediate shows a PSB which is shifted back toward the Asp85 and W402 which prepares the PSB for deprotonation. In addition, crystallographic measurements show a shift in Arg82 along with several other residues that have been implicated in disrupting the pentagonal water cluster. [15] This disruption destabilizes the active site, changing the charge balance and increasing the pKa of Asp85.

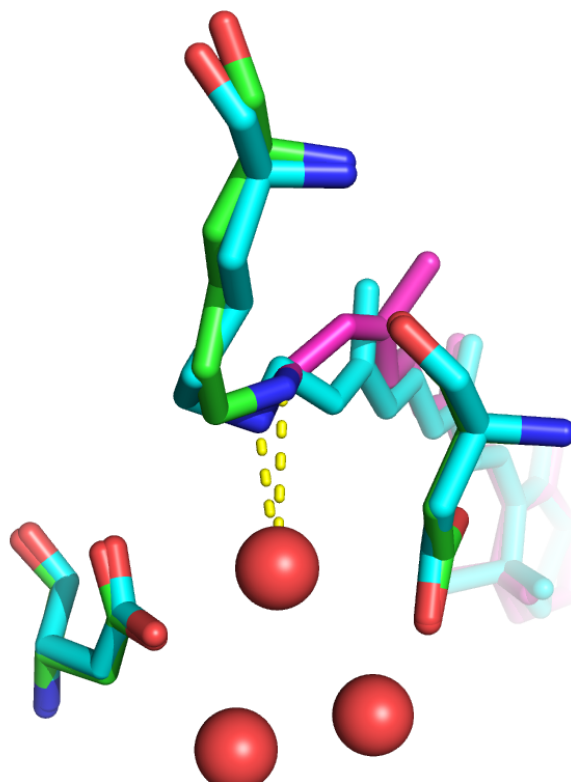


Figure 1.3: Bacteriorhodopsin unphotolyzed structure (sidechains in green, retinal in pink) and K intermediate structure (sidechains and retinal in teal) showing the PSB and active site with water molecules. Structure 1C3W [6] and 1IXF [15].

### The Late Photocycle

The M1 intermediate is formed after approximately  $40 \mu\text{s}$  post photoisomerization and is identified by the Schiff base deprotonating to Asp85. This is accompanied by a large blue shift of the visible absorption to  $\lambda_{\text{max}} = 412 \text{ nm}$  due to the change in electron density around the SB from the removal of the proton. In addition to the Schiff base deprotonation, a proton is ejected to the extracellular medium via disruption of the PRC (residues Glu194 and Glu204 at the extracellular interstitial surface) caused by the shifting of Arg82 [11, 13]. Finally, in the transition from the early M to late M intermediate ( $\text{M1} \rightarrow \text{M2}$ ), which does not involve any change in the visible absorbance, the conformational twist of 15-*anti* to 15-*syn* occurs reorienting the SB toward the cytoplasmic side and allowing access to the

hydrophobic channel leading to Asp96. [11, 13].

The N intermediate is formed after several hundred microseconds and is characterized by a red-shifted absorbance ( $\lambda_{\max} = 560$  nm) compared to the M intermediates. During the transition from M2 to N, a proton is transferred from the proton donor, Asp96 and as N decays into O, the donor is reprotonated by means of a pathway from several Asp residues on the cytoplasmic interstitial region.

The O intermediate is again red shifted ( $\lambda_{\max} = 640$  nm) as the retinal reisomerizes back to its unphotolyzed all-*trans* configuration. The final step in the resetting of the pumping mechanism is performed upon O decay as the proton acceptor group, Asp85 deprotonates to the PRC and the visible absorption is reestablished at  $\lambda_{\max} = 570$  nm.

### 1.2.2 Sensory Rhodopsin II from *Natronobacterium pharaonis*

SRII from *Natronobacterium pharaonis* (*Np*SRII) has a visible absorption maximum of  $\lambda_{\max} = 497$  nm, blue shifted from BR. Similarly to BR, *Np*SRII has an all-*trans* retinal chromophore connected via a Schiff base to a G-Helix lysine residue [16] The blue shifted  $\lambda_{\max}$  is thought to be a consequence of three residues which are non-homologous to BR (Val108, Gly130, Thr204) which are believed to alter the charge structure of the binding pocket which is known to play a large role in color tuning [17, 18]. One other important difference between BR and SRII is Arg72 (Arg82 in BR) which is extracellularly oriented. [17]

Three simultaneous mutation of BR (A215T/P200T/V210Y) [19] have been shown to allow BR to align with the *Natronobacterium pharaonis* transducer complex II (HtrII) and alter the functionality of BR such that it can effectively transmit a downstream signal. In addition, this BR triple mutant slows the photocycle to approximately 150 ms from the wild type time of 5 ms [19].

Upon absorption of a photon, *Np*SRII undergoes a photocycle similar to that of BR from the unphotolyzed state to  $K_{540}$ ,  $L_{540}$ ,  $M_{390}$ , and  $O_{560}$  [20]. Asp75 is the SB counterion and proton acceptor group in the transition to the M intermediate although any proton

pumping mechanism is slowed due to a lack of charged residues in the extracellular pathway [20,21]. Finally, proton uptake and release both occur on the extracellular surface of *NpSRII* providing no net charge translocation [22].

### 1.3 Channelrhodopsins

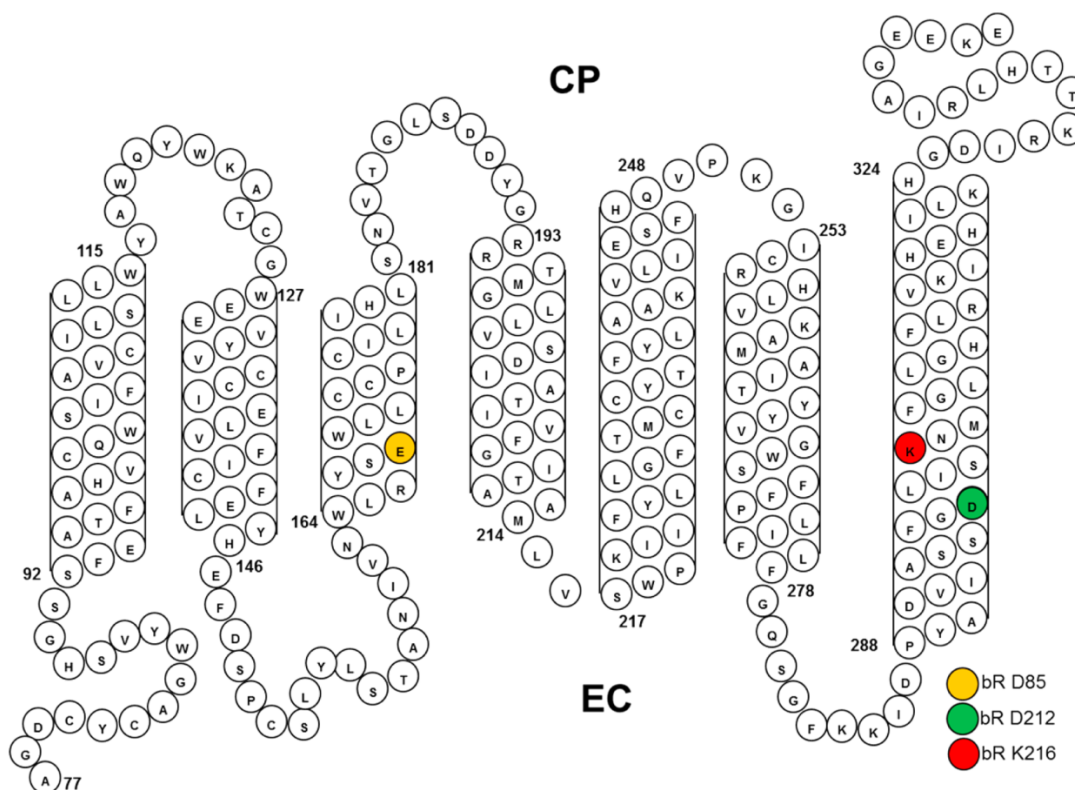


Figure 1.4: Sequence of CaChR1 and predicted folding pattern in the membrane based on earlier models of archaerhodopsins and other microbial rhodopsins (see, for example, [23]). Highlighted residues are the homologues of Asp85 and Asp212 in BR that comprise the complex counterion to the SB.

Channelrhodopsins (ChRs) are found in algae and, like all other microbialrhodopsins, have seven trans-membrane,  $\alpha$  helices with a bound retinylidene chromophore bound to the G-helix via a Schiff base formed with a lysine residue [24]. These proteins are light-activated, like all Type-1 rhodopsins, but unlike BR, form a gradient dependent ion channel

upon photoactivation instead of producing proton translocation [25]. This channel provides the algae with fast sensors to visible light which is used for phototaxis. Since their discovery, Channelrhodopsin 2 from *chlamydomonas reinhardtii* (*CrChR2*) has been used by the optogenetic community to trigger neuronal potentials with pulses of blue illumination. Recently, mutations of the wild-type *CrChR2* have been effective at improving the optogenetic properties including conductance, selectivity, kinetics, desensitization, light sensitivity, and spectral response. [25] Such mutants include *CrChR2* H134R,E123T, and C128X/D156A. In addition, several channels from other organisms have been used to great effect including *Volvox carteri* channelrhodopsin-1 and -2, and *chlamydomonas augustae* channelrhodopsin-1. [24,25]. It is this last channel that is the subject of this work.

## 1.4 Theory of Vibrational Spectroscopy

This section describes the general principles of linear absorption spectroscopy beginning with a derivation of the absorption scattering cross section and the Beer-Lambert Law. The second part of the derivations will include a classical derivation for Raman scattering. Following the derivations, techniques involving FTIR spectroscopy, FTIR difference spectroscopy, and near-IR, near-resonance Raman spectroscopy will be discussed.

### 1.4.1 Absorption Cross Section

The purpose of this derivation is to find an expression for the first order electric dipole absorption cross section of a system that is interacting with an electromagnetic wave. To achieve this, I begin with the quantum mechanical interaction picture. In this picture, we define a set of evolving states,  $|\alpha\rangle$ , that, at  $t = 0$ , are identical to the Schrödinger picture eigenstates,  $|n\rangle$ , and evolve in time according to the coefficients  $C_n(t)$ .

$$|\alpha\rangle = \sum_n C_n(t) |n\rangle \quad (1.1)$$

In the interaction picture, the equivalent of the Schrödinger Equation is given by

$$i\hbar \frac{\partial}{\partial t} |\alpha\rangle = V_I |\alpha\rangle \quad (1.2)$$

where  $V_I$  is the time dependent potential in the interaction picture.

Applying  $\langle n|$ , inserting a complete set of states and applying ((1.1)) to (1.2) gives

$$\begin{aligned} i\hbar \frac{\partial}{\partial t} \langle n| \alpha\rangle &= \langle n| V_I |\alpha\rangle \\ i\hbar \frac{\partial}{\partial t} C_n(t) &= \sum_m \langle n| V_I |m\rangle \langle m| \alpha\rangle \\ i\hbar \frac{\partial C_n(t)}{\partial t} &= \sum_m C_m(t) \langle n| V_I |m\rangle \end{aligned} \quad (1.3)$$

At this point, it is important to note that we are interested in first order perturbation theory and therefore, we must be careful to retain terms of the correct order in the small parameter,  $\lambda$ . The term on the left hand side is the time derivative of the time dependent amplitudes and is of order  $\lambda$ . The matrix element on the right is also order  $\lambda$  and thus, the coefficients on the right hand side must be of order  $\lambda^0$ . Under this constraint, and choosing this problem to represent the transition of the system out of the ground state (choosing  $m = 1$ ),  $C_m(t)$  is equal to 1 and equation (1.3) becomes

$$i\hbar \frac{\partial C_n(t)}{\partial t} = \langle n| V_I |1\rangle \quad (1.4)$$

The right side of this equation is the matrix element, in terms of the Schrödinger picture eigenstates. Thus, the interaction picture must be transformed using the time evolution operator

$$\begin{aligned} \langle n| V_I |1\rangle &= \langle n| UVU^\dagger |1\rangle \\ &= \langle n| e^{-\frac{iH_0 t}{\hbar}} V e^{\frac{iH_0 t}{\hbar}} |1\rangle \\ &= \langle n| V |1\rangle e^{\frac{iE_n t}{\hbar}} e^{-\frac{iE_1 t}{\hbar}} \end{aligned}$$

Using  $\omega_n = \frac{E_n}{\hbar}$  and defining  $\omega_{n1} = \omega_n - \omega_1$ :

$$\langle n| V_I |1\rangle = \langle n| V |1\rangle e^{\frac{i\omega_{n1} t}{\hbar}} \quad (1.5)$$

Inserting equation (1.5) into equation (1.4) and integrating yields

$$C_n(t) = \frac{-i}{\hbar} \int_0^t \langle n | V | 1 \rangle e^{\frac{i\omega_{n1}t}{\hbar}} dt \quad (1.6)$$

It is now important to define the potential. For a molecule in the presence of an electric field we can define a hamiltonian,  $H$  as

$$H = \frac{\mathbf{p}^2}{2m} + q\phi(t) - \vec{\mu} \cdot \vec{E}(t) \quad (1.7)$$

Thus, for a neutral system with dipole moment  $\vec{\mu}$ , the time dependent potential can be defined by

$$V = -\vec{\mu} \cdot \vec{E}(t) \quad (1.8)$$

Taking the electric field to be a plane wave propagating in direction  $\hat{k}$  with polarization vector  $\hat{\varepsilon}$

$$V = -\vec{\mu} \cdot \hat{\varepsilon} \frac{E_0}{2} [e^{i(\omega t - \vec{k} \cdot \vec{x})} + e^{-i(\omega t - \vec{k} \cdot \vec{x})}] \quad (1.9)$$

Substituting equation (1.9) into equation (1.6) gives

$$C_n(t) = \frac{iE_0}{2\hbar} \int_0^t \langle n | \vec{\mu} \cdot \hat{\varepsilon} [e^{i(\omega t - \vec{k} \cdot \vec{x})} + e^{-i(\omega t - \vec{k} \cdot \vec{x})}] | 1 \rangle e^{\frac{i\omega_{n1}t}{\hbar}} dt \quad (1.10)$$

In order to evaluate the matrix element, we note that the eigenstates are time independent but are not eigenstates of the position operator. Thus we must make the approximation that the term  $\vec{k} \cdot \vec{x}$  is small and can be ignored. This approximation is justified by examining the length scale of the problem. It is required that  $1 \gg kx$  or  $1 \gg \frac{2\pi x}{\lambda}$  where  $x$  is the extent of the dipole (on order of the size of the atom or molecule being interrogated) and  $\lambda$  is the wavelength of the plane wave. In the specific example of FTIR spectroscopy, light of wavelength  $\sim \mu\text{m}$  is used while the molecular dipole moment is  $\sim 1 \text{ nm}$ . Applying this approximation allows for the time dependence to be removed from the matrix element

$$\begin{aligned}
C_n(t) &= \frac{iE_0}{2\hbar} \langle n | \vec{\mu} \cdot \hat{\varepsilon} | 1 \rangle \int_0^t [e^{i\omega t} + e^{-i\omega t}] e^{\frac{i\omega_{n1}t}{\hbar}} dt \\
C_n(t) &= \frac{iE_0}{2\hbar} \langle n | \vec{\mu} \cdot \hat{\varepsilon} | 1 \rangle \int_0^t [e^{i(\omega+\omega_{n1})t} + e^{-i(\omega-\omega_{n1})t}] dt
\end{aligned} \tag{1.11}$$

Taking the integral

$$C_n(t) = \frac{iE_0}{2\hbar} \langle n | \vec{\mu} \cdot \hat{\varepsilon} | 1 \rangle \left[ \frac{e^{i(\omega+\omega_{n1})t} - 1}{i(\omega + \omega_{n1})} + \frac{e^{-i(\omega-\omega_{n1})t} - 1}{i(\omega - \omega_{n1})} \right] \tag{1.12}$$

The choice that the initial state of the system will be the ground state dictates that  $\omega_{n1} > 0$  and thus, if the frequency of the plane wave is close to the frequency of the transition ( $\omega_{n1}$ ) then the second term in the brackets will dominate. Seeking the sine function and defining  $\Delta\omega = \omega_{n1} - \omega$  equation (1.12) can be re-written as

$$\begin{aligned}
C_n(t) &= \frac{iE_0}{2\hbar} \langle n | \vec{\mu} \cdot \hat{\varepsilon} | 1 \rangle \frac{e^{i\frac{\Delta\omega}{2}t} - e^{-i\frac{\Delta\omega}{2}t}}{i\Delta\omega} e^{i\frac{\Delta\omega}{2}t} \\
C_n(t) &= \frac{iE_0}{2\hbar} \langle n | \vec{\mu} \cdot \hat{\varepsilon} | 1 \rangle \frac{\sin \frac{\Delta\omega}{2}t}{\frac{\Delta\omega}{2}} e^{i\frac{\Delta\omega}{2}t}
\end{aligned} \tag{1.13}$$

The probability of the transition from the ground state to the  $n^{th}$  state can be computed as  $P_n = |C_n(t)|^2$  by squaring equation (1.13)

$$P_n(t) = |C_n(t)|^2 = \frac{E_0^2}{4\hbar^2} |\langle n | \vec{\mu} \cdot \hat{\varepsilon} | 1 \rangle|^2 \frac{\sin^2(\frac{\Delta\omega}{2}t)}{(\frac{\Delta\omega}{2})^2} \tag{1.14}$$

Using the definition

$$\lim_{\alpha \rightarrow \infty} \frac{1}{\pi} \frac{\sin^2(\alpha x)}{\alpha x^2} = \delta(x) \tag{1.15}$$

and taking the limit of  $t \rightarrow \infty$  of  $P_n(t)$  yields the total probability that the transitions will occur

$$\lim_{t \rightarrow \infty} P_n(t) = \frac{E_0^2 \pi}{4\hbar^2} |\langle n | \vec{\mu} \cdot \hat{\varepsilon} | 1 \rangle|^2 \delta(\Delta\omega) t \tag{1.16}$$

This equation shows that the rate of the transition from  $|1\rangle$  to  $|n\rangle$  at long time is constant, known as Fermi's Golden Rule, and can be defined as

$$w_{1 \rightarrow n} = \frac{dP_n(t)}{dt} = \frac{E_0^2 \pi}{4\hbar^2} |\langle n | \vec{\mu} \cdot \hat{\varepsilon} | 1 \rangle|^2 \delta(\Delta\omega) \tag{1.17}$$



The absorption cross section is defined as

$$\sigma_{abs} = \frac{\text{(Energy/unit time) absorbed by the atom } (i \rightarrow n)}{\text{Energy flux of the radiation field}} = \frac{\hbar\omega w_{1 \rightarrow n}}{\Phi}$$

The energy flux of the electric field present can be defined in terms of the speed of light and the energy density

$$\Phi = cU = \frac{c\varepsilon_0}{2} E_0^2 \quad (1.18)$$

Putting equation (1.18) and equation (1.17) together with the definition of  $\sigma_{abs}$  gives the absorption cross section of an electric dipole transition

$$\sigma_{abs} = \frac{\pi\omega}{2\hbar c\varepsilon_0} |\langle n | \vec{\mu} \cdot \hat{\varepsilon} | 1 \rangle|^2 \delta(\Delta\omega) \quad (1.19)$$

#### 1.4.2 The Beer-Lambert Law

In both the FTIR spectroscopy and UV-Vis spectroscopy performed for this work, the absorption of light by the protein films or solution are the experimental observable of interest. The Beer-Lambert law relates the amount of incident light absorbed by many point absorbers within a macroscopic sample to the cross section and number density of those absorbers.

The Amount of energy removed from an incident, homogeneous beam of light with intensity  $I(t, z)$  while passing through a sample of thickness  $dz$  is

$$\frac{dI}{dz} = \frac{N_1}{V} \hbar\omega B_{21} u(\omega) F(\omega) \quad (1.20)$$

where  $N_i$  is the number of point absorbers in the interrogated volume  $V$ ;  $\hbar\omega$  is the energy per transition;  $u(\omega)$  is the energy density of the beam;  $B_{21}$  is the Einstein coefficient for absorption; and  $F(\omega)$  describes the broadening effects upon a given transition. The intensity of the beam is related to the energy density by a factor of  $cn$  (the speed of light times the index of refraction of the material) thus giving us the linear first order differential equation

$$\frac{dI}{dz} = \frac{N\hbar\omega B_{21} F(\omega)}{Vcn} I \quad (1.21)$$

which has the solution known as the Beer-Lambert Law:

$$I(z) = I(0)e^{-Kz} \text{ with } K = \frac{N\hbar\omega B_{21}F(\omega)}{Vcn} \quad (1.22)$$

This version of the Beer-Lambert Law directly relates the macroscopic absorption with Einstein matrix elements, the effects of spectral broadening, and the transition energies as well as the number of absorbers present. A more commonly used form of the law is given as:

$$I(z) = I(0) \times 10^{-OD} = I(0) \times 10^{-\epsilon(\omega)Cz} \quad (1.23)$$

where  $\epsilon(\omega)$  is the molar extinction coefficient as a function of radiation frequency,  $C$  is the molar concentration of the sample, and  $z$  is the path length through the sample. Similarly, Equation 1.23 can again be written in another, more familiar way to physicists

$$I(z) = I(0)e^{\sigma(\omega)Nz} \quad (1.24)$$

where  $\sigma$  is the absorption cross section,  $N$  is the number density of absorbers, and  $z$  is again the pathlength. In this way, a correlation between molar extinction and cross section can be calculated:

$$e^{\sigma Nz} = 10^{\epsilon Cz} \quad (1.25)$$

$$\sigma N = \epsilon C \ln(10) \quad (1.26)$$

$$\sigma \frac{N_A}{1000} = \epsilon \ln(10) \quad (1.27)$$

where the factor of 1000 comes from the conversion between  $\text{cm}^3$  in number density and L in concentration.

$$\sigma = \epsilon \frac{1000 \ln(10)}{N_A} \text{ or } 3.8 \times 10^{-21} \epsilon \quad (1.28)$$

### 1.4.3 Raman Scattering

Spectroscopy by measuring Raman scattering is a mature field with many commercial systems readily available. Simply, Raman scattering can be described as the inelastic scattering of light off of molecular vibrations (as opposed to Rayleigh scattering; the elastic scattering). From a quantum view, incoming photons scatter off of phonons thus either gaining energy from the interaction (phonon annihilation) or losing energy to the phonon mode (phonon creation).

#### Classical Derivation of Raman Scattering

For the purpose of this work, a classical approach to Raman spectroscopy and resonance Raman spectroscopy is appropriate and provides the necessary intuition for application of the technique to photoactive proteins.

In the classical picture, two masses,  $m_1$  and  $m_2$ , are connected by a Hooke's law spring force giving rise to the following second order ODE for the movement of the classical masses.

$$\frac{m_1 m_2}{m_1 + m_2} \left( \frac{d^2 x_1}{dt^2} + \frac{d^2 x_2}{dt^2} \right) = -K(x_1 + x_2) \quad (1.29)$$

by replacing the reduced mass with  $\mu$  and defining  $q = (x_1 + x_2)$  the ODE becomes

$$\mu \frac{d^2 q}{dt^2} = -Kq \quad (1.30)$$

which has the solutions of

$$q = q_o \cos(2\pi\nu_m t) \quad (1.31)$$

where  $\nu_m$  is the molecular vibrational frequency given as  $\nu_m = \frac{1}{2\pi} \sqrt{\frac{K}{\mu}}$

If we consider that these two particles are charged we can examine the dipole moment induced in the molecule by incident electromagnetic radiation.

$$P = \alpha E_o \cos(2\pi\nu_o t) \quad (1.32)$$

where  $P$  is the dipole moment,  $\alpha$  is the polarizability, and  $\nu_o$  is the frequency of the incident radiation. Under the small amplitude approximation, the polarizability can be expanded as a linear function of displacement

$$\alpha = \alpha_o + q \left( \frac{\partial \alpha}{\partial t} \right)_{q=0} + \dots \quad (1.33)$$

By using the expansion from above with the position of the the dipole moment from Equation (1.32) can be rewritten to first order as

$$P = \alpha_o E_o \cos(\pi \nu_o t) + q_o E_o \left( \frac{\partial \alpha}{\partial t} \right)_{q=0} \cos(2\pi \nu_m t) \cos(2\pi \nu_o t) \quad (1.34)$$

From the dipole moment we see terms representing two interactions with light. The first term,  $\alpha_o E_o \cos(\pi \nu_o t)$  is the Rayleigh scattering term and represents elastic scattering. The second term can be expanded to the following:

$$q_o E_o \left( \frac{\partial \alpha}{\partial t} \right)_{q=0} [\cos(2\pi(\nu_o - \nu_m)t) + \cos(2\pi(\nu_o + \nu_m)t)] \quad (1.35)$$

Here it becomes clear that the polarization of the model system oscillates at two frequencies; that of the sum of the electromagnetic and molecular vibrational frequencies and that of the difference of the two. These shifts in frequency are known as the Anti-Stokes and Stokes shifts, respectively, and can be directly measured by comparing the energy of the outgoing photons to that of the incident.

With this classical view in hand, the quantum picture can now be discussed by noting that the model can be replaced by a quantum system with energy states separated by  $h\nu_m$ . In this way, an incident photon will scatter off in one of three ways. The first, as depicted in the first panel of Figure 1.5 is the case of Rayleigh scattering. The second and third cases (panels two and three in Figure 1.5) are Stokes and Anti-Stokes Raman, respectively, where the energy of scattered photon (shown in red and blue, respectively) has been altered due to the system transitioning between vibrational energy states (indicated as  $E_0$  and  $E_0 + h\nu_m$ ).

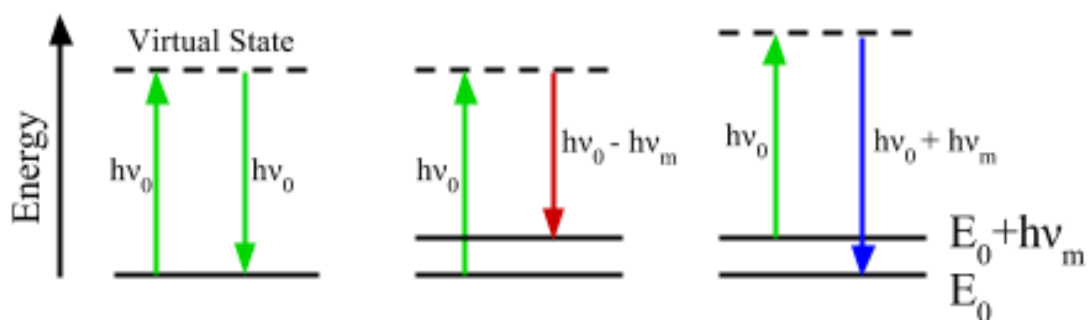


Figure 1.5: Three options for photon scattering off of vibrational energy levels,  $E_0$  and  $E_0 + h\nu_m$  through a virtual excited energy state, from left to right: Rayleigh scattering, no change in outgoing photon energy; Stokes scattering, a decrease in outgoing photon energy and an increase in vibrational state energy; Anti-Stokes scattering, an increase in outgoing photon energy and a decrease in vibrational state energy.

### Resonance Raman Spectroscopy

The description of Raman scattering above assumes that the incident radiation is far from any optical absorbance of the system as well as assuming a distinctive vibrational transition. While these assumptions are appropriate for a derivation of Raman scattering, for real molecular systems, and in particular for photoactive proteins such as the type used in the experiments described in this thesis, there are accessible electronic transitions as well as a manifold of vibrational states. The manifold of available vibrational states allows for many different transition pathways for return from the virtual excited state. In this way, identical incident photons will generate a spectrum of outgoing photons whose spacing in energy will be representative of the vibrational energy landscape of the sample and whose relative magnitude will represent the relative scattering cross sections for each transition. See the left hand panel in Figure 1.6.

If, however, the incident energy is tuned to the electronic transition within the system, the cross section for the Raman scattering is greatly enhanced leading to a massive increase in outgoing photons [26], shown on the right of Figure 1.6. This method is known as Resonance Raman spectroscopy and the excitation energy is in resonance with a naturally

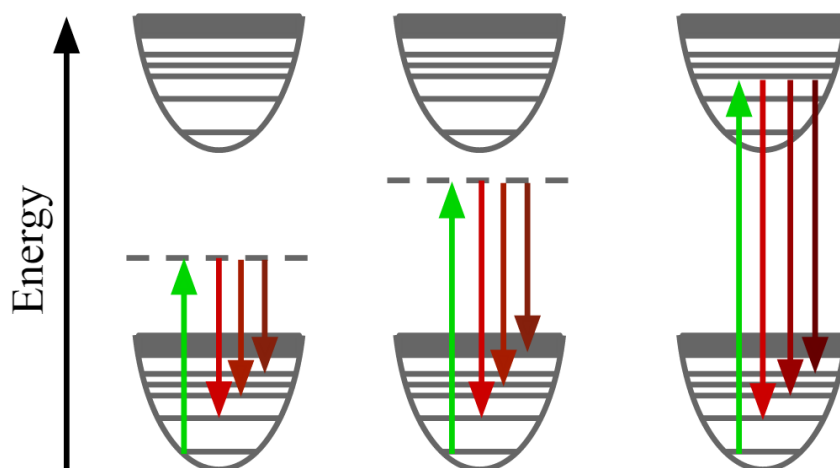


Figure 1.6: Schematic comparison of Raman spectroscopy: Standard Raman, pre-Resonance Raman, and Resonance Raman from Left to Right. The intensity of the Raman Scattering is greatly increased when the excitation energy is similar to an allowed electronic transition within the sample.

occurring electronic transition within the system of interest. Although highly favorable for increasing the yield of Raman photons, employing the resonance effect can highly complicate the measurement. In the case of the photoactive proteins involved in this work, the absorption of a photon changes the conformation of the chromophore element within the protein, the exact element that is being probed with Raman spectroscopy. This change in conformation alters the vibrational modes of the chromophore and thus, the Raman spectrum of the unphotolyzed protein and that of a photoactivated protein are not the same. De-convolving these two spectra in a sample which contains both unphotolyzed and photoactivated protein is extremely difficult, making it, therefore, preferable to not photoactivate the protein.

To still enjoy some of the enhancement provided by the above mentioned resonance effect, the excitation energy can be chosen to be slightly lower than the resonant transition energy (see Figure 1.6, middle panel). In this way, and specifically for the proteins discussed here, the photon energy will be insufficient to cause the conformational isomerization of the chromophore (or will do so at a very low rate) while the proximity of the virtual state to the photoactivated energy levels will still increase the Raman scattering cross

section. An additional benefit of this method is that only the energy levels associated with the resonance effect receive the enhancement of their cross section thus allowing, while in “pre-resonance” or “near-resonance”, for specific probing of the chromophore vibrational modes, an exceptionally useful tool for determining the isomeric conformation of the retinal molecules used in these photoactive proteins.

## Chapter 2

### Materials and Methods: Biophysical Spectroscopy

#### 2.1 Microbial-Rhodopsin Expression, Purification, and Reconstitution

Although present natively in *Chlamydomonas agustae*, *CaChR1* exists in very small quantities and would be extremely difficult to measure or purify from this native system. Unlike BR which is present as the Purple Membrane in *Halobacterium Salinarium*, *CaChR1* is spread in relatively small amounts only in the eyespot of the green algae. For this reason and given that there are or may be other photoactive proteins in the native system, it is required that *CaChR1* and all other proteins with the exception of BR used in this study be produced, purified, and reconstituted from a non-native system thereby allowing for the production of low containment, well controlled sample stocks.

In addition, the choice of a reconstitution system is highly influential on the final state of the protein. Although more difficult to work with, this work is nearly exclusively performed on proteins reconstituted in *E. Coli* Polar Lipids (ECPL) as opposed to using detergent solubilized proteins [27–29]. The biological conditions provided by ECPL reconstitution ensure that the *CaChR1* exists in as near to the native state as is possible for a reconstituted system. Later in this work, it will be shown that *CrChR2* in DMPC and ECPL are very similar but there are many studies which show that detergent solubilized proteins do not retain their native activity [30, 31].

##### 2.1.1 Channelrhodopsin Expression and Purification

The 7TM domain of *CaChR1* was expressed in *Pichia pastoris* and reconstituted using a procedure similar to that described by the Spudich Group [32]. Cells were grown in buffered minimal glycerol yeast (BMGY) medium; expression was induced by the addition of 0.5% methanol every 24 hours in the presence of the 5  $\mu\text{M}$  all-*trans* retinal. Cells were grown for 2 days, harvested by low-speed centrifugation, and disrupted by a bead beater. Membrane fragments were collected by centrifugation for 1 hour at 38000 rpm. The protein was par-



tially purified on a Ni-NTA agarose column (Qiagen, Hilden, Germany) after solubilization by incubation overnight in 3% dodecyl maltoside (DDM). For membrane reconstitution, the protein was eluted in 20 mM HEPES (pH 7.4), 100 mM NaCl, 0.05% DDM, and 300 mM imidazole and then mixed with *E. coli* polar lipids (ECPL; Avanti Polar Lipids, Alabaster, AL) at a concentration of 5mg/mL in 10% octyl glucoside at a mass ratio of 1:10 (*CaChR1*:ECPL) and incubated at room temperature for 1 hour after which 0.25 g of SM-2 Bio-Beads (Bio-Rad, Hercules, CA) was added, and the mixture was incubated at room temperature for 1 hour with slow rotation. The protein-lipid suspension was transferred to a fresh tube with 0.25 g of SM-2 Bio-Beads and the mixture was incubated overnight with slow rotation after which the reconstituted *CaChR1* proteoliposomes were pelleted at 10,000 rpm for 10 min. The pellet was resuspended in 10 mM phosphate buffer (pH 7.0) and washed twice.

Similar procedures were used to express the reconstituted *CrChR2* as described above except the cDNA of *CrChR2* encoded residues 1-309 with a C-terminal six-His tag sequence that was cloned in the pPIC9K vector (Invitrogen, Carlsbad, CA) within its EcoRI and NotI sites [33]. The production of the detergent purified *CrChR2* followed the methods of Bamann et al [33]. Structural guidance for the photocycle of *chr2* by an interhelical hydrogen bond [32]. For liposome reconstitution, *CrChR2* in 1% decyl maltoside (DM) was mixed with DMPC (Avanti Polar Lipids, Alabaster, AL) at a ratio of 1:20 (w/w).

Expression constructs containing the 7TM domains of the ChRs with a TEV protease site at the N-terminus and a nine-His tag at the C-terminus in the pPIC9IK vector backbone from Invitrogen, Carlsbad CA. Geneticin-resistant *P. Pastoris* clones were selected according to the manufacturer's instructions.

## 2.2 FTIR Spectroscopy and Difference Spectroscopy

Fourier-Transformed Infrared Spectroscopy (FTIR) is a method used to study the interaction of vibrational modes of molecules with electromagnetic radiation ranging in wavelength from 800 nm to 1 mm or in energy from 1.5 eV to 1 meV. For these studies, and infrared

radiation used is limited to a window within the mid-IR ranging from  $4000\text{ cm}^{-1}$  to  $800\text{ cm}^{-1}$ . This energy range directly interrogates the bending, stretching, and combination modes of the organic macromolecules used and includes the O–H, N–H, and C–H stretching regions; the C=O, C=C, and C=N stretching regions; and the C–C, C–O, and C–N bending regions [34, 35]. Unlike Ultra Violet-Visible radiation which interacts with electronic transitions with energies greater than  $1.5\text{ eV}$ , infrared radiation does not excite electrons.

As described previously, FTIR spectroscopy directly measures the infrared absorbance of a sample [34, 35]. The resulting spectrum is a combination of the bulk vibrational bands with cross sections accessible to IR radiation. By creating thin films of the proteins of interest, as described below in Sections 2.2.1 and 2.2.2, an absolute absorbance spectrum is measured using several different techniques; at room temperature, at low temperature, and with time resolution. Each of these techniques may be accompanied, in this case of photoactive proteins, with different illumination conditions the point of which is to drive these proteins out of their unphotolyzed state and into a variety of photointermediates. Once photolyzed, additional absolute absorbance spectra are measured which represent the bulk vibrational states the protein film in a that state. By properly combining the parameters discussed above and with repetition to improve signal to noise, a “difference spectrum” is formed by subtracting the absolute absorbances of the unphotolyzed from the photolyzed protein. From the Beer Lambert Law,

$$T = \frac{I}{I_0} = e^{-\epsilon lc} = e^{-\sigma lN} \quad (2.1)$$

where  $T$  is the transmitted intensity of the radiation at a given wavelength,  $I$  is the intensity of radiation measured by the detector with the sample in place,  $I_0$  is the measured background intensity,  $\epsilon$  is the molar extinction coefficient,  $l$  is the path length, and  $c$  is the concentration. These are the most commonly used quantities and correspond to quantities used most commonly in chemical studies. A change of units can reexpress equation (2.1) in terms of more common, physical quantities

$$T = e^{-\sigma l N} \quad (2.2)$$

where  $\sigma$  is the scattering cross-section,  $l$  is again the path length, and  $N$  is the number density of scatterers. A more useful quantity than transmittance is the absorbance,  $A$ , of a sample defined by

$$A = -\log(T) = -\log\left(\frac{I}{I_0}\right) \propto \sigma l N \quad (2.3)$$

The inherent improvement of this technique is that it is a direct, linear construction for the quantities of interest in the sample, namely  $\sigma$ ,  $l$ , or  $N$  and with careful sample preparation,  $l$  and  $N$  can be well controlled allowing for very exact measurements of the wavelength dependent cross section of a sample.

If, as described above, two spectra are recorded on the same sample, using the same background ( $I_0$ ) with one spectrum in the unphotolyzed state,  $A_1$ , and one post photoexcitation,  $A_2$ , the difference of these two spectra can be computed as

$$A_2 - A_1 = -\log\left(\frac{I_2}{I_0}\right) + \log\left(\frac{I_1}{I_0}\right) = -\log\left(\frac{I_2}{I_1}\right) \quad (2.4)$$

or similarly,

$$A_2 - A_1 \propto \sigma_2 l N - \sigma_1 l N = (\sigma_2 - \sigma_1) l N \quad (2.5)$$

This measurement, therefore, probes for changes in the cross section of the sample to be measured between the unphotolyzed and photolyzed states.

### 2.2.1 Time Resolved FTIR Difference Spectroscopy

The time resolved measurements were performed on a modified Bruker IFS66 v/s spectrometer from Bruker Optics Inc, Billerica, MA. Modifications to the instrument included the inclusion of a optically clear window on the front panel and the inclusion of a silver mirror inside of the sample chamber to allow for interrogation of samples with laser pulses. The

sample holder is produced by Herrick Scientific Products, Pleasantville, NY and holds two 25 mm diameter by 2 mm thick Calcium Fluoride windows from Crystran Ltd, Poole, UK. Additionally, the top of the sample chamber was altered to allow for coupling to a NesLab (Thermo Fisher Scientific, Waltham, MA) circulating chiller which is connected to the Herrick cell to provide temperature stability at the required experimental temperatures. For the Time Resolved experiments discussed here, the samples were run at 5 and 20 °C.

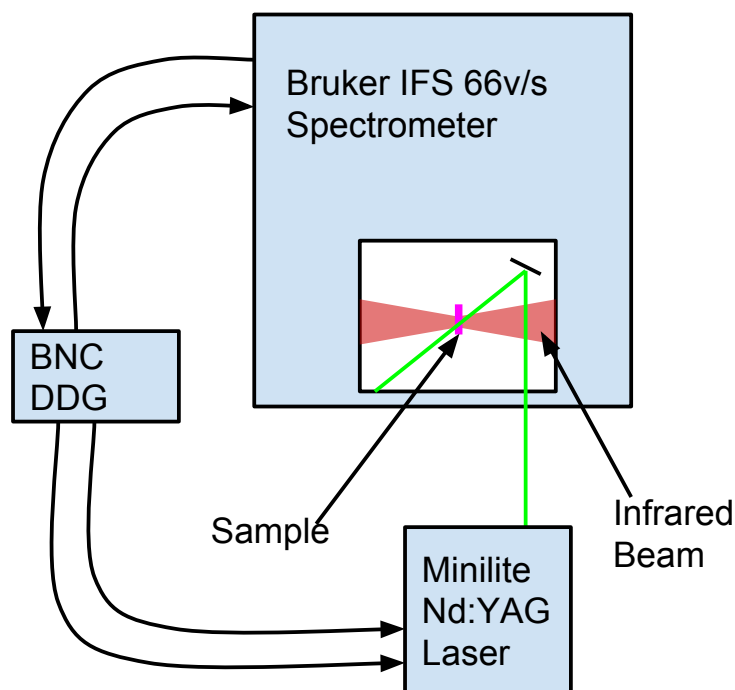


Figure 2.1: Schematic drawing of the Bruker IFS 66v/s FTIR Spectrometer and associated equipment which comprises the Time Resolved FTIR Difference Spectroscopy setup in the Rothschild Laboratory. Briefly, the Bruker programming begins a cycle by enabling the gate on the BNC DDG. The DDG then initiates a series of pulses, one to trigger the sequence of single beam acquisition of the infrared, and two to trigger the laser pulse which synchronously drives the protein photocycle.

A sample is made by depositing approximately 25  $\mu\text{L}$  of concentrated stock sample (approximately 50 to 100  $\mu\text{g}$ , described above in Section 2.1.1) onto one of the windows and allowing it to dry under argon or nitrogen. Once dry, a small drop (1 to 4  $\mu\text{L}$ ) of phosphate

buffered solution,  $^2\text{H}_2\text{O}$ , or  $\text{H}_2^{18}\text{O}$  (depending on the experiment of interest) is placed near the sample and a 2 mm thick, 25 mm diameter o-ring (McMaster-Carr, Elmhurst, IL) is sandwiched between the sample window and a clean, “top” window. The window – o-ring – window arrangement is sealed inside of the Herrick Cell which is tightened, and the sample is placed in the FTIR spectrometer, ready for testing and eventually, an experimental run.

Data is acquired on the Bruker instrument using a Macro program which serves to (1) time the initiation of a series of scans within the instrument and (2) wait for an incoming triggering pulse from a Berkely Nucleonics Corporation Digital Delay Generator (DDG – model 505). The DDG runs on a fixed cycle which provides three pulses the first of which triggers the Bruker signal acquisition. The second and third pulses are separated in time by 150  $\mu\text{s}$  and serve to trigger the Minilite 532 nm Nd:YAG laser from Continuum (San Jose, CA). By varying the timing between the first pulse and the second/third pulses, the laser flash can be tuned to arrive slightly after the FTIR scans have initiated thus providing “negative time-slices” compared with the photoexcitation.

Upon receipt of the initiation trigger from the DDG, the Bruker begins scanning and acquiring single-sided, forward-backward interferograms giving a total of 4 scans per complete mirror movement. The speed of the interferometer can be run up to 240 kHz (laser fringe read rate) which allows for a spectrum to be acquired in  $<8$  ms. A total of 80 scans will be acquired and if the delay for the laser is chosen properly, the photoexcitation should occur at scan 5 leaving one of each mirror movements pre-photoexcitation to be used to check the baseline. After acquisition, the macro program waits for a set time and then takes a series of 16 baseline scans which are binned and averaged; four for each mirror-travel direction. The reason for the delay is to ensure that the sample has decayed back to the unphotolyzed state. The macro then waits for a new DDG trigger pulse. This cycles is repeated in blocks of 500 shots with the output consisting of 84 averaged spectra; 4 baseline and 80 data.

The data is analyzed by saving out the averaged single beam spectra for each batch and difference spectra are computed via the Beer-Lambert Law with respect to the baseline spectra and a data spectra taking care to properly “align” the different mirror travel

directions. Thus in a simple schematic,

$$\begin{aligned}
 A_{1,5,9,\dots} &= -\log\left(\frac{D_{1,5,9,\dots}}{B_1}\right) \\
 A_{2,6,10,\dots} &= -\log\left(\frac{D_{2,6,10,\dots}}{B_2}\right) \\
 A_{3,7,11,\dots} &= -\log\left(\frac{D_{3,7,11,\dots}}{B_3}\right) \\
 A_{4,8,12,\dots} &= -\log\left(\frac{D_{4,8,12,\dots}}{B_4}\right)
 \end{aligned}$$

Due to the delay between initiation of the FTIR acquisition and the laser fire, as mentioned above, the first four acquisitions provide a baseline as well as the ability to determine if the system has fully relaxed into the unphotolyzed state. As well as examining the time series of difference spectra, slices can be averaged to produce “characteristic spectra”. For instance, in BR at 20 °C the fourth through tenth spectra, post laser excitation, can be averaged to isolate the BR→M difference spectrum.

### 2.2.2 Low Temperature FTIR Difference Spectroscopy

The low-temperature measurements are performed using the BioRad FTS 60A (Agilent Technologies, Santa Clara, CA) spectrometer coupled with a Optistat DN2 exchange gas Cryostat from Oxford Instruments, Abingdon, UK. The IR beam and HeNe tracer beam from the FTS 60A are aligned through two custom Calcium Fluoride (outer) and two Barium Fluoride (inner) windows. The sample sits in the center of the system. For illumination of the samples, custom software written into an Arduino microcontroller allows for the FTS 60A control computer to turn on and off the various channels of a DC4100 LED control box from Thorlabs Inc, Newton, NJ. Each channel powers a Thorlabs fiber-coupled LED (MxxxF1 series) which, in turn, are connected to a custom multimode bifurcated or tri-furcated fiber the output of which is focused into the sample chamber, reflected off of a steering mirror, and illuminates the sample.

Sample preparation for low-temperature FTIR Difference spectroscopy involves drying

a small amount of sample, typically around  $50 \mu\text{g}$  on a 17 mm in diameter by 1 mm thick Barium Fluoride window. Hydration is done through the vapor phase (much like for time-resolved samples) but only 0.3 to 1  $\mu\text{L}$  of hydration solution is necessary due to the much smaller volume of the sample compartment and the smaller film sample. A 1 mm thick, 17 mm diameter o-ring (McMaster-Carr, Elmhurst, IL) is placed on the sample window and is sandwiched with another clean window. The sample is then wrapped with Parafilm and Teflon tape to assist in retaining hydration at room and cryogenic temperatures and the assembly is mounted on the end of the cryostat sample rod using a retaining plate and 4 screws. The sample rod is lowered into and sealed within the cryostat. The sample compartment is evacuated then purged with helium exchange gas and the sample is then ready for preliminary testing and, eventually, an experimental run.

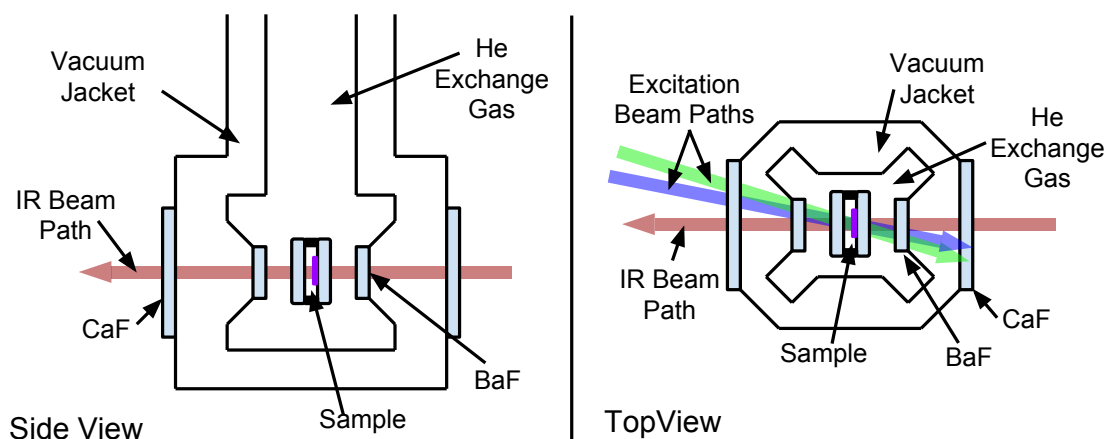


Figure 2.2: Schematic Drawing of the Optistat DN2 Cryostat system used for the low temperature FTIR measurements in this work. Left: a vertical cross section of the sample chamber providing a “on the side view”. Right: a horizontal cross section of the sample chamber providing a “top down view”.

The samples are cooled, quickly in the dark or with illumination to prevent dark adaptation (for BR, namely) and are below 237 K in less than 5 minutes. An ITC Model 5035 PID temperature control system provides feedback control between a heating element located inside the cryostat and wrapped around central heat exchange system and a temperature sensor mounted within the copper block, near the sample, on the sample insertion rod.

Liquid nitrogen is gravity fed through the bottom of the dewar section of the cryostat and into the capillary heat exchange. The boil-off is vented through a needle valve which acts to limit the flow of nitrogen gas and thus is a coarse control for sample cooling.

Once at temperature, the sample is left to equilibrate for >1 hour after which time the acquisition cycle begins. The acquisition begins with 20 spectra of 200 scans each being taken in the dark to be used later to check for sample stability in temperature and hydration. The cycle is as follows: one minute of acquisition in the dark, one minute of illuminated acquisition with light chosen to photolyze the sample, one minute of acquisition in the dark, one minute of illuminated acquisition to photoreverse the sample. This cycle takes approximately four and a half minutes including time for illumination changes and Fourier transform processing of the interferograms. For each sample, this cycle is repeated 30 or more times.

The data is analyzed by saving the absolute absorbance spectra of each scan (4 per cycle) and then averaging together complementary scans from different cycles. These averaged scans, representing one step in the cycle are then subtracted from one another to form difference spectra. Unlike the time resolved data, the use of the Beer-Lambert law is unnecessary since the data produced is an absorbance measurement. It should be noted, however, that the differences between absorbances done for these low temperature measurements produce the same result as the method employed with the single beam spectra in the time resolved measurements.

### **2.3 Near-Resonance Raman Spectroscopy**

The measurements presented here were taken with a Senterra Raman spectrometer from Bruker Optics, Billerica, MA, which uses a 785 nm narrow linewidth solid state laser source focused through an upright confocal microscope and onto the sample. The scattered radiation is recollected by the objective and passed through a narrow line-filter to remove the 785 nm laser radiation, reflected off of a diffraction grating, and collected by a CCD camera. Since the 785 nm laser radiation is of a well known energy, the difference between



the known energy and the energy of the radiation collected by the CCD can be computed and the output is presented as a plot of CCD counts as a function of Raman shift (typically in units of  $\text{cm}^{-1}$ ).

Sample preparation for acquisition using the Senterra spectrometer involves spinning down the protein of interest from its stock solution. Typically, 100 to 200  $\mu\text{L}$  of stock is concentrated at 15,000 rpm for 10 minutes. The supernatant is discarded and the pellet is drawn into a small volume syringe with a narrow diameter, flat tipped needle (Hamilton Laboratories, Reno, NV). The sample is deposited using the syringe into the closed end of a 500  $\mu\text{m}$  by 500  $\mu\text{m}$  square capillary which is again concentrated at 15,000 rpm for 10 minutes. Once concentrated, supernatant may be removed with a syringe and additional sample may be deposited if the pellet is not deemed adequate. After each additional aliquot of sample is added, additional concentration is required as stated above. The open end of the sample is sealed with critoseal (Krakeler Scientific, Albany, NY). The final sample is placed on the microscope stage of the Senterra confocal microscope where the focal plane is adjusted to be just under the 100  $\mu\text{m}$  quartz wall of the capillary. This maximizes the amount of sample interrogated by the 785 nm excitation laser while minimizing the number of Raman scattered photons re-absorbed by the sample.

Data acquisition is performed in scans of approximately 100 seconds with 100% laser power (approximately 40 mW at the sample). The objective is an Olympus 20X with an NA of 0.40. For each scan, a background is acquired automatically by the Opus 6.6 software (Bruker Optics). The resulting spectrum, if deemed appropriate by the operator on terms of SNR, background level, and absolute signal strength, is repeated anywhere from 10 to 200 times until a quality composite spectra can be obtained. Initial data manipulation consists of removing the linear baseline and contributions of the capillary from the spectrum using an iterative de-wiggling technique implemented in Matlab. Single acquisitions are then summed together to form one final spectrum which is used for analysis and comparisons.

An additional capability that has been added to the Senterra Raman microscope is the ability to illuminate a sample with one or more external, fiber-coupled sources. An Arduino

has been programmed to accept commands from the Senterra control computer the result of which are +5 or 0 V TTL outputs which, when coupled into T-Cube (LEDD1B) LED Drivers from Thorlabs (Newton, NJ) allows for toggling of fiber-coupled LEDs (MxxxF1 series) from Thorlabs. The out put of the LEDs is coupled into multimode fibers which are placed on the sample stage and oriented perpendicular to both the sample and the excitation beam path. In this way, a modified acquisition scheme can be applied wherein a number of spectra are acquired in the dark and a number are acquired with illumination. The number of each can be varied as well as the order of illumination; e.g. the sequence [dark - red - dark - blue] may be used and repeated over a large number of cycles.

## **2.4 UV-Vis Laser Induced Transient Absorption Spectroscopy**

Taking much from the sections deriving the Beer-Lambert Law and linear absorption spectroscopy, the BU MBL UV-Vis Laser Induced Transient Absorption Spectroscopy (LITAS) system was designed, built, and operated as part of the work to complete this thesis. This system provided many technical challenges as well as providing capabilities never before available to the Rothschild group. Below the hardware and software will be described along with data acquisition procedures, typical data and some specialty experiments.

The system, in essence uses a UV-Vis – Pump, UV-Vis – Probe scheme with the Minilite 532 nm Nd:YAG laser (Continuum) providing the pump and a Hammamatsu L9455-03 Xenon arc flashlamp providing the probe. The Minilite laser system provides a 3-5 ns pulse delivering up to 12 mJ per pulse to the sample. The Hamamatsu flashlamp provides a 500 ns FWHM pulse providing up to 8.5 mJ per pulse to the sample over a broad spectral range from 300 to 800 nm. Light from the flashlamp is fiber-coupled (discussed below) into the qPod 2e 1 cm cuvette holder which provides magnetic stirring, purge gas, and peltier cooling and heating between -30 and 110 °C. In addition the qpod (Quantum Northwest) provides two, perpendicular optical paths through the sample both of which can be coupled to custom fiber-coupled optics provided by Quantum Northwest. One set of optics acts as a collimator / collector pair while the other acts as a focusing / collecting pair. For all measurements

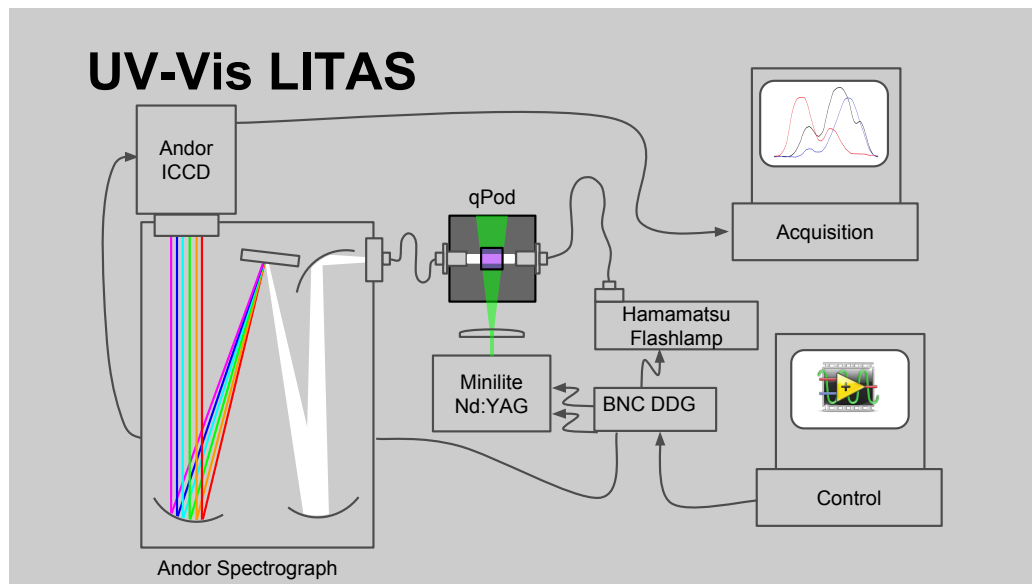


Figure 2.3: Schematic drawing of the LITAS system including the Nd:YAG pump, Flash-lamp probe, ICCD with associated spectrograph, qPod sample holder, acquisition computer, and control computer

where the white light is used, the collimator / collector fiber-coupled pair are used. Post-sample the probe light is fiber-coupled via a 7 fiber bundle-to-linear arrangement from Thorlabs into a Shamrock-163 spectrograph from Andor Technologies which is equipped with a 300 lines/mm grating blazed at 500 nm. An Andor iStar-3858 ICCD camera collects the spectrum and the data is acquired by the Andor Solis spectroscopy software. All timing is done for the system using a Berkeley Nucleonics 575 DDG with data written using custom LabView Software. The laser excitation pulse is coupled from freespace perpendicular to the white light illumination path.

Data acquisition with the LITAS system involves two, separate computer systems:

(1) the acquisition system which runs a custom macro written in the Andor Solis spectroscopy software which controls the iStar ICCD camera acquisition parameters including CCD vertical and horizontal binning, spectral averaging, gating duration, gain, and internal delay and records and saves the data as csv tables.

(2) the control system which, using custom LabView software, writes out pump / probe

timing data as well as acquisition timing data to the BNC 575 DDG, and triggers the acquisition of a shot by iStar ICCD camera.

One shot (the acquisition of one difference-spectrum) proceeds as follows: First, the control computer writes the set of timing commands to the BNC DDG which include pulse widths for the 4 outgoing signals (Xe-flashlamp trigger, camera acquisition trigger, laser-flashlamp trigger, laser q-switch trigger) as well as delay times between the laser flash and the Xe-flashlamp / acquisition ( $\tau_1$ ). The delay between the laser-flashlamp trigger and laser q-switch trigger is fixed at  $150 \mu\text{s}$  and both TTL signals must have a duration greater than  $15 \mu\text{s}$ . The delay between the Xe-flashlamp trigger and the camera acquisition trigger are fixed at  $80 \text{ ns}$  with each trigger also being at least  $15 \mu\text{s}$  in length. Labview then activates the Xe-flashlamp and camera acquisition channels while disabling the two laser trigger channels. The trigger is then sent which causes the DDG to send the white light and acquisition trigger signals a preset number of times ( $N$ ) with a system delay of  $T+\tau_1$  between triggers. This sequence provides the reference spectra for the particular timeslice  $\tau_1$ . Labview then writes to the DDG to activate the laser triggers and the pulse series is repeated, this time with the laser flash occurring after  $T$  and the white-light acquisition after  $T+\tau_1$ . This sequence provides the data spectra for the particular timeslice  $\tau_1$  and, along with the reference form a difference spectra according to the Beer-Lambert law illustrated above. The control computer then proceeds to the next timeslice dictated by the loaded control-list and repeats the background – data acquisition triggering.

Simultaneously with the above described cycle of triggers, the acquisition computer has important functionality. For each timeslice acquisition, the reference and data spectra are generated by acquiring an "image spectrum" comprised of imaging the output of the linear fiber onto the  $256 \times 1024$  pixel (h x w) detector. In general, this method would be too slow to be effective as full acquisition requires  $>5$  seconds but the pixels can be binned to reduce readout time. Generally, the full horizontal resolution is collected while the vertical pixels are used from 85 to 188 and binned by 2 or 4 pixels resulting in approximately 1 Hz or 0.5 Hz repetition rates, respectively. These pixel values are chosen because  $>75\%$  of the

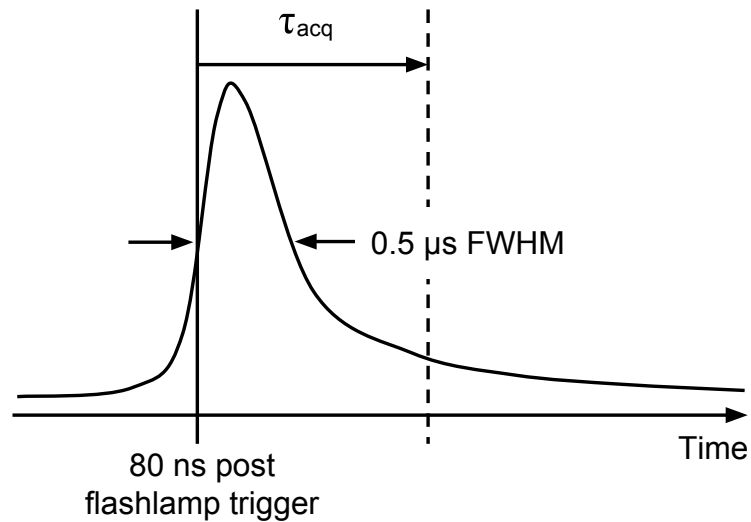


Figure 2.4: Schematic drawing of the LITAS system white light acquisition. Eighty nanoseconds post flashlamp trigger, the camera acquisition begins; at approximately half of the flashlamp max brightness. The camera acquires for a time,  $\tau_{acq}$  dictated by the acquisition computer and the time between sequential timeslices.

photons from the white light fall within this range. In addition, the acquisition computer sets the amount of time over which the intensifier is active and thus gating the acquisition “on”. This time,  $\tau_{acq}$  is calculated based on the timing between successive timeslices. For example, if timeslice  $n$  is at  $t_n = 1 \mu s$  and timeslice  $n+1$  is at  $t_{n+1} = 2 \mu s$ , the maximum allowed acquisition time would be  $0.75 \mu s [0.75 \times (t_{n+1} - t_n)]$  where the coefficient 0.75 was an arbitrary choice. The maximum value for  $\tau_{acq}$  is decided by the user and usually set to be just under the acquisition time at which any part of the image saturates the detector. In this way it is ensured that adjacent timeslices do not overlap while also ensuring that the acquisition window does not allow too much light to fall upon the detector.

Once a trigger timecourses have begun,  $N$  reference and  $N$  data acquisitions are co-added (matching the number of shots programmed into the control computer) and each set of co-added images are saved as one image. Post acquisition, the data are “compactified”; they are summed along the vertical direction producing a single spectrum from each image. These spectra are then time ordered into a  $T$  by 1024 matrix (timeslices by wavelength

pixels) and the differences are calculated by computing the absorption between each data scan (2n) and the reference scan immediately preceding it, (2n-1) in accordance with the following:

$$\Delta A = -\log_{10}\left(\frac{I_{2n}(\lambda)}{I_{2n-1}(\lambda)}\right) \quad (2.6)$$

Where  $\Delta A$  is the difference absorbance in units of  $\Delta OD$ , and  $I_{\tau_i}(\lambda)$  is the wavelength dependent intensity for timeslice  $\tau_i$ .

In this way, data showing the changes in absorption with time are produced. An example of such data, for Bacteriorhodopsin, is shown below.

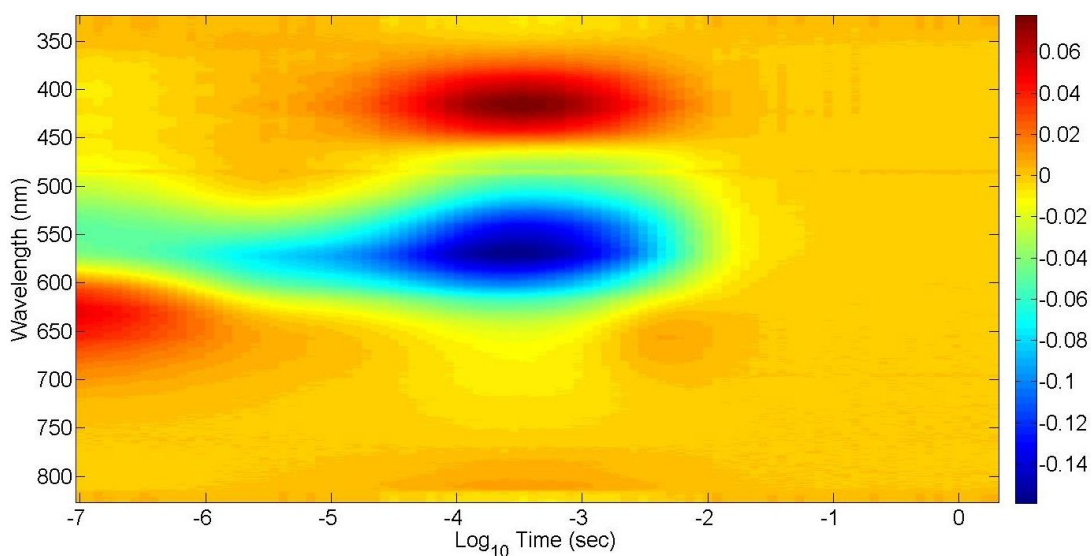


Figure 2.5: UV-Vis Acquisition with 100 timeslices logarithmically spaced from 100 ns to 1.9 seconds. The color scale shows difference bands representing depletion of the visible absorbance in the unphotolyzed state (blue), and build up of photointermediates (red) including the initial photoproduct, K, at 100 ns as well as the M photointermediate between 100  $\mu s$  and 1 ms.

## Chapter 3

### The P<sub>0</sub> state of *CaChR1*: Retial Conformation, Schiff Base Protonation, and the Counterion Complex

#### 3.1 Raman Spectroscopy of the *CaChR1* P<sub>0</sub> unphotolyzed state.

Samples of *CaChR1*, *CrChR2*, *NpSRII*, and BR were prepared in capillaries for RRS studies as described in the Materials and Methods chapter. In addition to WT samples, several mutant samples were studied including *CaChR1* E169Q and D299N. As discussed, this involved concentrating a small volume of stock solution, typically 10-30  $\mu\text{L}$ , removing the supernatant, and then inserting the pellet into a 0.5 mm square capillary which has one sealed end. The capillary is then centrifuged to concentrate the sample to the sealed end and the top is sealed with crytoseal.

Samples were also studied via pH titration which was performed by preparing individual samples at separate pH values. This was performed by diluting the initial aliquot of stock solution in 1 mL of 50 mM phosphate buffer at the pH of interest. The sample was then concentrated, the supernatant removed, and the pellet was resuspended in another 1 mL of phosphate buffer. This procedure was repeated at least 4 times for each desired pH and after the final supernatant was removed, the sample was loaded and sealed into a capillary, as described.

A similar procedure was used for the pH 3, 2 M NaCl and 1 M Na<sub>2</sub>SO<sub>4</sub> experiments except that there was no K<sub>2</sub>PO<sub>4</sub> present in any of the solutions used.

##### 3.1.1 Similarity of the Raman Spectra of *CaChR1*, BR, and *NpSRII*

The near-IR resonance Raman spectrum of *CaChR1* is remarkably similar to the near-IR resonance Raman spectrum recorded under identical conditions for BR and even more similar to that of *NpSRII* (See Figure 3.1). This is particularly true in the configurationally sensitive fingerprint region (1150–1300  $\text{cm}^{-1}$ ) that involves mainly the C–C stretching modes of the retinal chromophore. In the case of both BR and *NpSRII*, previous RRS and FTIR

studies [16,36–38] led to the conclusion that the retinal chromophore exists in an all-*trans* protonated SB configuration. For example, bands in the BR spectrum were previously assigned to an all-*trans* retinal chromophore using model retinal compounds and isotope labeling [39].  $^{13}\text{C}$  solid state NMR also provides strong confirmation of the existence of an almost pure all-*trans* configuration of the retinal chromophore in the case of BR [40]. In addition, *NpSR*II appears to exist in a pure all-*trans* form in both light-adapted and dark-adapted states [41].

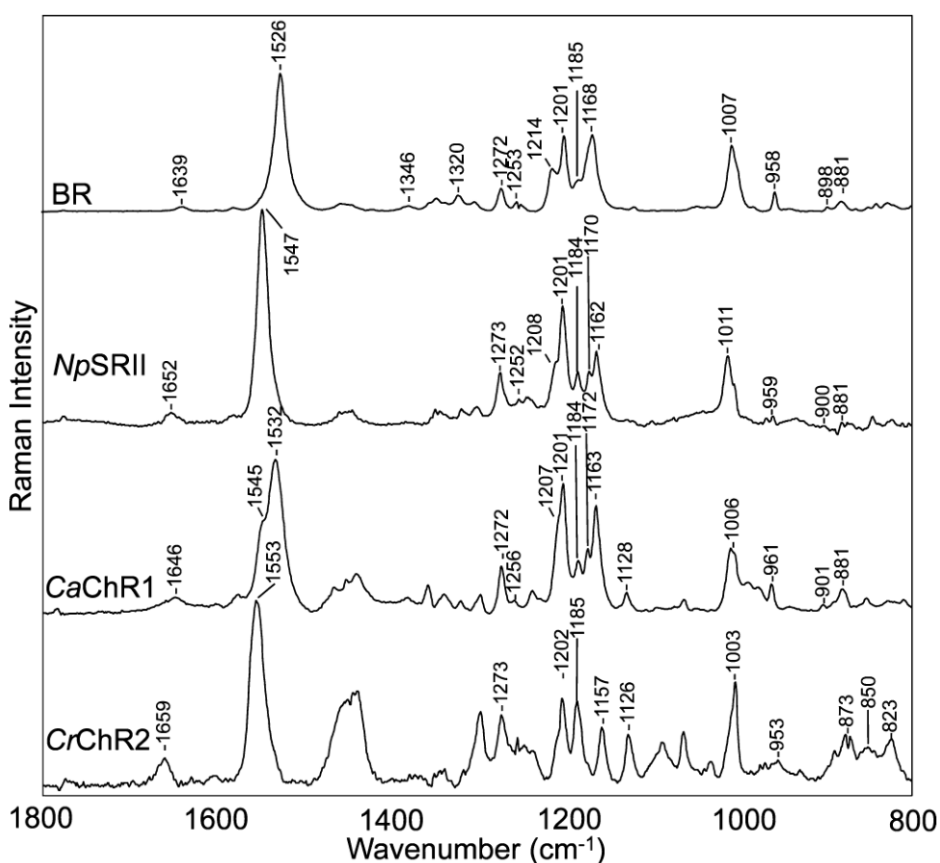


Figure 3.1: Resonance Raman spectra of BR (purple membrane), *NpSR*II and *CaChR*1 reconstituted into *E. coli* polar lipids, and *CrChR*2 reconstituted into DMPC recorded in 50 mM phosphate buffered solution at pH 7. Data were recorded at room temperature using a 785 nm probe laser with a 100 mW power (40 mW measured at the sample). A background spectrum of the quartz capillary and buffer was subtracted from the sample. The spectra were scaled using the intensity of the ethylenic band at  $1526\text{ cm}^{-1}$ .



Bands in the fingerprint region of the retinal are particularly sensitive to the isomeric state of retinal and arise mainly from the various mixed C–C stretching modes of the chromophore [38,39,42]. The similarity of the relative intensities and frequencies of bands in this region for *CaChR1*, BR, and *NpSRII* strongly indicates that all three chromophores have similar all-*trans* retinal configuration. For example, bands appear in this region in *CaChR1*, BR, and *NpSRII* near 1272, 1256, 1207 (shoulder), 1201, 1184, 1172, and 1163  $\text{cm}^{-1}$  (*CaChR1*). While the 1172  $\text{cm}^{-1}$  band in *CaChR1* and the 1170  $\text{cm}^{-1}$  band in *NpSRII* do not appear clearly in BR, which is most likely due to the upshift of the 1163  $\text{cm}^{-1}$  band to 1168  $\text{cm}^{-1}$ . The latter band in BR is assigned mainly to the C<sub>10</sub>–C<sub>11</sub> stretching mode [39] and may indicate some differences in structure in this region of the chromophore compared to the structures of the *CaChR1* and *NpSRII*. Many other microbial rhodopsins with all-*trans* chromophores such as AR3 [43] and green- and blue-absorbing proteorhodopsin (GPR and BRP, respectively) [44] also exhibit very similar resonance Raman spectra in the fingerprint region, reflecting a similar all-*trans* retinal configuration.

The agreement between the intensity and frequency of many bands outside the fingerprint region also provides strong evidence of the similar configurations of BR, *NpSRII*, and *CaChR1* chromophores. For example, the 1006  $\text{cm}^{-1}$  band assigned in BR to in-plane methyl rocking vibrations of the two methyl groups at positions C<sub>9</sub> and C<sub>13</sub> appears at a similar frequency in *CaChR1* [39]. A second example is in the hydrogen out-of-plane (HOOP) region, where bands appear at 961, 901, and 881  $\text{cm}^{-1}$  in *CaChR1* and 958, 889, and 881  $\text{cm}^{-1}$  in BR [44].

Visible absorption measurements indicate that there is very little change in the absorption of *CaChR1* between the light- and dark-adapted states (Figure 3.2). The curve-fit major component appears at 524 nm, close to the peak for the maximal wavelength of the action spectrum for the current generation of *CaChR1* [32]. Furthermore, the spectrum of BR recorded under identical conditions (Figure 3.1) using 785 nm Raman excitation exhibits no major bands characteristic of the dark-adapted state (e.g., the 1536  $\text{cm}^{-1}$  ethylenic band), [43] indicating that even if *CaChR1* did exhibit dark adaptation it should remain in

the light-adapted state during the Raman measurement. Reducing the 785 nm excitation power from 100 to 10 mW or continuously illuminating the sample with a 530 nm LED during the measurement did not significantly alter the resonance Raman spectrum (Figure 3.3). Thus, we do not consider it likely that the Raman spectrum recorded with 785 nm excitation shown in Figure 3.1 reflects a long-lived photoproduct in the photocycle.

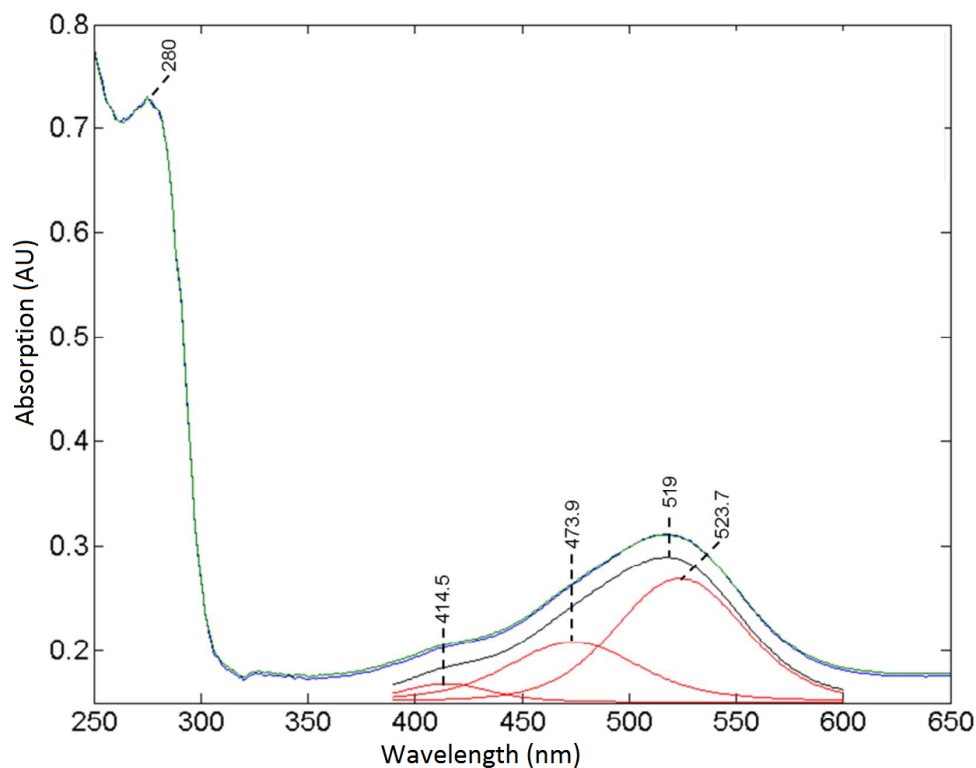


Figure 3.2: Visible Absorption of Light and Dark-adapted *CaChR1*. The light and dark-adapted spectra are very similar and shown as green and blue plots, respectively. The subcomponent bands for the light-adapted spectrum are also shown (red traces) and were computed using the peak fitting algorithm provided in Grams AI. The black trace is the sum of the three fitted bands.

In contrast to *CaChR1*, the RSS of *CrChR2*, particularly in the fingerprint region, differs significantly from that of BR and *CaChR1* (Figure 3.1). This reflects the heterogeneity of the chromophore structure of *CrChR2* that has been found to exist in a mixture of all-*trans* and 13-*cis* isomers both in the light- and dark-adapted states [28, 45, 46]. For example, Nack et

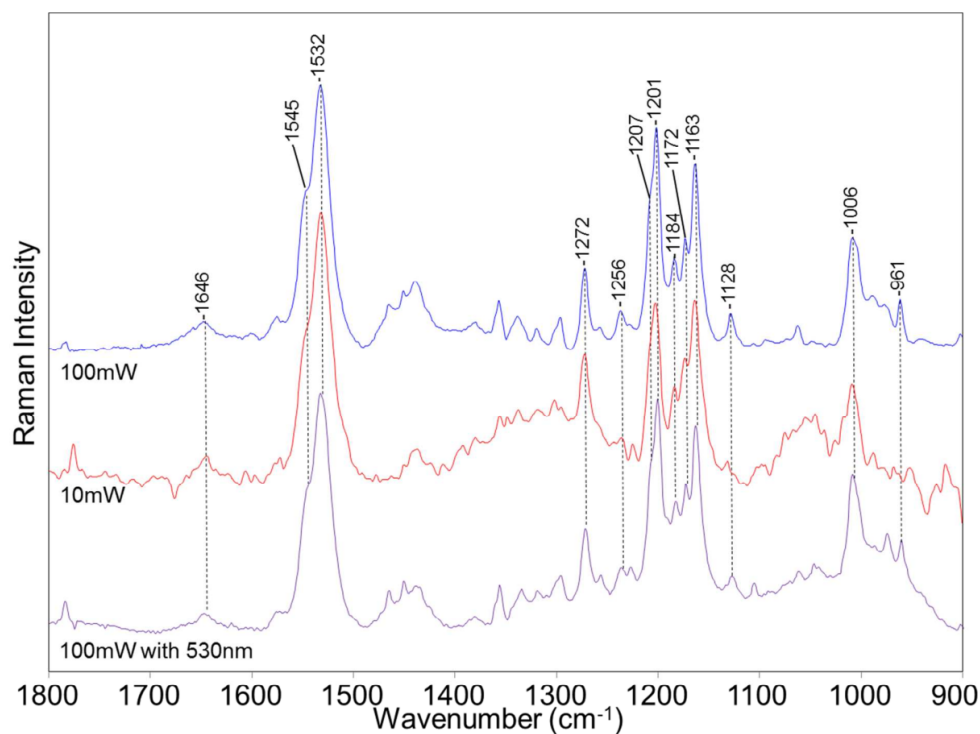


Figure 3.3: Comparison of *CaChR1* resonance Raman spectra recorded under different conditions. Top: RRS recorded at pH 7 with 100 mW 785-nm laser excitation power. Middle: pH 7, 10 mW. Bottom: same conditions as top except with 20 mW/cm<sup>2</sup> continuous illumination from a 530 nm LED.

al. [28] found on the basis of RRS and extraction–high-performance liquid chromatography analysis that there were significant contributions from 13-*cis* retinal and small amounts from 9-*cis* retinal, both of which increased with light adaptation. Note that even though the earlier study was performed using a different laser excitation frequency (647 nm) [28], almost all of the bands appear at similar frequencies and intensities as in the resonance Raman spectrum shown in Figure 3.1 recorded using 785 nm excitation.

The most outstanding differences between *CrChR2* and BR, *NpSR11*, and *CaChR1* appear in the fingerprint region. The magnitude of the 1185 cm<sup>-1</sup> band, which is highly characteristic of the 13-*cis* isomer, increases relative to that of the 1200 cm<sup>-1</sup> band, which is characteristic of the all-*trans* form [39]. This increase is also apparent in both the resonance Raman spectrum and FTIR difference spectrum of many of the BR photointermediates with

a 13-*cis* retinal configuration [47,48]. For example, bands at 1186 and 1198  $\text{cm}^{-1}$  are almost equal in magnitude in the resonance Raman spectra of the N intermediate, [49] very similar to bands reported here and previously for *CrChR2* [28]. An almost identical fingerprint profile is also found for BR 548, the 13-*cis* retinal-containing component of dark-adapted BR [39]. On the basis of normal mode calculations, the 1185  $\text{cm}^{-1}$  band is assigned primarily to the C<sub>10</sub>–C<sub>11</sub> stretching mode of the retinylidene chromophore [39]. In contrast, microbial rhodopsins that contain the predominantly all-*trans* -retinal chromophore, such as light-adapted BR and *NpSRII* (see Figure 3.1), display a much weaker band intensity near 1185  $\text{cm}^{-1}$  relative to that near 1200  $\text{cm}^{-1}$ , which is most likely due to a different C–C stretching mode [37].

Additional differences in the resonance Raman spectra of *CrChR2* compared to BR and *CaChR1* appear in the in-plane methyl rocking vibration and HOOP mode regions (Figure 3.1). Overall, this comparison indicates that *CrChR2* has a significantly higher fraction of the 13-*cis* isomer in the light-adapted ground state than *CaChR1* does.

### 3.1.2 Assignment of the *CaChR1* Ethylenic C=C Stretching Vibration

One significant difference between the resonance Raman spectra of BR, *NpSRII*, *CaChR1*, and *CrChR2* is in the ethylenic C=C stretching region where intense bands appear at different frequencies (BR at 1526  $\text{cm}^{-1}$ , *CaChR1* at 1532  $\text{cm}^{-1}$ , *NpSRII* at 1547  $\text{cm}^{-1}$ , and *CrChR2* at 1553  $\text{cm}^{-1}$ ) (Figure 3.1). Importantly, these variations are in agreement with the expected inverse relationship between  $\lambda_{\text{max}}$  and  $\nu_{\text{C=C}}$  found for most microbial rhodopsins. For example,  $\lambda_{\text{max}}$  and  $\nu_{\text{C=C}}$  of *CaChR1* fall close to a best fit line that includes several microbial rhodopsins, including the dark-adapted form and M intermediate of BR (see Figure 3.4).

In addition to the 1532  $\text{cm}^{-1}$  band, a shoulder appears near 1545  $\text{cm}^{-1}$  in the resonance Raman spectrum of *CaChR1*, which reflects an underlying band near 1549  $\text{cm}^{-1}$  as revealed by curve fitting (see Figure 3.5). It is possible that this band arises from a second form of *CaChR1* that on the basis of the empirical correlation shown in Figure 3.4 would have a

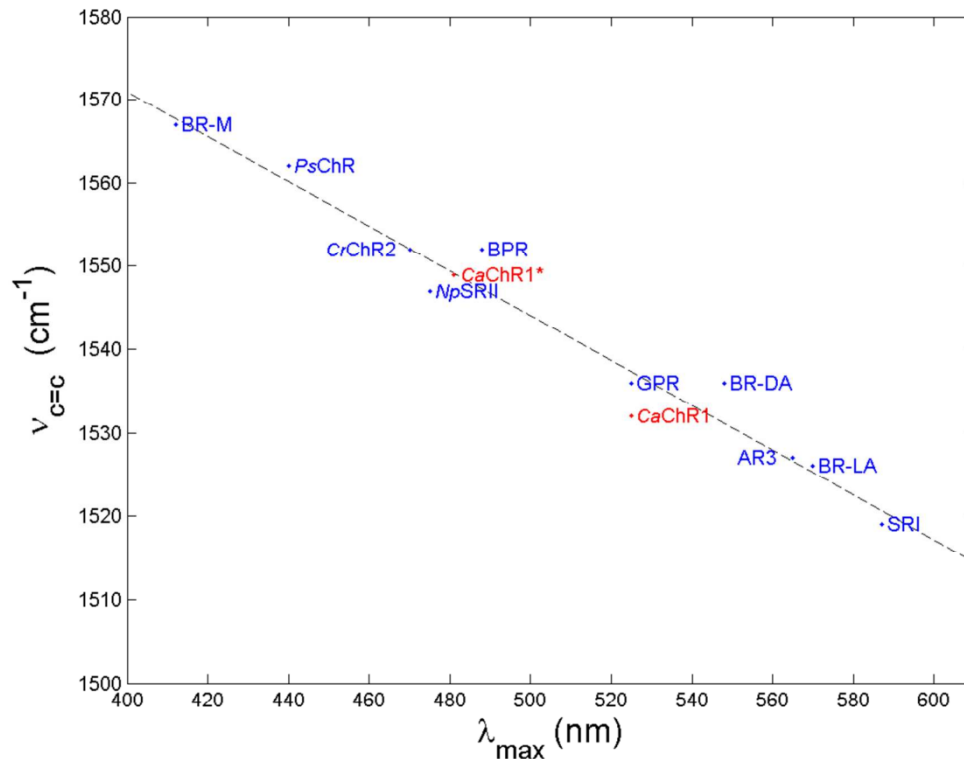


Figure 3.4: Inverse linear correlation between ethylenic frequency and visible absorption wavelength maximum of several microbial rhodopsins including *CaChR1*. All wavelength and frequency values are from this paper (*CaChR1*, *CrChR2*, *NpSRII*, light-adapted BR) or from previously published data: light-adapted AR3 [43]; BR dark-adapted [40]; BR M-intermediate [50,51]; BPR and GPR [44]; SRI [52].

$\lambda_{\max}$  near 480 nm. In fact, curve fitting of the visible absorption of light-adapted *CaChR1* (Figure 3.2) reveals a second component near this wavelength. However, this does not establish the existence of a second form of *CaChR1*, because multiple bands can appear in the visible absorption of retinal-containing proteins because of vibronic coupling. For example, in the case of *NpSRII*, a major band appears at approximately 500 nm and two others attributed to vibronic coupling appear at 460 and 420 nm [53,54]. The first vibronic band is separated from the major band by  $17.6 \text{ cm}^{-1}$ , which is not significantly different from the separation of the *CaChR1* main band and curve-fit shoulder ( $16.8 \text{ cm}^{-1}$ )

In the case of *CrChR2*, a second ethylenic band in the resonance Raman spectrum was

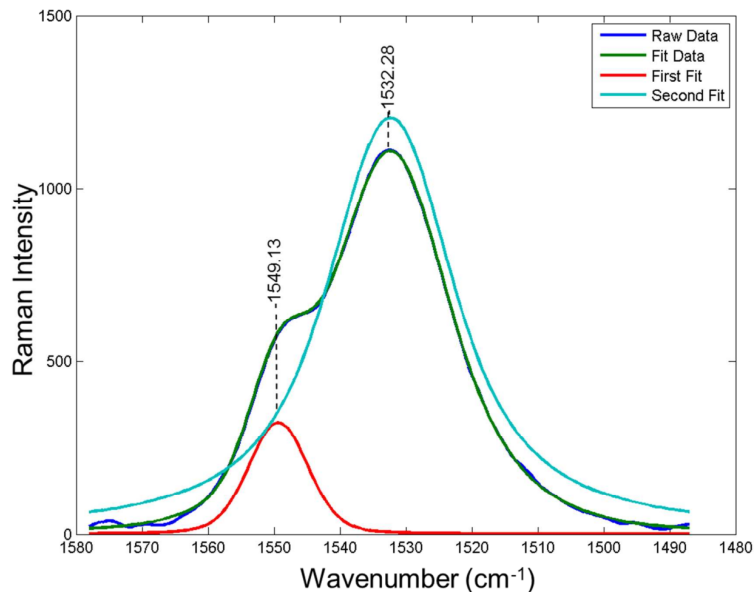


Figure 3.5: Curve fit of ethylenic region of the RRS of CaChR1 at pH 7. Fitted data is the shown in Figure 3.1. Curve fitting was performed using the Grams AI spectroscopy suite (Thermo-Fischer Scientific). Two Voigtian components (red and light blue) plus a baseline (not shown) resulted in a close fit (green curve) to the raw data (blue curve). A similar analysis was used for RRS at other pHs and also for the two mutants E169Q and D299N in order to determine the frequency, intensity and full-width at half-maximum of each of the component bands.

also found by curve fitting at  $1557\text{ cm}^{-1}$  and assigned to the presence of a second species having predominantly 13-*cis* retinal [28]. However, in the case of *CaChR1*, the two bands in the resonance Raman spectrum may arise from a single chromophore species that has two Raman- active ethylenic stretching modes as previously observed for the resonance Raman spectrum of the L intermediate of BR [55, 56]. The existence of multiple ethylenic modes is common for vibrational spectra of retinals and is actually expected for microbial rhodopsins, although in some cases only one mode dominates the resonance Raman spectrum. An additional possibility is that the second band at  $1549\text{ cm}^{-1}$  arises from non-resonant Raman contributions of the protein (non-chromophore) such as the amide II vibration mode characteristic of  $\alpha$ -helical protein structure. However, this mode is relatively

weak in the nonresonance Raman spectra of proteins such as bovine opsin relative to the amide I and III modes [57]. Because we do not observe contributions from the amide I mode except in the case in which CaChR1 is partially heat denatured where it appears at  $1652\text{ cm}^{-1}$  (data not shown), it is unlikely the amide II mode contributes significantly to this shoulder. Further studies using differential isotope labeling of the retinal chromophore and protein were performed and the results are discussed with respect to these various possibilities in the following chapter.

### 3.1.3 Assignment of the *CaChR1* SB C=N Stretching Mode and Strength of Hydrogen Bonding

In general, the C=N SB stretching frequency ( $\nu_{\text{C=N}}$ ) depends on the bond strength of the C=N bond as well as coupling to other normal modes of the retinal. The C=N bond strength is directly influenced by molecular interactions with the SB such as hydrogen bonding to water molecules and the presence of nearby counterions (in the case of BR, Asp85 and Asp212) [58]. As shown in Figure 3.1, a small band appears at  $1639\text{ cm}^{-1}$  in the resonance Raman spectrum of BR, which has been previously assigned to the SB C=N stretching mode ( $\nu_{\text{C=N}}$  of  $1639\text{ cm}^{-1}$ ) [59]. In contrast, a band appears at  $1646\text{ cm}^{-1}$  in *CaChR1* and at an even higher frequency,  $1659\text{ cm}^{-1}$ , in the case of *CrChR2* [28].

To further confirm the assignment of the  $1646\text{ cm}^{-1}$  band in *CaChR1*, D–H exchange was performed, which is expected to cause a frequency downshift [37]. In addition, the magnitude of the downshift increases with the hydrogen bonding strength of the SB [59, 60]. As seen in Figure 3.6, in the case of *CaChR1*, this downshift is  $26\text{ cm}^{-1}$  (from  $1646$  to  $1620\text{ cm}^{-1}$ ) compared to  $17\text{ cm}^{-1}$  for BR and  $28\text{ cm}^{-1}$  for *CrChR2* [28]. Thus, we concluded that *CaChR1* and *CrChR2* have stronger SB hydrogen bonds than BR. Interestingly, *NpSR11*, which as previously noted has a resonance Raman spectrum very similar to that of *CaChR1*, also has a similar H–D exchange-induced shift ( $23\text{ cm}^{-1}$ ) [61]. Other microbial rhodopsins with appreciable H–D exchange-induced shifts include green- and blue-absorbing proteorhodopsins (GPR at  $23\text{ cm}^{-1}$  and BPR at  $21\text{ cm}^{-1}$ ) [44].

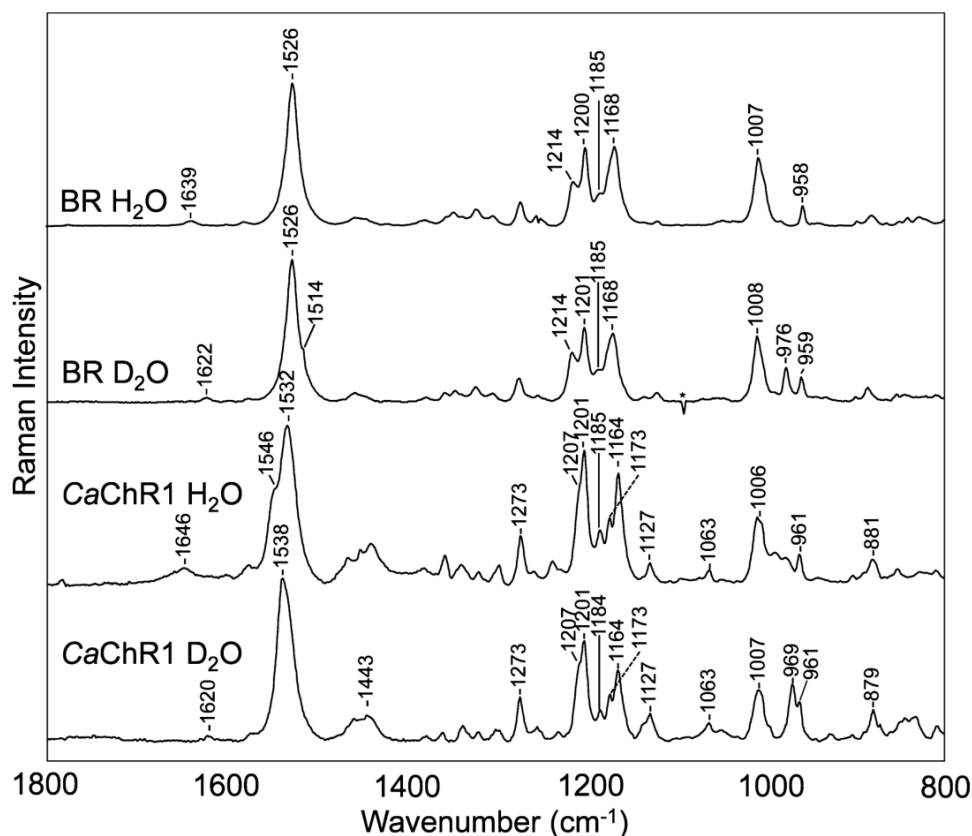


Figure 3.6: Comparison of resonance Raman spectra of BR and *CaChR1* recorded in H<sub>2</sub>O and D<sub>2</sub>O. Data were recorded using the same conditions as Figure 3.1.

### 3.1.4 Effects of pH and Anions on the Resonance Raman Spectrum of *CaChR1*

The resonance Raman spectrum of *CaChR1* remains largely unaltered over a wide pH range (Figure 3.8), including the configurationally sensitive fingerprint region. However, curve fitting the main ethylenic band reveals it undergoes a monotonic downshift of approximately 2–3 cm<sup>-1</sup> with a decrease in pH from pH 9 to 2 (Figure 3.7), which corresponds to a red shift of  $\lambda_{\text{max}}$  of approximately 8–12 nm based on the correlation shown in Figure 3.4.

This is fully consistent with the visible absorption changes observed for pH titration of *CaChR1* in detergent where three pK<sub>a</sub> values are found at pH 9, 5.5, and 2 [32]. Although the pK<sub>a</sub> values are expected to be somewhat shifted upon comparison of membrane-



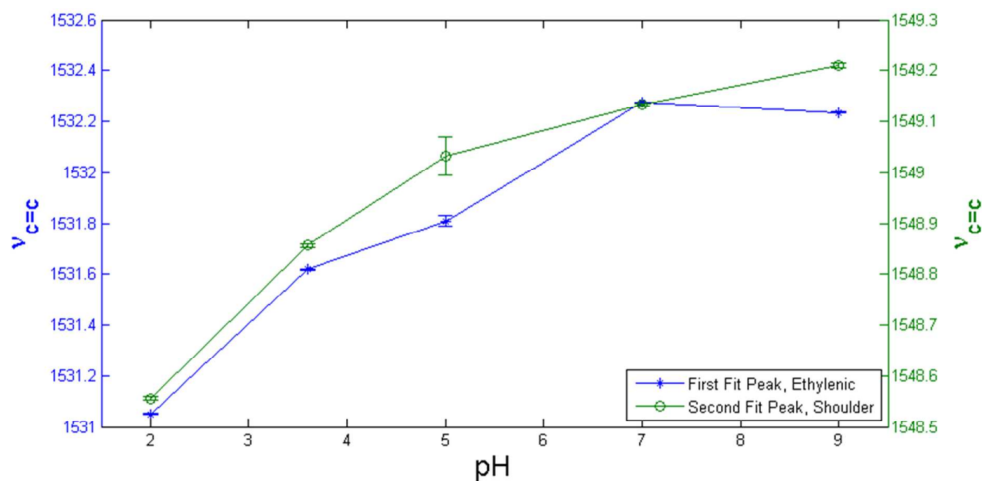


Figure 3.7: The two component bands of the ethylenic region (main peak in blue and shoulder in green) were fit using Grams AI for each of the pH values reported in Figure 3.8 and plotted as a function of pH. An example of a single fit is provided in Figure 3.5. Error bars shown indicate error in the fitted frequency from a single spectrum.

reconstituted and detergent-solubilized *CaChR1*, it is likely the red shifts we deduce from the shifts in  $\nu_{C=C}$  of only 8-12 nm correspond to the red shift observed in detergent micelles going from pH 8 to 2 and involve mainly titratable groups with  $pK_a$  values of 5.5 and 2.

The relatively small downshift of the ethylenic stretching frequency and insensitivity in other regions such as the fingerprint of the *CaChR1* resonance Raman spectrum between pH 9 and 2 are very unusual. For example, the primary counterion, Asp85, in BR undergoes a protonation below pH 3 that causes a pronounced red shift in  $\lambda_{max}$  from 570 to approximately 600 nm and a downshift in  $\nu_{C=C}$  from 1527 to 1518  $cm^{-1}$  [62]. This effect can be partially explained if the homologous residue Glu169 in *CaChR1* is already protonated at pH <9 as recently predicted on the basis of visible absorption pH titration studies [32]. However, at lower pH values, one might then expect that a second counterion (i.e., Asp299) undergoing protonation would cause a red shift larger than that observed as discussed below.

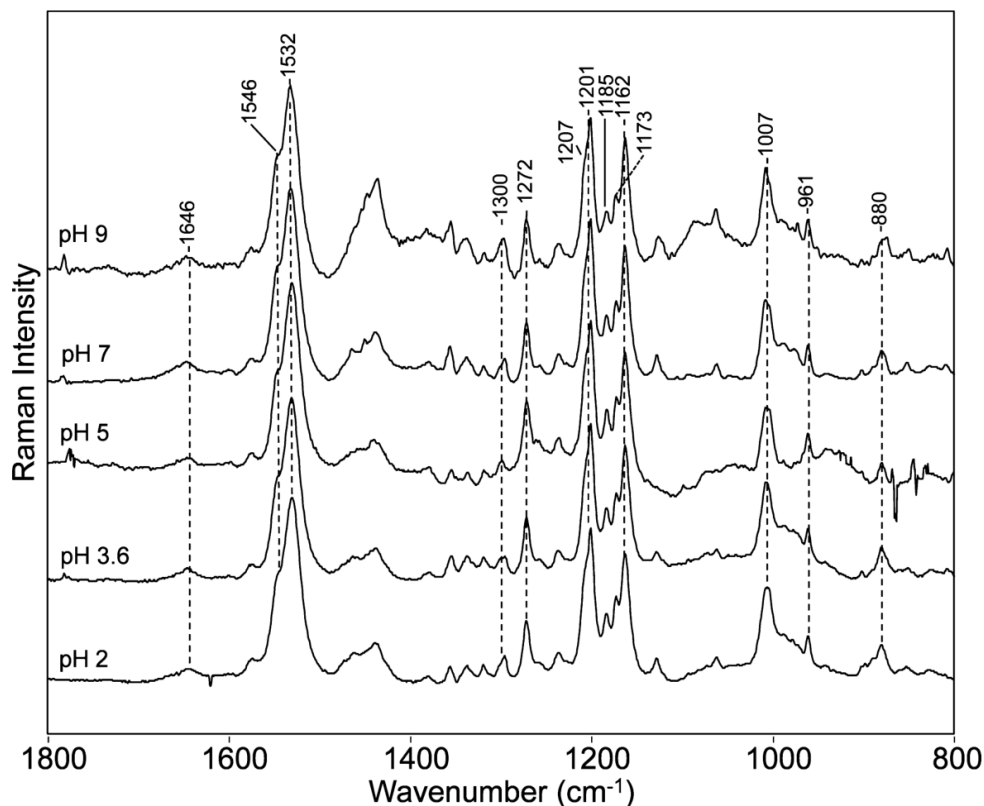


Figure 3.8: Resonance Raman spectra of *CaChR1* recorded at various pH values ranging from 2 to 9. All conditions used for RRS were the same as those for Figure 3.1.

### 3.1.5 The Effects of Anion Exchange on the PSB

The effect of changing the anion species from  $\text{Cl}^-$  to  $\text{SO}_4^{2-}$  at pH 3 was also measured. As shown in Figure 3.9, increasing the NaCl concentration from 10 mM to 2 M or switching to 1 M  $\text{Na}_2\text{SO}_4$  has little effect on the ethylenic or fingerprint region, indicating that an anion does not interact closely with the SB proton at this pH. Note that contributions from opsin are also detected in the 2 M NaCl spectrum as apparent from bands appearing at 1652, 1450, and 1003  $\text{cm}^{-1}$  that are assigned to the amide I, methyl, and phenylalanine vibrations, respectively (for example, see ref [57]). In the case of the  $\text{Na}_2\text{SO}_4$  spectrum, opsin contributions were partially removed by subtracting the spectrum of *CaChR1* opsin obtained after bleaching of the chromophore due to prolonged illumination. In addition, the band at 961  $\text{cm}^{-1}$  is assigned to a sulfate vibration.

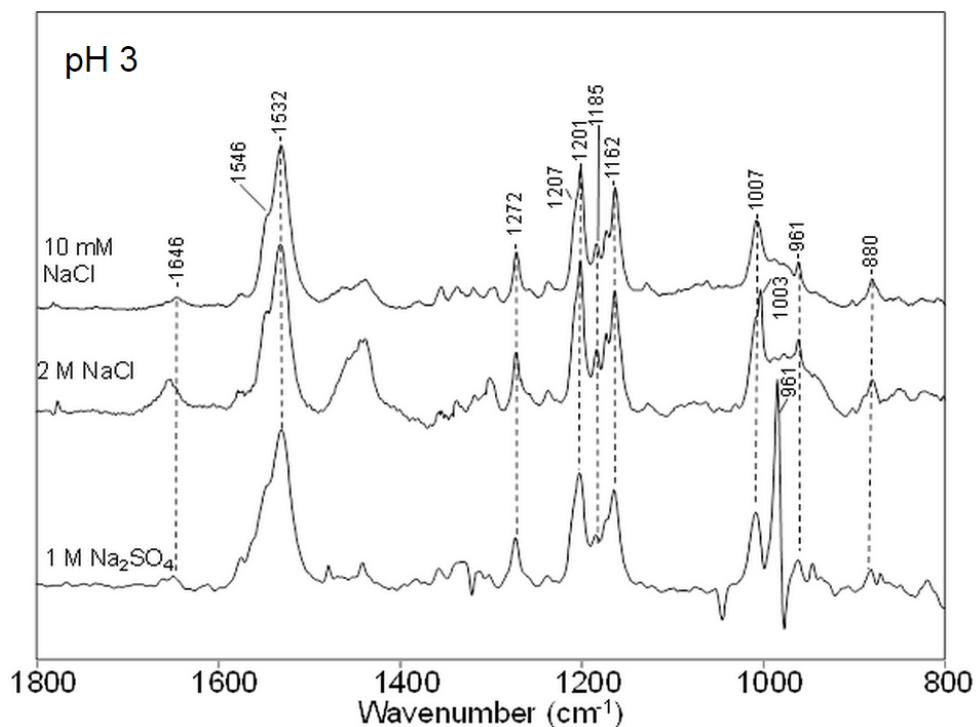


Figure 3.9: Effects of salt concentration and anion species on the RRS of *CaChR1* at pH3. All conditions used for RRS were the same as described in Figure 3.1. Top trace is pH3.6 spectrum shown in Figure 3.8.

### 3.1.6 Effects of Substitution of Glu169 and Asp299

The *CaChR1* residues homologous to the SB counterions Asp85 and Asp212 in BR are Glu169 and Asp299, respectively. These residues are located in helices C and G, respectively, and comprise along with a nearby water molecule (W402) the SB counterion complex. Conservative substitution of Glu169 with a neutral residue (Glu to Gln), based on effects of such substitutions in BR and other type 1 rhodopsins, would be expected to cause a substantial red shift of  $\lambda_{\max}$  and upshift of  $\nu_{C=C}$ . For example, the  $\lambda_{\max}$  of the mutant BR D85N (Asp to Asn) is red-shifted approximately 30 nm and the  $\nu_{C=C}$  is downshifted 7  $\text{cm}^{-1}$  [63], similar to the case for the acidified or deionized blue membrane [62]. In addition, the full width at half-maximum of D85N increases significantly from 19 to 31  $\text{cm}^{-1}$ , which was attributed to an increase in 13-*cis* retinal content [63]. Similar effects result from the

low pH or deionization-induced purple-to-blue transition of BR in which Asp85 is neutral due to protonation [62]. In both cases, a mixture of all-*trans* and 13-*cis* retinal as in dark-adapted BR was deduced from the resonance Raman spectrum. One exception to this type of effect is Anabaena sensory rhodopsin (ASR), in which the Asp212 homologue is replaced with a neutral threonine [64].

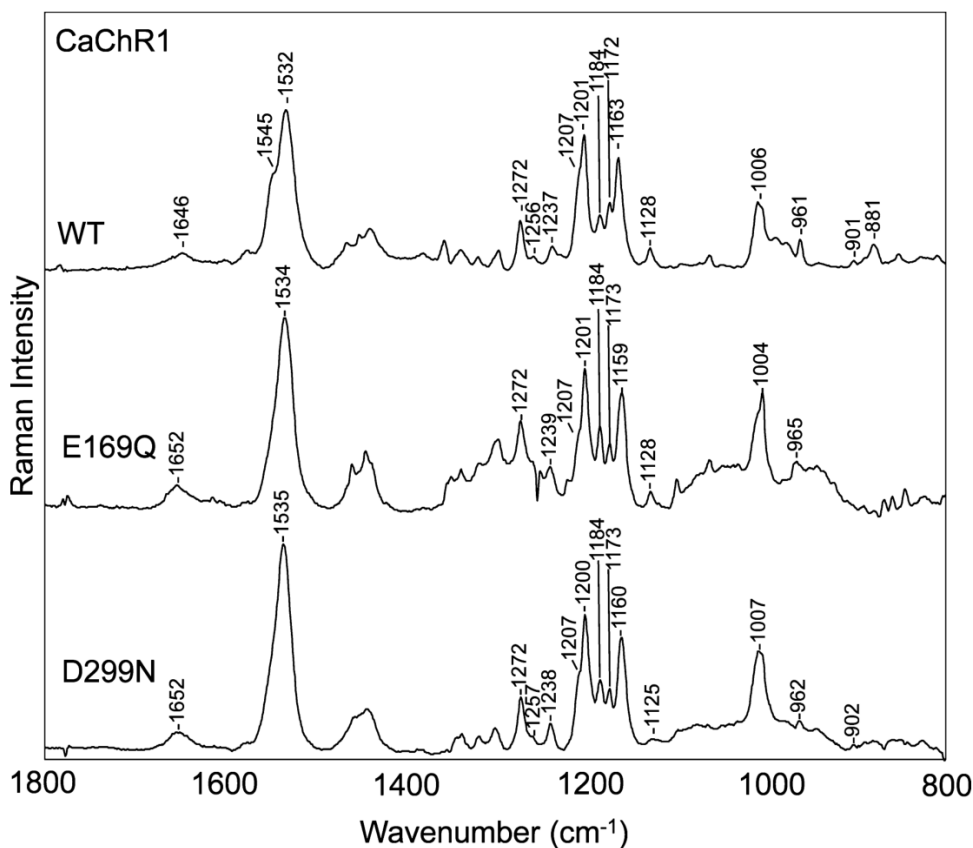


Figure 3.10: Resonance Raman spectra of *CaChR1* and mutants E169Q and D299N. All conditions used for RRS were the same as those for Figure 3.1.

In contrast, the  $\nu_{C=C}$  of the ethylenic band for the *CaChR1* E169Q mutant upshifts approximately  $2 \text{ cm}^{-1}$  relative to the WT and does not undergo a change in the intensity of the full width at half-maximum (Figure 3.10). On the basis of curve fitting (see Figure 3.4), the full width at half-maximum of the main component band and shoulder-fit band are 21 and  $11 \text{ cm}^{-1}$  versus 20 and  $15 \text{ cm}^{-1}$  for WT and E169Q, respectively. As predicted by

the inverse relationship between  $\lambda_{\max}$  and  $\nu_{C=C}$  (Figure 3.4), in contrast to the significant red shift in BR D85N, a blue shift of  $\lambda_{\max}$  by approximately 10 nm should occur, which is confirmed by visible absorption measurement in both films and membrane suspensions (data not shown) and also is in agreement with E169Q *CaChR1* solubilized in detergent [32].

The C–C stretch fingerprint region indicates that E169Q remains mainly in an all-*trans* configuration with only a small increase observed in the intensity of the 1184  $\text{cm}^{-1}$  band as compared, for example, to that of acid blue or deionized BR for which significant increases in intensity of a band near 1184  $\text{cm}^{-1}$  are observed [62]. We conclude that the small blue shift observed in *CaChR1* E169Q is not due to increased 13-*cis* retinal content in the mutant masking a red-shift of the all-*trans* component. It is also noted that the SB C=N stretch frequency upshifts to 1652  $\text{cm}^{-1}$  even though neutralization of this homologous residue in other microbial rhodopsins causes a downshift [63]. For example, in D85N the SB C=N downshifts 6  $\text{cm}^{-1}$  [63] and in acid blue or deionized BR the SB C=N downshifts approximately 10  $\text{cm}^{-1}$  [62].

Interestingly, almost identical changes compared to WT occur in the resonance Raman spectrum of the mutant D299N. For example, the  $\nu_{C=C}$  upshifts by about 3  $\text{cm}^{-1}$ , slightly more than that of E169Q, which is confirmed by a slightly greater blue shift of the visible  $\lambda_{\max}$  [32]. Like that of E169Q, the  $\nu_{C=N}$  upshifts to 1652  $\text{cm}^{-1}$ , and the fingerprint region remains substantially unchanged.

### 3.2 Conclusions from Raman Studies

The light-gated channel activity of heterologously expressed ChRs in neurons has led to significant interest in their structure and molecular mechanisms of action [65]. Despite this interest, relatively few studies have focused on the molecular mechanism of ChRs besides *CrChR2*. However, ChRs display considerable diversity even within the same genus of *Chlamydomonas*. This includes differences in visible absorption, photocycle and current kinetics, light inactivation, pH sensitivity, and channel conductivity [66]. In this work, we used near-IR confocal RRS to study the chromophore and electrostatic interactions near the

protonated SB of a ChR1 from *C. augustae* (*CaChR1*). On the basis of these measurements and earlier studies, several conclusions about the retinal structure in *CaChR1* and the interaction of the nearby counterions Glu169 and Asp299 with the SB have been reached.

### 3.2.1 Light-Adapted *CaChR1* has an All-*Trans* Retinal Composition Similar to That of BR and *NpSRII* in Contrast to That of *CrChR2*

RRS indicates that the retinal chromophore of *CaChR1* is similar to the structure and isomeric composition of light-adapted BR. Recent FTIR difference measurements of the *CaChR1* primary photo-transition at low temperatures also confirm that *CaChR1* have a predominantly all-*trans* retinylidene chromophore in contrast to a mixed isomeric composition of the retinylidene chromophore in *CrChR2*. One difference in the chromophore configuration of *CaChR1* and BR may be near the C<sub>10</sub>–C<sub>11</sub> portion of the retinal that has a slightly lower frequency for the fingerprint band assigned to that mode in *CaChR1* compared to BR (see Figure 3.1). However, this effect may also be due to differences in the interaction of the protein with other regions of the retinal chromophore, causing mode mixing to which this band is very sensitive [16]. Importantly, these results with *CaChR1* contrast with RRS measurements of *CrChR2*, which contains bands in the fingerprint region reflecting a mixture of all-*trans* and 13-*cis* retinal-containing species (see Figure 3.1) and earlier results [45, 67].

Even more striking are the nearly identical resonance Raman spectra of *CaChR1* and the phototaxis receptor *NpSRII* (Figure 3.1). This spectrum recorded using 785 nm excitation is almost identical to the resonance Raman spectra reported previously using 514 nm excitation and a spinning cell designed to eliminate contributions from long-lived intermediates of the *NpSRII* photocycle (M, N, and O) and minimize contributions from K (0.1%) and L (1.3%) [16]. This similarity strongly indicates that both microbial rhodopsins have very similar retinal structures. Furthermore, a combined quantum chemical/normal mode approach indicates that the spectrum of *NpSRII* best reflects an all-*trans* 15-*anti* protonated Schiff base (PSB) structure similar to that of BR. However, differences with the BR

resonance Raman spectrum such as shifts in band frequency and intensity in the ethylenic and fingerprint region were attributed to a stronger interaction of the counterion(s) with the SB in *NpSR*II, thus also explaining the blue-shifted  $\lambda_{\max}$  relative to that of BR [16]. On this basis, we surmise that the differences between the resonance Raman spectra of BR and *CaChR*1 are also due to differences mainly near the SB region of the chromophore and its interaction with its counterion(s).

Several other features also suggest the similarity of the *CaChR*1 and *NpSR*II retinal chromophores. As discussed below, *NpSR*II and *CaChR*1 both have much stronger hydrogen bonding of the SB than BR [16]. In addition, the absence of dark adaptation in both proteins indicates that the binding pocket does not easily accommodate a 13-*cis* retinal configuration as previously suggested for *NpSR*II based on measurement of the rate of 13-*cis* retinal regeneration [41]. It is also noted that like *CaChR*1, the ethylenic band of *NpSR*II measured by RRS was fit by two subcomponent ethylenic bands both attributable to the same all-*trans* retinal species [16].

Confirming the absence of significant light–dark adaptation, we observed no significant resonance Raman spectral changes upon green light illumination during the acquisition of resonance Raman spectra (Figure 3.3). Furthermore, the 785 nm laser excitation used to record the resonance Raman spectra is far from the visible absorption  $\lambda_{\max}$  of *CaChR*1 near 525 nm and hence not likely to produce photocycle intermediates even in cases where the longest photointermediate decay time is a few seconds. As noted above, the similarity of the resonance Raman spectra of *NpSR*II that has a slowly decaying O intermediate of a few seconds recorded using photostationary 785 nm excitation here and under conditions where the photointermediates are minimized [16] also supports this conclusion.

### 3.2.2 The Schiff Base Has Hydrogen Bonding Stronger Than That of BR

The RRS-measured H–D exchange-induced downshift of the C=N vibrational mode ( $\nu_{C=N}$ ) of the retinylidene SB in *CaChR*1 indicates that the SB forms a hydrogen bond that is stronger than that of BR. A similar conclusion was also reached on the basis of the H–D

exchange-induced shift for the C=N vibrational mode of *CrChR2* [28]. One possible explanation is suggested by the crystal structure of the C1C2 chimera that shows a movement of water molecule W402 found in BR away from the SB [5]. In this position, the water closest to the SB in *CaChR1* may not be able to act to soften the hydrogen bonding interaction of the counterion(s) with the SB (see below).

### 3.2.3 Glu169 Exists in a Neutral Form at Neutral pH

With a decrease in pH from 9 to 2, a red shift in  $\lambda_{\max}$  of around 8–12 nm was deduced. Furthermore, substitution of the neutral residue Gln for Glu169 caused a small upshift in  $\nu_{C=C}$  confirming a reported blue shift in  $\lambda_{\max}$  [32]. However, on the basis of the effect of neutralizing the homologous residue Asp85 in BR, a significant downshift in  $\nu_{C=C}$  and a red shift in  $\lambda_{\max}$  should occur if Glu169 functioned as the predominant SB counterion at neutral pH [58]. Furthermore, the absence of a smaller than expected red shift or even a blue shift as observed in the case of E169Q cannot be explained by postulating that the chromophore adopts a non-all-*trans* configuration (e.g., 13-*cis*) because the fingerprint region remains substantially unchanged and characteristic of an all-*trans* chromophore.

An explanation for these effects is that Glu169 has a very high  $\text{pK}_a$ . In this case, substitution with another neutral group (Gln) should not cause a red shift, and pH titration below the  $\text{pK}_a$  would also not cause a substantial change in  $\lambda_{\max}$ . In fact, the  $\text{pK}_a$  of Glu169 was determined to be near 9 in detergent micelles by pH titration of the visible absorption of *CaChR1* and the mutant E169Q [32]. *CaChR1* reconstituted in *E. coli* polar lipid membranes may have a  $\text{pK}_a$  even higher than that in detergent micelles because we do not observe a substantial blue shift in  $\lambda_{\max}$  deduced from the  $\nu_{C=C}$ . Such a  $\text{pK}_a$  shift would be expected if the surface charge near *CaChR1* were altered in these two different environments as is observed in the case the BR for the  $\text{pK}_a$  of the purple-to-blue transition [68].



### 3.2.4 Asp299 Serves as the Predominant SB Counterion over a Broad pH Range

The *CaChR1* SB has a hydrogen bond strength that is greater than that of BR (see the above, Section 3.2.2), yet Glu169, the residue homologous to Asp85 that in BR acts as the primary counterion, exists in a neutral form (Section 3.2.3) over a wide pH range. This indicates that another counterion or counterion complex interacts strongly with the SB. An attractive candidate is Asp299, which is homologous to Asp212 in BR and exists in an ionized form along with Asp85.

One problem with this model, however, is that the  $pK_a$  for Asp299 was determined on the basis of site-directed muta-genesis and pH titrations to be near 5 [32]. This would thus indicate that below pH 5, both Glu169 and Asp299 exist in a neutral form, providing no effective counterbalancing negative anionic charge for the positively charged SB. Under these circumstances, we would expect to observe a downshift of  $\nu_{C=C}$  much larger than that observed ( $1-2 \text{ cm}^{-1}$ ) upon titration from pH 7 to 2 (corresponding to only a 4–8 nm red shift in  $\lambda_{\max}$ ) (see Figure 3.4), in good agreement with the reported red shift for *CaChR1* in detergent over the same pH range [32]. Furthermore, the  $\nu_{C=N}$  does not shift appreciably over this pH range, which would be expected if the SB counterions were neutral. For example, neutralization of the primary BR counterion, Asp85, by either lowering the pH or substituting a neutral residue results in 7 and 6–10  $\text{cm}^{-1}$  downshifts in  $\nu_{C=C}$  and  $\nu_{C=N}$ , respectively [62, 63].

It is likely for this reason that another source(s) of negative charge compensation near the PSB comes into play at very low pH in *CaChR1*. One possibility is that a negative anion enters the active site of *CaChR1* and serves as the counterion to the PSB. FTIR difference studies indicate that movement of a  $\text{Cl}^-$  ion to near the PSB occurs in BR when both counterions are neutral near pH 0 [69]. On the basis of resonance Raman spectra, the retinal chromophore for this acid form of BR has an all-*trans* retinal chromophore very similar to light-adapted BR, including similar ethylenic and C=N SB stretching frequencies [62]. Entry of an anion has also been reported in sensory rhodopsin I from *Salinibacter ruber* (*SrSRI*)

but near the  $\beta$ -ionone ring of the retinal chromophore [70,71]. However, no spectral changes in the resonance Raman spectra were observed for *CaChR1* when measured in 2 M NaCl or 1 M Na<sub>2</sub>SO<sub>4</sub>, as described in the above Section 3.1.4. In addition, no difference in the visible absorption was found between mutants E169Q and D299N for 100 mM NaCl and Na<sub>2</sub>SO<sub>4</sub> solutions [32]. Thus, this option seems unlikely.

A second possibility is that other negatively charged residues located nearby the PSB assume the role of counterion(s). In the case of ChRs, there are several residues with yet unknown pK<sub>a</sub> values that could serve this role. For example, Glu136 (Glu90 in *CrChR2*) located on helix B is approximately 6 Å from the PSB in the C1C2 structure and may be pulled closer below pH 5 when both Glu169 and Asp299 are expected to be neutral. Other residues such as Glu128 and Glu129 also on helix B are possible candidates but are located >9 Å from the PSB [5].

Another possible explanation for the absence of larger changes in the resonance Raman spectra at lower pH is that protonation of Asp299 causes a concerted deprotonation of Glu169, which then becomes the predominant counterion for the SB. Such a deprotonation was also proposed to occur when Asp299 is replaced with Asn, to explain the apparent ability of Glu169 to function as the SB proton acceptor in D299N at neutral pH [32]. Such an effect might be caused by a strong mutual electrostatic interaction among Glu169, Asp299, and the SB, which acts to maintain overall charge neutrality in the active site between the positively charged SB and the Glu169Asp299 complex. Such a direct interaction is suggested by the position of an internal water molecule in C1C2 that is similar to that of W402 in BR but is located 4.4 Å from the SB compared to 2.8 Å in BR [5]. Because W402 in BR is in a position to mediate the electrostatic interaction of the SB with Asp85 and Asp212, moving this water farther away may allow more direct interactions of these residues with the SB. In fact, on the basis of low-temperature FTIR measurements of C1C2, it was concluded recently that Glu162, the homologue of Glu169 in *CaChR1*, interacts directly with the PSB without the intervening water molecule found in BR [72]. However, this model contrasts with the one we propose for *CaChR1* where Glu169 exists in a protonated form and Asp299

acts as the predominant counterion for the PSB at neutral pH.

## Chapter 4

### The $P_0$ to $P_1$ phototransition: The Initial Photoproduct and the Assignment of Chromophore, Protein, and Water Vibrations.

#### 4.1 FTIR Difference Spectroscopy of *CaChR1* at 80 K

As described in the Materials and Methods section, films of *CaChR1*, *CrChR2*, *NpSR11*, BR and various mutants were produced by drying approximately 50  $\mu\text{L}$  of stock solution onto a CaF or BaF window under a stream of argon or nitrogen. The samples were then sealed on the Optistat DN2 Sample rod and loaded into the Optistat DN2 Cryostat system used with the BioRad FTIR. The samples were cooled in under 5 minutes to below 273 K with helium exchange gas. Light adapting illumination was used for BR until the sample was below 273K. FTIR difference spectra were acquired at 80 K using steady state illumination conditions (via ThorLabs LED sources) appropriate for photoproduct formation and photoreversal. A typical cycle consists of 1 minute dark acquisition, 1 minute with illuminated acquisition to drive intermediate production, 1 minute with dark acquisition, and 1 minute with illuminated acquisition to photoreverse where 1 minute of acquisition is the average of approximately 200 double-sided, forward-backward movements of the interferometer. All data presented were formed from >30 such cycles with many data sets being the average of several hundred cycles.

In addition, and as described previously, H-D and  $\text{H}_2\text{O}$ - $\text{H}_2^{18}\text{O}$  substitutions are produced by drying films out of their native buffer and rehydrating the film with  $\text{D}_2\text{O}$  or  $\text{H}_2^{18}\text{O}$  through the vapor phase in a sealed window-o-ring-window construction. The sample is then opened, re-dried in a dry box, and again rehydrated through the vapor phase. This procedure is repeated at least 4 times with the final, hydrated sample being sealed for data acquisition.

#### 4.1.1 The Primary Phototransition of *CaChR1* Involves all-*trans* to 13-*cis* chromophore isomerization

The difference spectrum of the  $P_0 \rightarrow P_1$  photointermediates of *CaChR1* is similar to the difference spectrum of  $BR \rightarrow K$  [73–76] for bands assigned to the retinal chromophore as shown in Figure 4.1. In the ethylenic C=C stretching region from 1500–1600  $\text{cm}^{-1}$  negative/positive bands appear at (-)1535 and (+)1521  $\text{cm}^{-1}$  which are assigned to the ethylenic C=C stretching modes of the retinal chromophore for the initial dark-state,  $P_0$  and the  $P_1$  photointermediate, respectively (see below). The negative/positive ethylenic bands in *CaChR1* are upshifted to a higher frequency compared to BR (1529/1514  $\text{cm}^{-1}$ ) as expected due to *CaChR1*'s blue-shifted visible absorption ( $\lambda_{\text{max}} = 523 \text{ nm}$ ) [32] relative to that of light-adapted BR ( $\lambda_{\text{max}} = 570 \text{ nm}$ ) and is in agreement with the inverse linear relationship existing between  $\lambda_{\text{max}}$  and  $\nu_{C=C}$  for most microbial and animal rhodopsins [77–79]. In addition, the negative band at 1535  $\text{cm}^{-1}$  is close to the frequency assigned to the ethylenic mode of *CaChR1* using Resonance Raman Spectroscopy [80]. The slight increase in frequency compared to the RRS (1532  $\text{cm}^{-1}$ ) is expected due to splitting effects between the positive and negative ethylenic bands in the FTIR-difference spectrum.

The fingerprint region (1100–1250  $\text{cm}^{-1}$ ), which reflects the mixed C–C stretching modes of the retinylidene chromophore, is, as with Raman Spectroscopy, particularly sensitive to the retinal isomeric state [39, 81]. The RRS study provided in the previous chapter discussed bands near 1201, 1172 and 1163  $\text{cm}^{-1}$  which are highly characteristic of an all-*trans* configuration of retinal in the unphotolyzed state of *CaChR1* [80]. Negative bands appear at similar frequencies in the FTIR-difference spectrum of *CaChR1* and BR (Figure 4.1), further indicating that the primary phototransition at low temperature involves isomerization of an all-*trans* retinylidene chromophore.

The largest positive band in this region for *CaChR1* appears at 1196  $\text{cm}^{-1}$ , close to the 1194  $\text{cm}^{-1}$  band in BR assigned to the mixed stretching vibration of the 13-*cis* retinylidene chromophore [81]. Importantly, almost all microbial rhodopsins containing an essentially pure all-*trans* retinal composition display a pattern similar to *CaChR1* and BR in this region

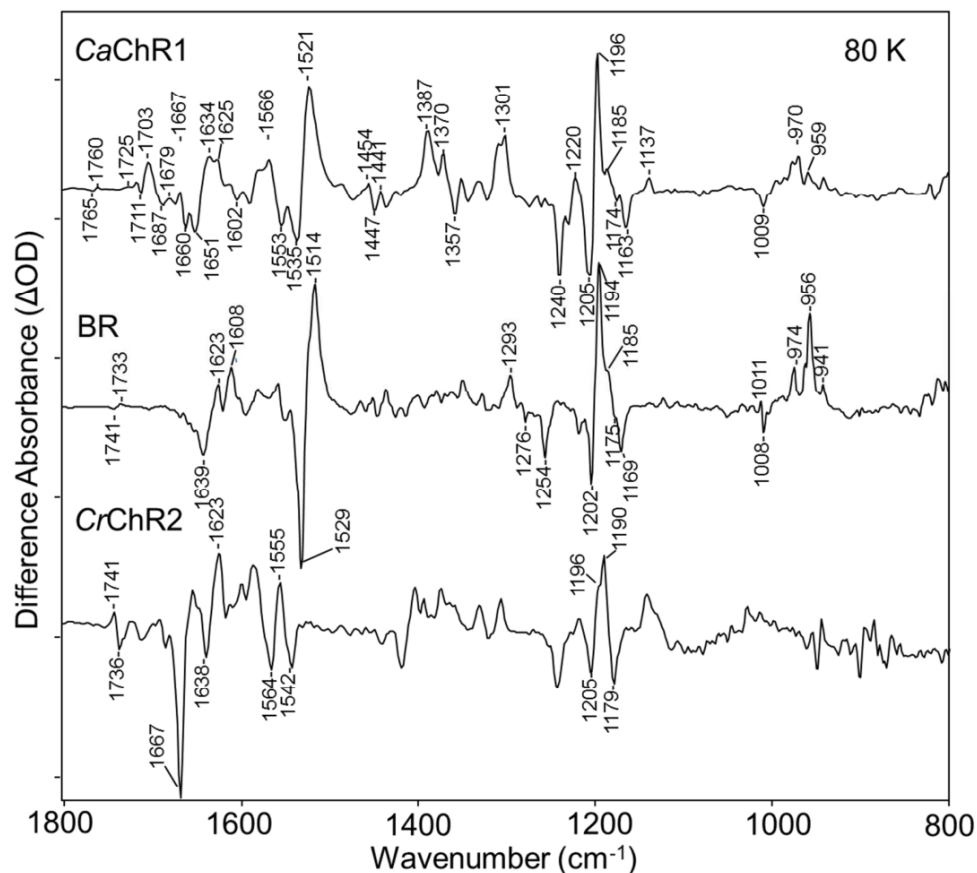


Figure 4.1: Comparison of FTIR-difference spectra for *CaChR1*, *BR*, and *CrChR2* taken at 80 K over the 800-1800  $\text{cm}^{-1}$  region. Y-axis markers indicate 2.5 mOD for *CaChR1*, 5 mOD for *BR*, and 0.6 mOD for *CrChR2*.

with two negative bands near 1200 and 1165-1170  $\text{cm}^{-1}$  and a positive band near 1195  $\text{cm}^{-1}$  including arachaeorhodopsin-3 (AR3) [82], green- and blue-absorbing proteorhodopsin (GPR, BPR) [77, 83], *NpSR*II [84], and halorhodopsin from *Halobacterium salinarum* (*HsHR*) [85].

It is important to note that the upshift in frequency of the negative band at 1205  $\text{cm}^{-1}$  compared to the RRS spectrum (1201  $\text{cm}^{-1}$ ) is most likely due to overlap/splitting effects with the positive band at 1196  $\text{cm}^{-1}$ . Overall, the similarity of the fingerprint region for *CaChR1* and *BR* firmly establishes that the chromophore undergoes an all-*trans* to a 13-*cis* isomerization as previously established for *BR* on the basis of RRS studies of isotopic labeled retinals [39, 81].

In contrast, a significantly different pattern is observed in the fingerprint region for the 80 K FTIR-difference spectrum of *CrChR2* (Figure 4.1). Although a negative band still appears at  $1205\text{ cm}^{-1}$  and a positive shoulder at  $1196\text{ cm}^{-1}$ , a more positive band appears at  $1190\text{ cm}^{-1}$  and the negative band near  $1165\text{--}1170\text{ cm}^{-1}$  is replaced by a negative band at  $1179\text{ cm}^{-1}$ . These alterations are most likely explained by the presence of 13-*cis* retinal in both the dark and light-adapted state of *CrChR2* [28] which also isomerizes during the primary phototransition and contributes to the difference spectrum in this region. Indeed, a similar conclusion was reached from the FTIR-difference spectrum for the primary phototransition of blue absorption proteorhodopsin (BPR) [83], where a second positive band appears at  $1188\text{ cm}^{-1}$  and the band between  $1165\text{--}1170\text{ cm}^{-1}$  is absent. Supporting this conclusion, a positive band appears in the RRS of *CrChR2* [28, 80] at  $1185\text{ cm}^{-1}$  which most likely accounts for the negative band at  $1179\text{ cm}^{-1}$  in the FTIR-difference spectrum, which is downshifted due to spectral splitting with the positive band at  $1190\text{ cm}^{-1}$ . Note that while these differences might be attributed to the fact that *CrChR2* was reconstituted in DMPC and *CaChR1* in ECPL (see Materials and Methods), identical results were obtained for *CrChR2* reconstituted in ECPL (Figure 4.2).

Evidence for isomerization of a pure all-*trans* retinal in the primary phototransition of *CaChR1* and mixed all-*trans* /13-*cis* isomerization in *CrChR2* can be found from photoreversibility experiments. The *CrChR2* difference spectrum shown in Figure 4.1 is the average of many cycles of differences involving photo-excitation/reversal using 455 nm and 530 nm illumination light as described in Materials and Methods. The first push difference consisted of recording a spectrum after cooling from dark state and subtracting from a spectrum recorded after the sample was illuminated with a 505 nm LED in the case of *CaChR1* and a 455 nm LED in the case of *CrChR2*. In contrast to the photo-excitation/reversal experiments, the difference spectrum recorded for only the first push from the dark-adapted state to  $P_1$  (using only 455 nm illumination), differs somewhat in the fingerprint region, with a negative band appearing near  $1184\text{ cm}^{-1}$  instead of  $1179\text{ cm}^{-1}$  (see Figure 4.3). An almost identical difference spectrum involving only the first push was also reported earlier

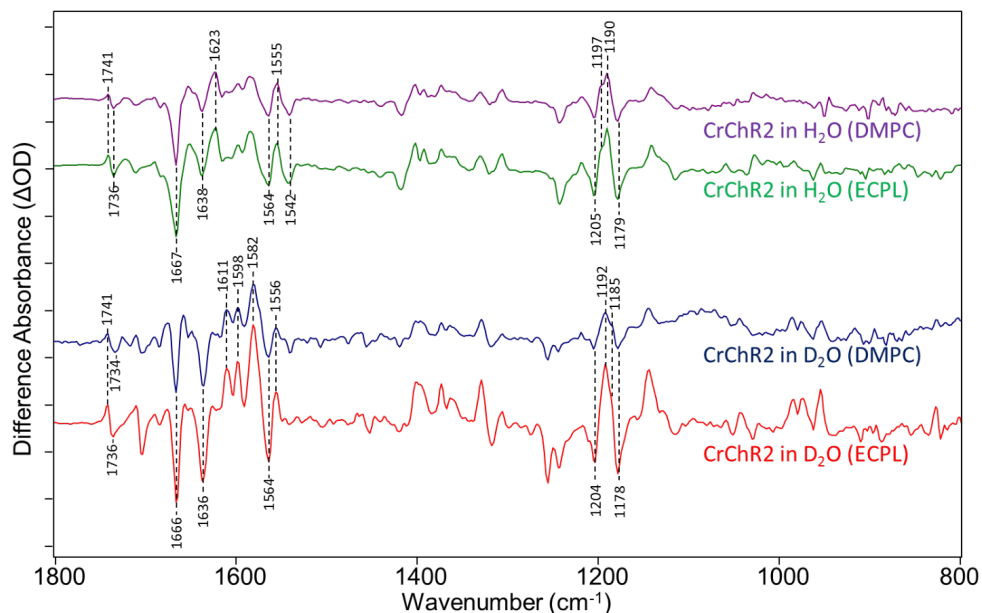


Figure 4.2: Comparison of *CrChR2* reconstituted in DMPC (purple and blue traces) and ECPL (green and red traces) in both  $\text{H}_2\text{O}$  (top two traces) and  $\text{D}_2\text{O}$  (bottom two traces) over the  $800\text{--}1800\text{ cm}^{-1}$  region at  $80\text{ K}$  ( $\text{P}_0\rightarrow\text{P}_1$ ). Y-axis markers are approximately  $0.5\text{ mOD}$  for the  $\text{H}_2$  data and  $0.2\text{ mOD}$  for the  $\text{D}_2\text{O}$  data.

for *CrChR2* at  $80\text{ K}$  [46] despite the fact that it was in a detergent micellar form. This indicates that the first push at low temperature involves isomerization of even more *13-cis* retinal since the  $1185\text{ cm}^{-1}$  band is highly characteristic of this isomer [39, 81]. Consequently, the photoproduct of the *13-cis* photocycle is not fully photo-reversed and thus the average of many photocycles does not match the first push. In contrast, the first push and the average of many photocycles of *CaChR1* are nearly identical (see Figure 4.3), a consequence of the pure all-*trans* retinal content of both the dark and light-adapted *CaChR1*.

#### 4.1.2 Assignment of the Schiff Base C=N Stretch and Amide I Bands

An early FTIR-difference study of the primary phototransition of light-adapted BR using isotope labeled retinals and H-D exchange led to the assignment of the Schiff base (SB) C=N stretching mode of the K intermediate to a positive band near  $1609\text{ cm}^{-1}$  [75]. The



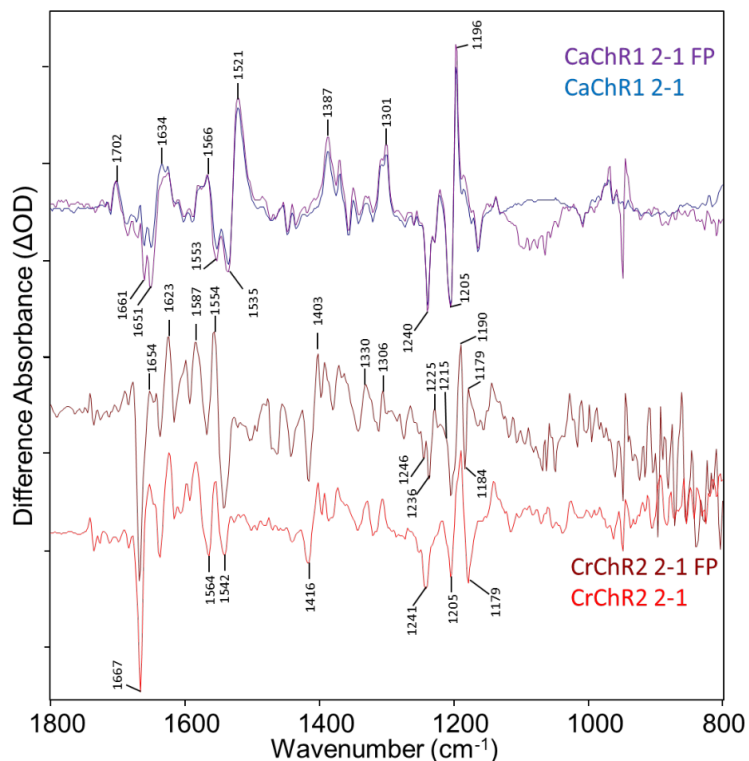


Figure 4.3: Comparison of *CaChR1* and *CrChR2* over the 800-1800  $\text{cm}^{-1}$  region both for the first push (FP: purple and maroon traces, respectively) and for many averages of  $P_0 \rightarrow P_1$  (teal and red traces, respectively). Y-axis markers are approximately 2 mOD for *CaChR1* and 0.4 mOD for *CrChR2*.

corresponding assignment of this band for the  $P_1$  intermediate has not yet been made for any ChRs. As a first step, isotope labeled retinals and H-D exchange were used to assign the  $\nu_{C=N}$  of the dark-adapted *CaChR1* which should appear as a negative band near  $1646 \text{ cm}^{-1}$  based on recent RRS measurements [29, 80]. As seen in Figure 4.4, a negative band at a slightly higher frequency ( $1650 \text{ cm}^{-1}$ ) downshifts when *CaChR1* is regenerated with both all-*trans* [ $^{15}\text{-}^{13}\text{C}, ^{15}\text{-}^2\text{H}$ ] retinal and all-*trans* [ $^{14}, ^{15}\text{-}^2\text{H}_2$ ] retinal and also upon H-D exchange which causes deuteration of the SB C=N bond (Figure 4.4, spectra D-F, respectively). Since all of these substitutions are expected to cause a downshift of the  $\nu_{C=N}$  in analogy with BR, [75] this result establishes the assignment of the negative  $1651 \text{ cm}^{-1}$  band to the C=N stretch mode. FTIR-difference spectra measured for BR regeneration

with these two isotope retinal labels also supports this conclusion (see Figure 4.5). The slightly higher frequency measured in the FTIR-difference spectrum at  $1653\text{ cm}^{-1}$  is most likely due to the overlap of hidden bands.

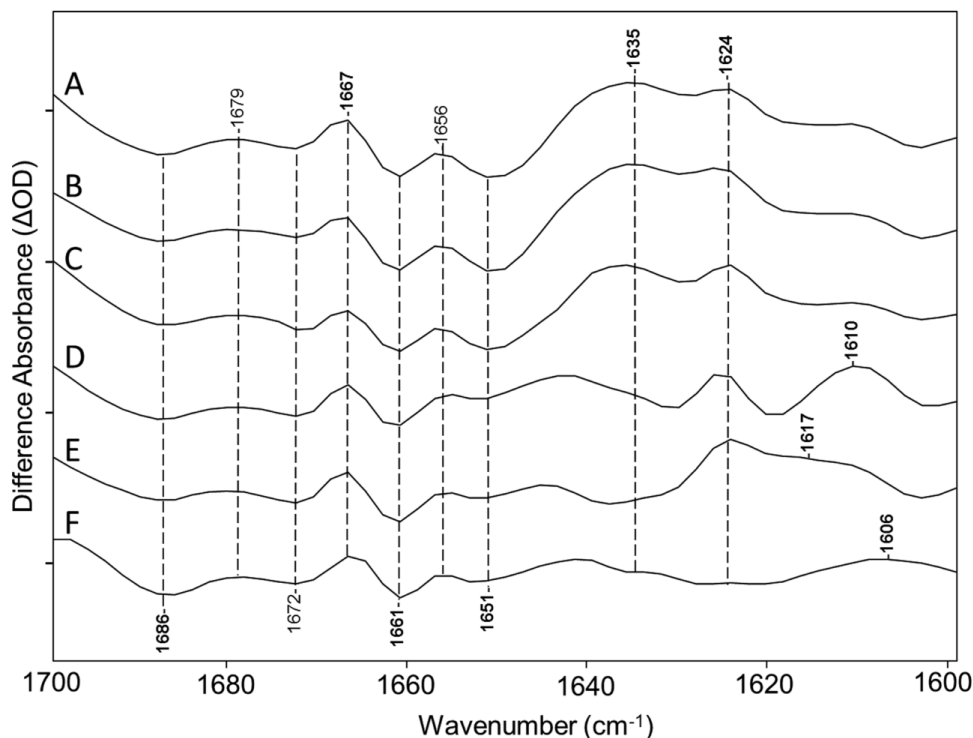


Figure 4.4: Comparison of CaChR1 recorded at 80 K over the  $1600\text{-}1700\text{ cm}^{-1}$  region for (A) untreated sample and samples subjected to bleaching and retinal regeneration with (B) A1 retinal, (C) A2 retinal, (D)  $[15\text{-}^{13}\text{C},15\text{-}^2\text{H}]$  retinal, (E)  $[14,15\text{-}^2\text{H}_2]$  retinal, and (F) CaChR1 in  $\text{D}_2\text{O}$ . Y-axis markers are approximately 1.5 mOD for all spectra.

As a control, CaChR1 regenerated with normal all-trans A1 retinal was also measured. As shown in Figure 4.4, spectrum B, no spectral changes are observed due to the regeneration procedures, as expected. Interestingly, no changes are also seen in this region for CaChR1 regenerated with A2 retinal (3,4-dehydroretinal) (Figure 4.4, spectrum C) which, unlike the isotope labels, causes a substantial red-shift in the  $\lambda_{\text{max}}$  from 525 nm with A1 retinal to 550 nm with A2, (data not shown, see ref [86]). This result indicates that the extra double bond in the A2 retinal in the  $\beta$ -ionone ring, while causing an increased electron

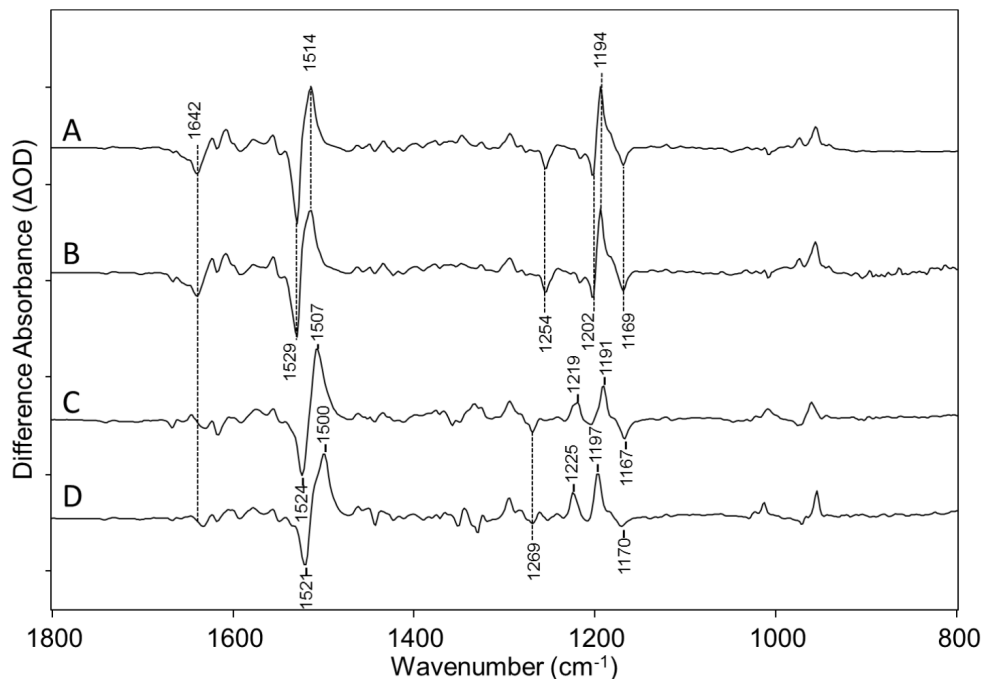


Figure 4.5: Comparison over the 800–1800  $\text{cm}^{-1}$  region of light-adapted BR for: (A) native purple membrane, and BR bleached and regenerated with (B) A1 retinal, (C) [ $^{15}\text{-}^{13}\text{C},^{15}\text{-}^2\text{H}$ ] retinal, and (D) [ $^{14},^{15}\text{-}^2\text{H}_2$ ] retinal. Y-axis markers are approximately 3 mOD for all spectra.

delocalization in the poly-ene chain, does not significantly affect the charge distribution over the C=N double bond.

On a similar basis, the positive band near  $1635\text{ cm}^{-1}$  can be assigned to the C=N stretch of the  $\text{P}_1$  intermediate which tentatively downshifts to 1610, 1617 and  $1606\text{ cm}^{-1}$  for the all-*trans* [ $^{15}\text{-}^{13}\text{C},^{15}\text{-}^2\text{H}$ ] retinal, all-*trans* [ $^{14},^{15}\text{-}^2\text{H}_2$ ] retinal and deuterated SB of the all-*trans* retinal, respectively (Figure 4.4, spectra D-F). It should be noted that, in comparison to the  $1635\text{ cm}^{-1}$  band, the  $1624\text{ cm}^{-1}$  band is insensitive to these retinal isotope alterations and most likely arises from a protein vibration (see below). One exception is the case of H-D exchange where the  $1650\text{ cm}^{-1}$  negative band is expected to downshift  $26\text{ cm}^{-1}$  based on RRS measurements [80], thus explaining the drop in intensity near  $1624\text{ cm}^{-1}$ . The smaller overall downshift of the C=N vibration from  $1651$  to  $1635\text{ cm}^{-1}$  during the *CaChR1*  $\text{P}_0 \rightarrow \text{P}_1$  transition is much smaller than in  $\text{BR} \rightarrow \text{K}$  ( $1639$  to  $1609\text{ cm}^{-1}$ ) [75] which may indicate that

the change in microenvironment near the SB occurring during this transition is smaller in *CaChR1* than in BR. Note also that no significant shift was found for the  $1635\text{ cm}^{-1}$  band for A2 retinal (Figure 4.4, spectrum C), a further indication that the electron density for the SB C=N bond is unaltered in the  $P_1$  intermediate even though the  $\lambda_{\text{max}}$  of the  $P_1$  intermediate is red-shifted.

The  $1600\text{--}1700\text{ cm}^{-1}$  region is also expected to exhibit bands due to amide I mode which consists predominantly of the C=O stretch of peptide backbone groups. In the case of *CaChR1*, several bands in this region may be due to the amide I mode including the negative band at  $1661$  and  $1687\text{ cm}^{-1}$  and the positive band at  $1667\text{ cm}^{-1}$  but the intensities of these bands are minimal compared to the large  $1667\text{ cm}^{-1}$  band in the *CrChR2* spectrum (Figure 4.1).

#### 4.1.3 Evidence for Changes in the Amide II Protein Mode in the Primary Phototransition of *CaChR1*

In addition to the negative/positive bands at  $1535$  and  $1521\text{ cm}^{-1}$  assigned to the ethylenic mode of the *CaChR1* dark-adapted state and  $P_1$  intermediate, respectively, a second prominent negative band appears in the ethylenic region at  $1553\text{ cm}^{-1}$  (Figures 4.1 and 4.6). This band may indicate the existence of a second blue-shifted species or additional ethylenic vibration from the  $523\text{ nm}$  absorbing species which contributes to the *CaChR1* photocycle and gives rise to additional ethylenic bands. A second possibility, however, is that this peak arises from alterations in the protein backbone structure. In fact, the amide II band which consists of a coupled C–N stretch and N–H bending motion of the peptide group of the protein backbone also falls in this region [87].

In order to distinguish between the two possibilities of chromophore versus protein structural changes, the two retinal isotope substitutions and substitution of the A2 retinal were analyzed in this region as shown in Figure 4.6. As expected, the negative/positive ethylenic bands at  $1535$  and  $1521\text{ cm}^{-1}$  are all altered by the isotope substitutions near the SB. As established previously, the ethylenic normal modes consist of a mixture of C=C

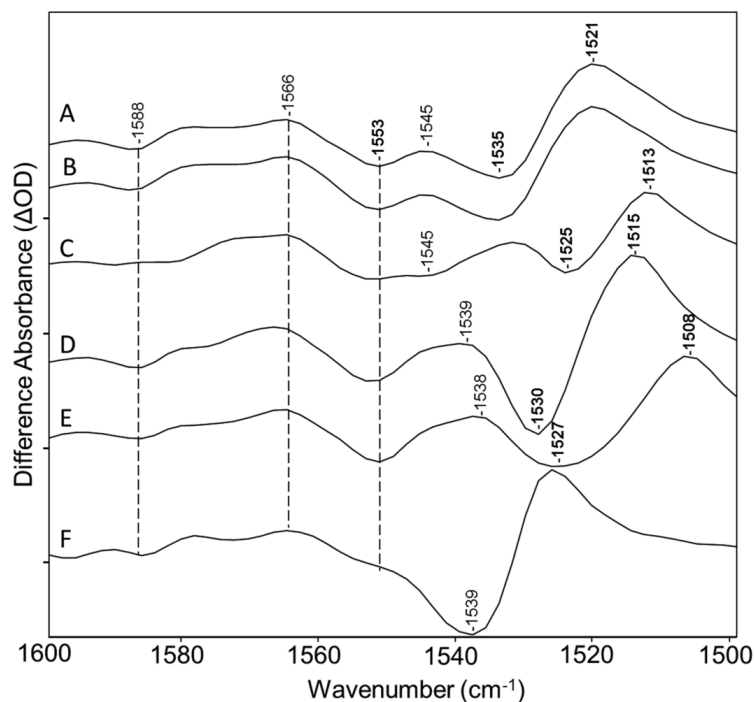


Figure 4.6: Comparison of CaChR1 recorded at 80 K over the  $1500\text{-}1600\text{ cm}^{-1}$  region. As in earlier figures (A) native *CaChR1* and *CaChR1* regenerated with (B) A1 retinal, (C) A2 retinal, (D)  $[15\text{-}^{13}\text{C},15\text{-}^2\text{H}]$  retinal, (E)  $[14,15\text{-}^2\text{H}_2]$  retinal, and (F) *CaChR1* in  $\text{D}_2\text{O}$ . Y-axis markers are approximately 1.75 mOD for all spectra.

stretches involving various double bonds including the  $\text{C}_{13}=\text{C}_{14}$  bond [37, 88] in all-*trans* and 13-*cis* protonated SB retinals. Hence, it is not surprising that the all-*trans*  $[14,15\text{-}^2\text{H}_2]$  retinal has the largest effect with an apparent shift of the negative/positive bands from  $1535/1521\text{ cm}^{-1}$  to  $1527/1508\text{ cm}^{-1}$ . In the case of all-*trans*  $[15\text{-}^{13}\text{C},15\text{-}^2\text{H}]$  retinal, the shift is smaller to  $1530/1515\text{ cm}^{-1}$ . As expected, the ethylenic bands also down shift in the A2 retinal substitution to  $1525/1513\text{ cm}^{-1}$  in agreement with the red-shift of the visible absorption [66]. Similar qualitative effects for bands assigned to the ethylenic mode in BR is also observed for the same isotope labels as shown in Figure 4.5.

In contrast to the behavior of the assigned ethylenic bands, the negative  $1553\text{ cm}^{-1}$  band is not affected by any of isotope labels or A2-retinal, strongly indicating it arises from a protein vibration. The one exception is its near disappearance upon H-D exchange. One

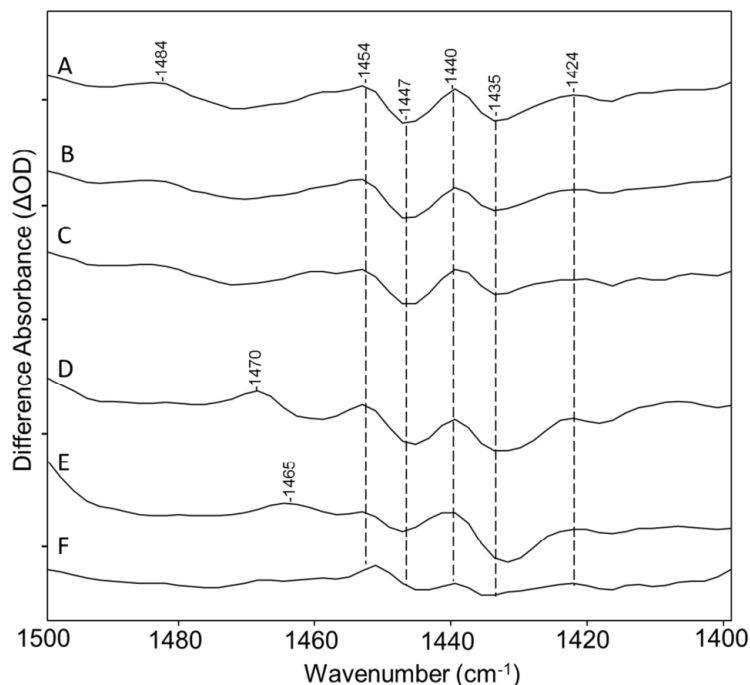


Figure 4.7: Spectra from Figure 4.4 over the 1400–1500  $\text{cm}^{-1}$  region. (A) native *CaChR1* and *CaChR1* regenerated with (B) A1 retinal, (C) A2 retinal, (D) [ $^{15}\text{-}^{13}\text{C},^{15}\text{-}^2\text{H}$ ] retinal, (E) [ $^{14},^{15}\text{-}^2\text{H}_2$ ] retinal, and (F) *CaChR1* in  $\text{D}_2\text{O}$ . Y-axis markers are approximately 1.75 mOD for all spectra.

likely explanation is that H–D exchange of peptide N–H groups causes a shift of the amide II band to the 1430–1460  $\text{cm}^{-1}$  range (often referred to as the amide II' band) as is observed in the case of BR [89]. Consistent with this explanation, a decrease in positive intensity is observed near 1440  $\text{cm}^{-1}$  in the *CaChR1*  $\text{P}_0 \rightarrow \text{P}_1$  spectrum recorded in  $\text{D}_2\text{O}$  but not in the other spectra as is shown in Figure 4.7. This could be explained by the downshift of the 1553  $\text{cm}^{-1}$  negative band to near this frequency. A complete exchange of all the peptide groups in a protein backbone, however, is not expected since many are resistant due to strong hydrogen bonding and inaccessibility to the external bulk water, especially in the case of a membrane protein. For example, BR undergoes only a partial exchange of its N–H peptide groups, unless it is fully delipidated and then reconstituted/regenerated in the presence of  $\text{D}_2\text{O}$  [89]. Under these conditions, a negative band appears in the  $\text{BR} \rightarrow \text{M}$

difference spectrum at  $1439\text{ cm}^{-1}$  which was assigned to the amide II' mode [89]. This comparison with BR as well the flattening at  $1435\text{ cm}^{-1}$  in Figure 4.7, spectrum F confirm that the  $1553\text{ cm}^{-1}$  band present in the *CaChR1*  $P_0 \rightarrow P_1$  difference is due to a protein vibration.

#### 4.1.4 Detection of Bands in the Carboxylic Acid C=O Stretching Region

A number of positive and negative bands appear in the  $1600\text{--}1700\text{ cm}^{-1}$  region in the *CaChR1*  $P_0 \rightarrow P_1$  difference spectrum (Figure 4.8). Importantly, there is a significant difference compared to *CrChR2*, where two prominent positive/negative bands appear at  $1741/1736\text{ cm}^{-1}$  but most of the bands appearing in *CaChR1* are absent (see Figure 4.1 and Figure 4.9).

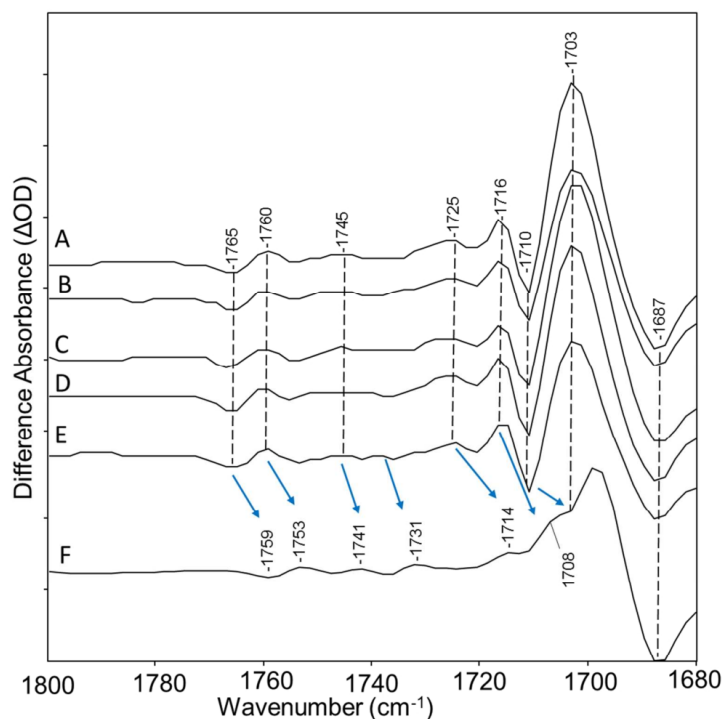


Figure 4.8: Spectra from Figure 4.4 over the  $1680\text{--}1800\text{ cm}^{-1}$  region. (A) native *CaChR1* and *CaChR1* regenerated with (B) A1 retinal, (C) A2 retinal, (D)  $[15\text{-}^{13}\text{C}, 15\text{-}^2\text{H}]$  retinal, (E)  $[14, 15\text{-}^2\text{H}_2]$  retinal, and (F) *CaChR1* in  $\text{D}_2\text{O}$ . Y-axis markers are approximately 1.75 mOD for all spectra.

Bands appearing in this region often reflect hydrogen bonding and protonation changes of individual Asp and Glu residues due to alterations in the C=O stretch frequency of the carboxylic acid groups [90]. Note however, bands near  $1700\text{ cm}^{-1}$  can also arise from the carboxyl stretch mode of Asn and Gln residues [83]. In the case of BR→K difference spectrum, a pair of weak negative/positive bands appears near  $1741/1733\text{ cm}^{-1}$  (Figure 4.1) which were assigned on the basis of site-directed mutagenesis to Asp115 [91] located near the retinal  $\beta$ -ionone ring [6]. Notably, no other bands in this region appear and thus it is unlikely that other Asp/Glu residues undergoing any significant alteration during the primary phototransition of the BR photocycle [91].

Assignment of bands in this region to Asp and Glu residues can be made by measuring the frequency downshift of the carboxylic acid C=O stretch mode that occurs upon H–D exchange (COOH→COOD). Depending on the strength of the hydrogen bonding, this exchange normally causes a downshift of the  $\nu_{C=O}$  of 1 to  $12\text{ cm}^{-1}$  with smaller shifts occurring for stronger hydrogen bonding [92]. As shown in Figure 4.8 traces A (*CaChR1* in  $\text{H}_2\text{O}$ ) and F (*CaChR1* in  $\text{D}_2\text{O}$ ), all of the bands observed in this region downshift between 5 to  $11\text{ cm}^{-1}$ . Note that at least part of the apparent downshift of the positive band at  $1703\text{ cm}^{-1}$  may be due to the overlap of hidden bands near  $1708/1703\text{ cm}^{-1}$  which have downshifted due to H–D exchange from  $1716/1710\text{ cm}^{-1}$  as indicated in *CaChR1* mutants (discussed in detail below). A smaller or even absent H–D induced shift of this band could be caused by very strong hydrogen bonding (for example see BR D96 in L intermediate [92]), absence of H–D exchange which could also occur due to very strong hydrogen bonding, or if this vibration arose from an Asn or Gln residue. Note also that the negative band at  $1687\text{ cm}^{-1}$  is unaffected by retinal changes or D–H exchange and most likely because of the lower frequency originates from an amide I mode of a peptide backbone structure which is inaccessible to H–D exchange.

The non-chromophore origin of these bands (and high degree of reproducibility) can also be seen by comparison of this region with *CaChR1* regenerated with the various retinals (Figure 4.8, spectra C-E). For example, the two retinal isotope substitutions have no effect



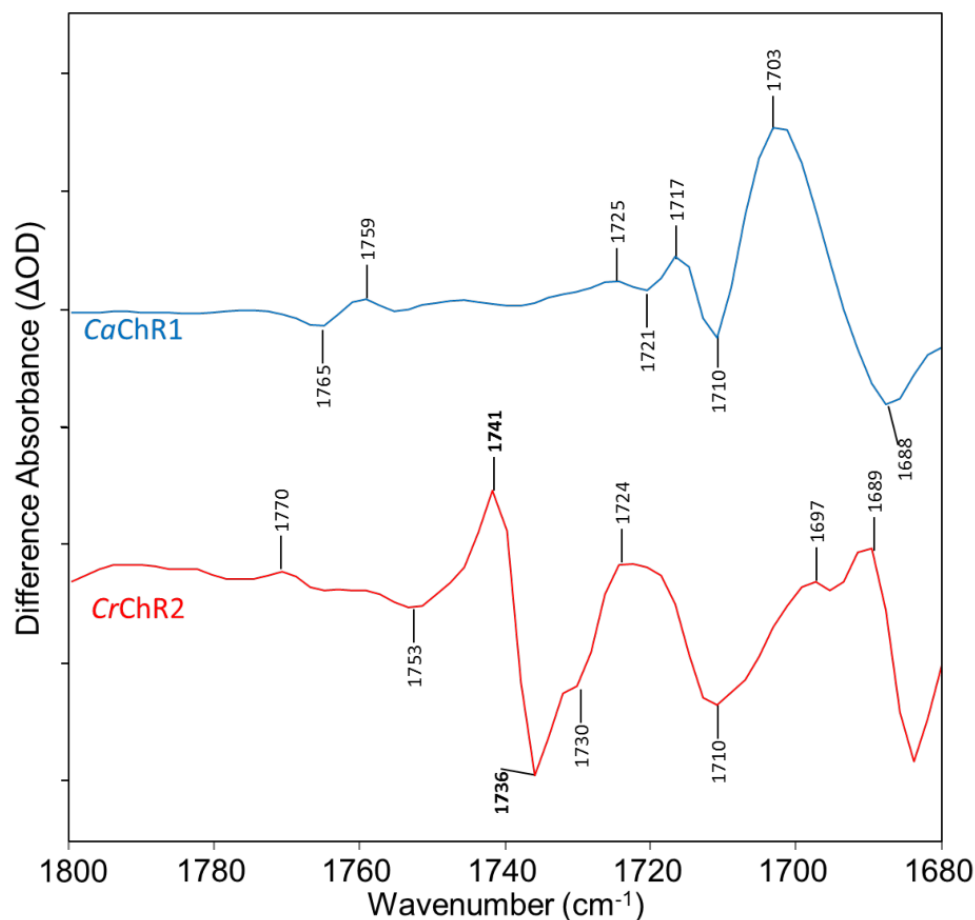


Figure 4.9: Comparison of *CaChR1* (top, in blue) and *CrChR2* (bottom, in red), over the 1680-1800  $\text{cm}^{-1}$  region at 80 K. Y-axis markers are approximately 300  $\mu\text{OD}$  for *CaChR1* and 70  $\mu\text{OD}$  for *CrChR2*.

on these bands. This insensitivity is especially notable for the case of the A2 retinal substitution (Figure 4.8, spectrum C) where the two hydrogens at the 3,4 position are eliminated in the  $\beta$ -ionone ring.

#### 4.1.5 Detection of Weakly Hydrogen Bonded Internal Water Molecules

The OH stretching mode of weakly hydrogen bonded waters is normally found in the region from 3550-3700  $\text{cm}^{-1}$  [93]. In the case of BR, negative/positive bands appear in the BR $\rightarrow$ K FTIR-difference spectrum at 3642/3636  $\text{cm}^{-1}$  with a second positive band at 3625  $\text{cm}^{-1}$ , all

of which downshift approximately 10 to 13  $\text{cm}^{-1}$  when  $\text{H}_2^{18}\text{O}$  is substituted for  $\text{H}_2\text{O}$  [94]. A similar pattern is also observed in this region, although at shifted frequencies, for green and blue proteorhodopsins [83].

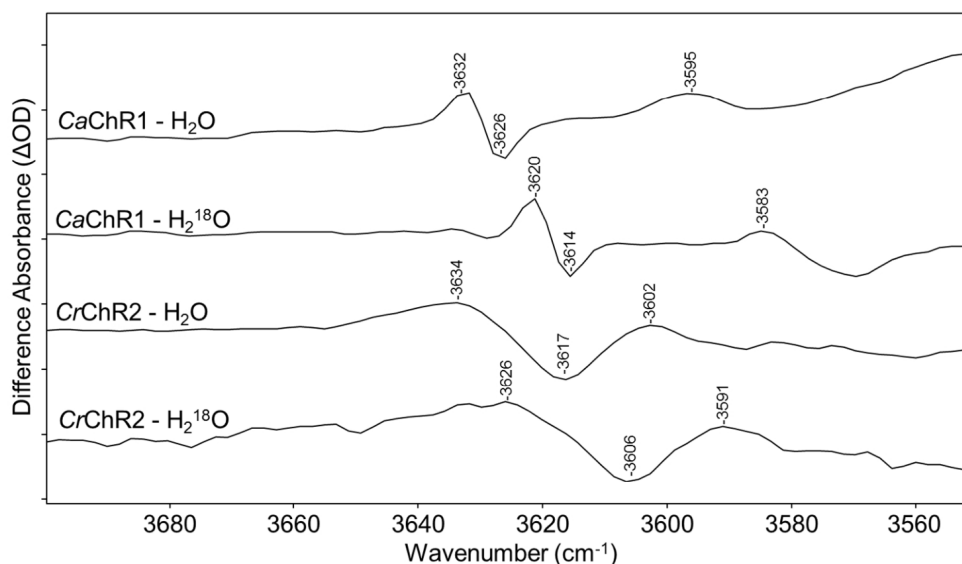


Figure 4.10: Comparison of the weak hydrogen-bonding region from 3550-3700  $\text{cm}^{-1}$  for *CaChR1* and *CrChR2* in  $\text{H}_2\text{O}$  and  $\text{H}_2^{18}\text{O}$  at 80 K. Y-axis markers are approximately 0.1 mOD for both *CaChR1* spectra and 0.05 mOD for both *CrChR2* spectra.

In the case of *CaChR1*, a different pattern is found in this region with positive/negative bands appearing at 3632/3626  $\text{cm}^{-1}$  and an additional positive band at 3595  $\text{cm}^{-1}$  (Figure 4.10). All of these bands can be assigned to one or more weakly hydrogen bonded internal waters on the basis of an  $\text{H}_2^{18}\text{O}$  induced downshift in frequency (Figure 4.10). In contrast, none of the retinal substitutions including the A2 retinal analog affects these bands (Figure 4.11). As expected, H-D exchange causes a complete disappearance of these bands (Figure 4.11, spectrum F) with their downshift and appearance in the O-D stretching region at (+)2682 and (-)2677  $\text{cm}^{-1}$  (Figure 4.12, spectrum F).

A similar spectral pattern is also observed in this region for *CrChR2*. The bands appear much broader and the negative band at 3617  $\text{cm}^{-1}$  at a lower frequency and positive band at 3602  $\text{cm}^{-1}$  at higher frequency relative to the corresponding bands in *CaChR1* (Figure

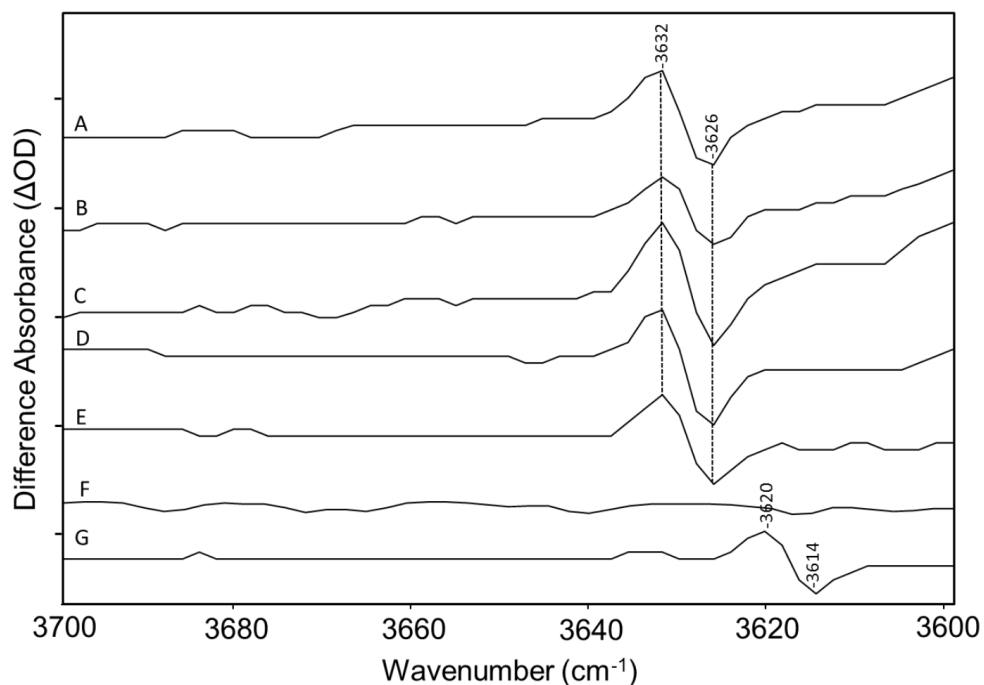


Figure 4.11: Spectra from Figure 4.4 over the 3600–3700  $\text{cm}^{-1}$  region. (A) native *CaChR1* and *CaChR1* regenerated with (B) A1 retinal, (C) A2 retinal, (D) [ $^{15}\text{-}^{13}\text{C},^{15}\text{-}^2\text{H}$ ] retinal, (E) [ $^{14},^{15}\text{-}^2\text{H}_2$ ] retinal, (F) *CaChR1* in  $\text{D}_2\text{O}$ , and (G) *CaChR1* in  $\text{H}_2^{18}\text{O}$ . Y-markers are approximately 0.15 mOD for all spectra.

4.10). The much broader bands in *CrChR2* indicate these waters are located in a more heterogeneous environment and have more disordered structure. Overall, the band pattern observed in both ChRs indicate that at least one weakly hydrogen bonded water undergoes a further decrease in hydrogen bonding strength during the primary phototransition. In contrast in BR it has been deduced that a weakly hydrogen bonded water (W401) which is part of a hydrogen-bonded pentagonal cluster located near the retinal Schiff base [95–97] undergoes an increase in hydrogen bonding. Furthermore, as discussed below, in contrast with BR, in *CaChR1* this water does not appear to be significantly affected by substitutions in the putative counterion residues near the SB.

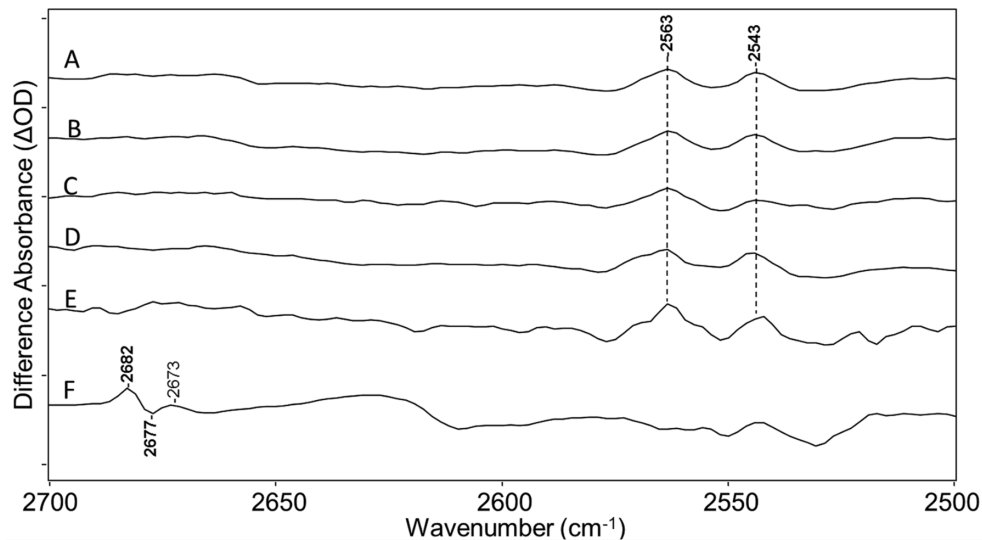


Figure 4.12: Spectra from Figure 4.4 over the 2500–2700  $\text{cm}^{-1}$  region. (A) native *CaChR1* and *CaChR1* regenerated with (B) A1 retinal, (C) A2 retinal, (D) [ $^{15}\text{C}$ , $^{2}\text{H}$ ] retinal, (E) [ $^{14}\text{C}$ , $^{2}\text{H}_2$ ] retinal, (F) *CaChR1* in  $\text{D}_2\text{O}$ , and (G) *CaChR1* in  $\text{H}_2^{18}\text{O}$ . Y-markers are approximately 0.25 mOD for all spectra.

#### 4.1.6 Detection of Cysteine Vibrations

The S–H stretching mode of cysteine residues is typically found in the spectral region from 2500–2600  $\text{cm}^{-1}$  [98,99]. For example, bands in this region have been assigned to cysteine in the FTIR difference spectrum of bovine rhodopsin [100], sensory rhodopsin from the fungus *Neurospora crassa* (NOP-1) [78], and sensory rhodopsin from *cyanobacterium Anabaena* (ASR) [64]. In contrast, bands do not appear in this region of BR and *NpSR*II, which have no cysteines in their primary sequences.

In the case of *CaChR1*, two positive bands appear in this region at 2563 and 2543  $\text{cm}^{-1}$  (Figure 4.12, spectrum A) which are highly reproducible in *CaChR1* regenerated with the various isotope substitutions and also in  $\text{H}_2^{18}\text{O}$  which are not expected to cause a shift in this vibration (Figure 4.12, spectra B-E). The higher frequency bands disappear as expected due to H–D exchange of the cysteine S–H group (Figure 4.12, spectrum F). However, the lower frequency band at 2543  $\text{cm}^{-1}$  could not be definitively assigned to cysteine since there is still positive intensity near 2543  $\text{cm}^{-1}$  in  $\text{D}_2\text{O}$ . Instead this band may arise from

positive/negative bands appearing in this region from the O–D stretch mode of internal D<sub>2</sub>O molecules. Alternatively, it is possible that this particular cysteine S–H group is inaccessible to H–D exchange as seen for example for some N–H peptide groups in BR [89].

#### 4.1.7 Effects of Mutations at Glu169 and Asp299 in the Carboxylic Acid C=O Stretch Region

Glu169 and Asp299 are the *CaChR1* residues homologous to the SB counterions Asp85 and Asp212 in BR, respectively. In order to identify possible contributions from Asp299, the conservative substitution Asp→Glu was made at position 299 to form the mutant D299E. This substitution, which adds an extra carbon in the side chain of Glu relative to the wild-type Asp, often shifts the frequency of the C=O stretch vibration in the carboxylic acid [91] but does not completely abolish it as in the case of Asn/Gln substitutions discussed below.

As seen in Figures 4.13 and 4.14, the band at 1703 cm<sup>-1</sup> downshifts to 1696 cm<sup>-1</sup> indicating its assignment to Asp299 (and the 1696 cm<sup>-1</sup> band to Glu299). Other changes in this region can also be attributed to this downshift and intensity cancellation of overlapping bands such as the decreased intensity of the negative band at 1686 cm<sup>-1</sup> and increased intensity of the negative band at 1710 cm<sup>-1</sup>. Note that only the positive band at 1703 cm<sup>-1</sup> appears to undergo a frequency shift due to this mutation, while other bands in this region remain unchanged. These results and earlier studies which demonstrate that Glu299 exists in an ionized state at neutral pH [32, 80] are consistent assignment of the positive 1703 cm<sup>-1</sup> band to protonation of Asp299 occurring during the *CaChR1* P<sub>0</sub>→P<sub>1</sub> phototransition.

Further support for this conclusion is based on measurements of D299E in D<sub>2</sub>O, where the 1698 cm<sup>-1</sup> band in WT (downshifted due to H–D exchange from 1703 cm<sup>-1</sup>) now appears due to the Asp→Glu substitution at an even lower frequency at 1692 cm<sup>-1</sup>. A strong negative band is also revealed in this mutant at 1700 cm<sup>-1</sup> which most likely is due to the H–D induced downshift of the band in D299E in H<sub>2</sub>O at 1710 cm<sup>-1</sup>. In WT with D<sub>2</sub>O this band may be masked by the more intense positive band at 1698 cm<sup>-1</sup> as

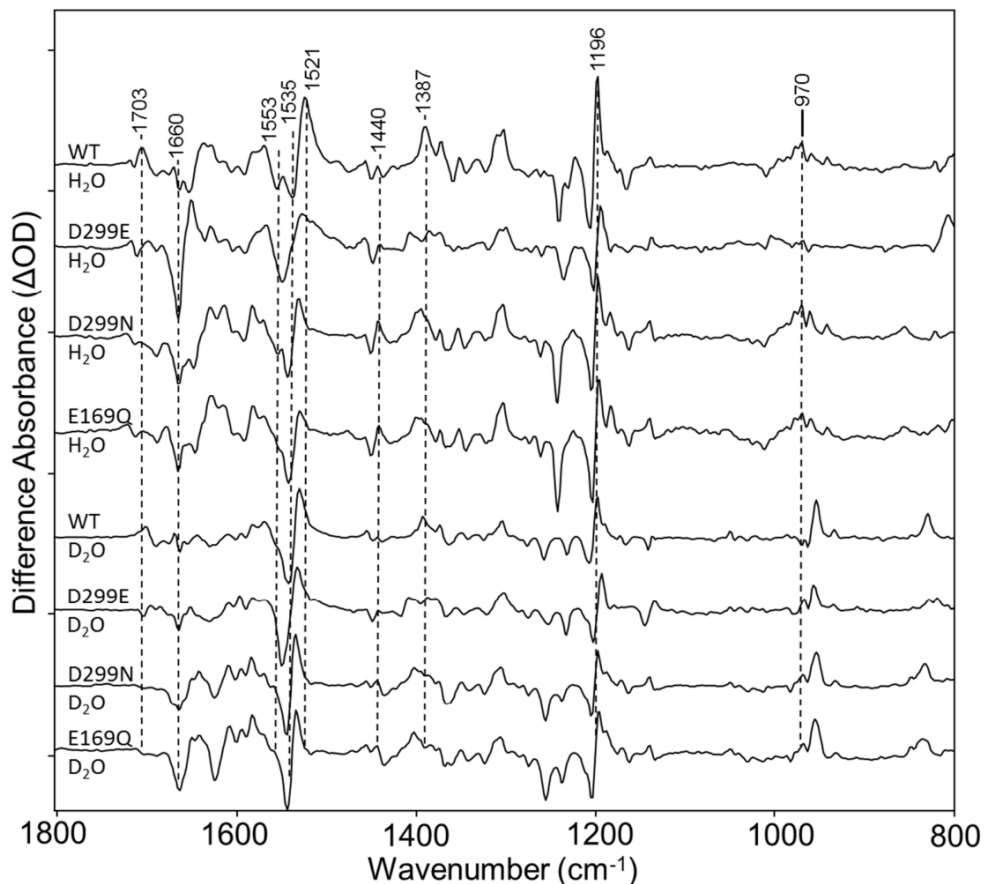


Figure 4.13: Comparison of *CaChR1* and the D299N, E169Q and D299E mutants over the region from 800-1800  $\text{cm}^{-1}$ . The top four spectra were recorded in  $\text{H}_2\text{O}$  and the bottom four in  $\text{D}_2\text{O}$ . All spectra were acquired as described previously. Y-axis markers are approximately 3 mOD for WT, 2 mOD for D299E, 2.5 mOD for D299N, and 1 mOD for E169Q

indicated by the presence of a shoulder near this frequency. Again, other than the 1698  $\text{cm}^{-1}$  band assignable to the deuterated Asp299 (COOD group), other bands do not appear to be affected by the Asp $\rightarrow$ Glu substitution. For example, the positive 1717  $\text{cm}^{-1}$  band which downshifts to 1707  $\text{cm}^{-1}$  due to H-D exchange can also be seen in D299E in  $\text{D}_2\text{O}$  at the same frequency.

Glu169 and Asp299 were also replaced with the neutral substitutions Gln and Asn, respectively to form E169Q and D299N. Previously, these mutants were studied in HEK293 cells using photoinduced charge displacement measurements [101] as well as RRS and UV-

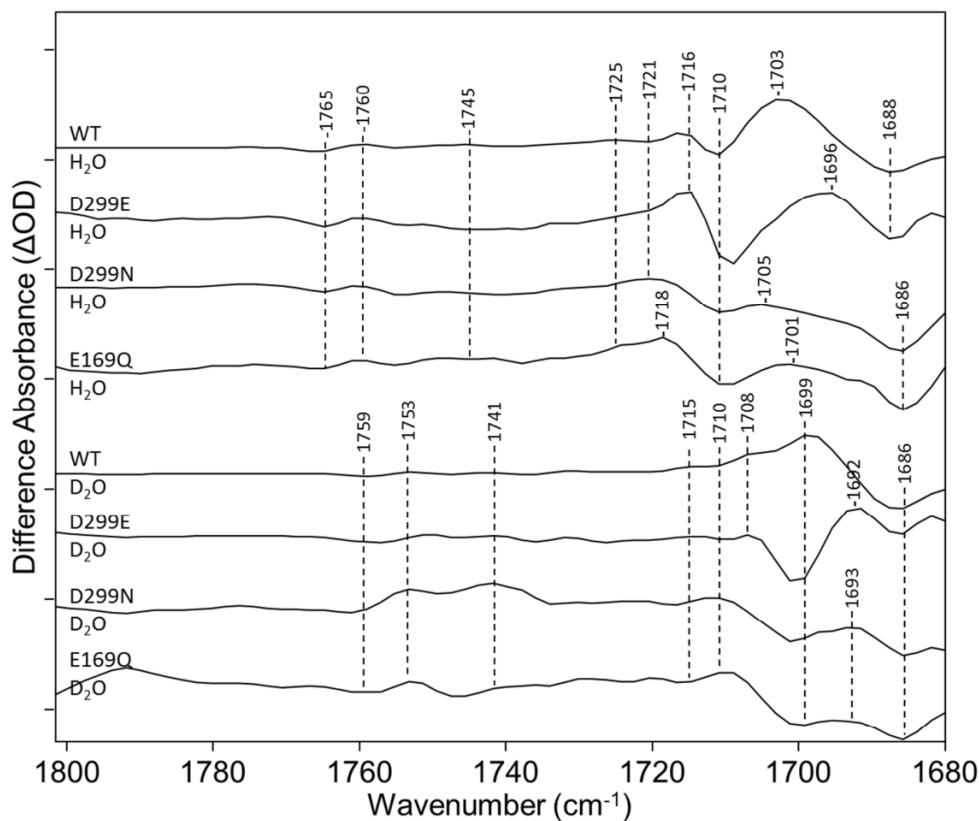


Figure 4.14: Comparison of *CaChR1* and the D299N, E169Q and D299E mutants over the region from 1680–1800  $\text{cm}^{-1}$ . The top four spectra were recorded in  $\text{H}_2\text{O}$  and the bottom four in  $\text{D}_2\text{O}$ . All spectra were acquired as described previously. Y-axis markers are approximately 1.5 mOD, 1 mOD, 0.2 mOD, 0.4 mOD, 1.5 mOD, 0.3 mOD, 0.2 mOD, and 0.5 mOD for spectra reading top to bottom.

visible absorption in detergent or reconstituted membranes as is discussed in earlier chapters of this thesis [32, 80]. Strikingly, both neutral mutations have almost identical effects on both chromophore and protein assigned bands in both  $\text{H}_2\text{O}$  and  $\text{D}_2\text{O}$  (Figure 4.13, spectra A-E). In the carboxylic acid C=O stretch region (Figure 4.14), the positive band at 1703  $\text{cm}^{-1}$  disappears. In addition, the negative band at 1710  $\text{cm}^{-1}$  and smaller positive band at 1717  $\text{cm}^{-1}$  are replaced by much broader positive/negative bands at 1718 and 1710  $\text{cm}^{-1}$ . The fact that the 1710  $\text{cm}^{-1}$  band does not undergo a significant change in intensity as occurs in D299E despite the disappearance of the nearby 1702  $\text{cm}^{-1}$  indicates that a more

intense negative band near this frequency also disappears. A similar pattern is also observed in D<sub>2</sub>O, where the positive band at 1698 cm<sup>-1</sup> disappears and a broad positive/negative bands appear at 1710 and 1700 cm<sup>-1</sup> downshifted approximately 9-10 cm<sup>-1</sup> from their position for these mutants in H<sub>2</sub>O. Importantly, no other bands in either H<sub>2</sub>O or D<sub>2</sub>O at higher frequency are affected by these mutations again supporting their assignment to other Asp or Glu residues in *CaChR1*. As described in below in more detail, the simplest model consistent with all the observed changes due to the three mutants studied, is a proton transfer occurring between Glu169 and Asp299 during the *CaChR1* P<sub>0</sub>→P<sub>1</sub>.

#### 4.1.8 Effects of Mutations at Glu169 and Asp299 in other Spectral Regions

The appearance of a positive ethylenic band in the region from 1520 to 1530 cm<sup>-1</sup> for all the mutants examined in both H<sub>2</sub>O and D<sub>2</sub>O provides strong evidence that these mutants produce a P<sub>1</sub>-like intermediate (Figure 4.13). In addition, the fingerprint region is highly characteristic of an all-*trans* to 13-*cis* isomerization for the primary transition, especially the appearance of the positive band near 1196 cm<sup>-1</sup>.

Interestingly, both of these neutral substitutions did not produce a downshift in the ethylenic frequency corresponding to an expected red-shift in visible absorption wavelength which would be expected if the putative counterion to the positively charged SB were neutralized as is observed in the case of BR [63]. Instead, a small blue-shift can be deduced from the increase in frequency of the ethylenic mode (Figure 4.13). A similar effect was also observed in the RRS of these mutants [80], as is described in the previous chapter, as well as directly from visible absorption measurements [32]. As discussed recently, this absence of a red-shift is most likely a consequence of a neutral residue (Phe139) on helix B; in the case of most high-efficiency ChRs that do exhibit red-shifts, they have a positively charged Lys as the homologue [32]. The largest upshift in frequency of the negative ethylenic band occurs for D299E (Figure 4.13) with a  $\nu_{C=C}$  near 1547 cm<sup>-1</sup>, which agrees with a blue-shifted  $\lambda_{\max}$  near 505 nm and also with RRS measurements [80]. A small negative band at 1182 cm<sup>-1</sup> (Figure 4.13) is also observed, indicative of increased 13-*cis* isomer content in this mutant.



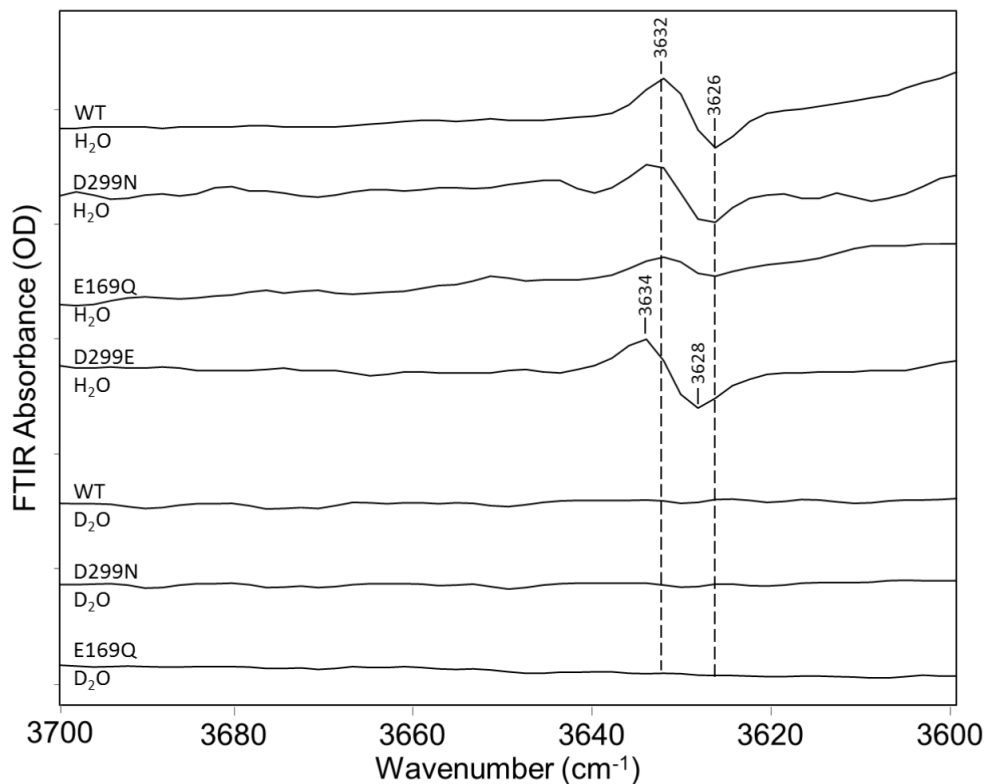


Figure 4.15: Comparison of CaChR1 WT and mutants over the 3600-3700  $\text{cm}^{-1}$  region. The top four spectra were recorded in  $\text{H}_2\text{O}$  and the bottom three in  $\text{D}_2\text{O}$ . Y-axis markers are approximately 0.2 mOD for all spectra.

The negative band at 1553  $\text{cm}^{-1}$  assigned to the amide II mode (see above) is also reduced or eliminated with the Asn and Gln substitutions. In the case of the D299E mutant the band may still be present but is hidden by the upshift of the ethylenic band. In the case of the 1600-1700  $\text{cm}^{-1}$  region, the small negative band at 1660  $\text{cm}^{-1}$  in WT, most likely assigned to the amide I mode, dramatically intensifies along with a positive band near 1648  $\text{cm}^{-1}$ .

Interestingly, the bands assigned to weakly hydrogen bonded water molecules appear not to be significantly altered by these mutations as most clearly seen in the region of the O-H stretch (Figure 4.15). There is, however, a small upshift of 1-2  $\text{cm}^{-1}$  in the frequency of these bands in the case of D299E. This indicates that the weakly hydrogen bonded waters do not strongly interact with Glu169 or Asp299.

## 4.2 Conclusions from Low-Temperature FTIR Studies of *CaChR1*

In order to further investigate the molecular mechanism of ChR light activation, we have focused in this work on the structural changes that occur during the primary phototransition from the dark state,  $P_0$  to the red-shifted  $P_1$  intermediate of *CaChR1* which is analogous to the well-known BR to K transition in the BR photocycle. Part of the motivation for this study are the near-IR confocal RRS measurements described in the previous chapter which shed light on the ground state chromophore composition of *CaChR1* and showed that is significantly different compared to *CrChR2* which consists of a mixture of all-*trans* and 13-*cis* isomers [28]. In contrast, *CaChR1* resembles the pure all-*trans* retinal composition of many microbial rhodopsins such as BR and *NpSR11* [80]. In addition, measurements of intramolecular proton transfers indicate that *CaChR1* exhibits a fast outward directed photoinduced current with a rise time similar to M formation in BR, while other ChRs such as *CrChR2* do not exhibit this current [101]. Furthermore, recent time-resolved measurements of the *CaChR1* photocycle (see Appendix A ) indicate that the decay time for the  $P_1$  intermediate is significantly longer than in *CrChR2* [102]. Hence, it is important to further elucidate the differences in the light-activated ion gating mechanisms between *CaChR1* and *CrChR2* and a variety of other ChRs derived from green flagellate algae.

As described in the previous chapter, the FTIR-difference measurements reported here on the primary phototransition of *CaChR1* and *CrChR2* were made at 80 K on protein reconstituted into bilayer lipid membranes. A number of methods were used to assign peaks in the spectra including retinal isotope labeling, site-directed mutagenesis and measurements of the effects of  $D_2O$  and  $H_2^{18}O$  substitutions on band frequency. Although no earlier FTIR-difference measurements have been reported for the primary phototransition of *CaChR1* , recent static FTIR-difference measurements were reported for *CaChR1* at room temperature, which reflect mainly the *CaChR1*  $\rightarrow P_2$  transition [45]. In addition, low-temperature FTIR-difference measurements have been reported for the primary phototransition of *CrChR2* [46, 67] and C1C2, the chimera of *CrChR1* and *CrChR2* (see

below) [72].

The picture that emerges from the present study further supports the conclusion based on RRS [80] that the unphotolyzed retinal composition of *CaChR1* and *CrChR2* are significantly different with *CaChR1* containing an almost pure all-*trans* retinal composition which photoisomerizes to a 13-*cis* configuration. In contrast, *CrChR2* contains a mixed retinal composition with both species undergoing isomerization during the primary phototransition. Furthermore, the FTIR difference spectra reveal fundamental differences between the structural changes during the primary phototransition of these two ChRs from *Chlamydomonas* involving the retinylidene chromophore, peptide backbone, Asp/Glu residues, cysteine residues and internal water molecules as summarized below:

#### **4.2.1 Chromophore Structural Changes in the primary phototransition of *CaChR1* are more similar to BR than to *CrChR2***

The FTIR-difference spectrum of *CaChR1* is very similar to that measured in BR (Figure 4.1), particularly in the fingerprint region, where earlier RRS and FTIR- difference measurements show all-*trans* retinal isomerizes to a 13-*cis* , 15-*anti* configuration. Furthermore, at 80 K the transition to the P<sub>1</sub> state of *CaChR1* is photo-reversible, similar to BR and many other microbial rhodopsins.

In contrast, parallel photoreactions of both an all-*trans* and 13-*cis* retinal isomer appear to occur in the primary phototransition of *CrChR2* . In addition, this reaction is not fully photo-reversible (see for example Figure 4.3). This last feature is understandable if the P<sub>1</sub> photoproducts of the all-*trans* and 13-*cis* species of *CrChR2* have different absorption properties and are thus not fully reversed to the same composition of retinal isomers as the original retinal species. In this regard, femtosecond time-resolved absorption measurements on *CrChR2* reveals different P<sub>1</sub>-like intermediates in equilibrium after excitation for the first few picoseconds [103] which might reflect multiple species of the ground state composition.

#### 4.2.2 Structural changes which involve the protein backbone are different in *CaChR1*, *CrChR2*, and BR

The appearance during the primary phototransition of a negative band near  $1553\text{ cm}^{-1}$  assigned to the amide II mode of *CaChR1* along with appearance of peaks assigned to amide I modes in the  $1600\text{--}1700\text{ cm}^{-1}$  region provides strong evidence that *CaChR1* undergoes structural changes of the protein backbone as early as the primary phototransition. Similarly, the primary phototransition of *CrChR2* also involves significant but different protein backbone structural changes as indicated by the appearance of an intense negative band at  $1664\text{ cm}^{-1}$  which is not present in the difference spectrum of *CaChR1* (see Figures 4.1, 4.3 and ref [46]). Note, however, that a similar band appear near  $1661\text{ cm}^{-1}$  in subsequent steps in the photocycle of *CaChR1* (ref [29]). There are also differences in other bands in the amide I region such as the appearance of a negative band at  $1687\text{ cm}^{-1}$  in *CaChR1* but not *CrChR2*. Overall, the appearance of amide I and amide II bands in the 80 K spectrum of *CaChR1* compared to the absence of such contributions in BR (see Figure 4.1) indicates that retinal isomerization produces significantly more protein structural change in both this protein as well as *CrChR2*.

#### 4.2.3 Structural changes of weakly hydrogen bonded internal water molecules are different in *CaChR1* and *CrChR2*

FTIR-difference bands due to structural changes of internal water molecules have not previously been identified for either *CaChR1* or *CrChR2*, although they have been observed in the FTIR-difference spectrum during the primary phototransition of a chimera of *CaChR1* and *CrChR2* [5] as well as many other microbial including BR and archaerhodopsin-3 (AR3) [82].

As discussed in the above section, a comparison of the bands appearing in the O–H stretching region for weakly hydrogen bonded water molecules (sometimes referred to as water molecules with dangling O–H groups) reveals distinct differences between *CaChR1*, *CrChR2*, and BR (see Figure 4.10 and ref [82]). This provides clear evidence that distinct differences occur in the environment and/or structural changes which these waters undergo

during the primary phototransition. Most notably there appears much broader bands in *CrChR2* than *CaChR1*. The broader bands in *CrChR2* indicate multiple sub-conformational states of the protein at least at 80 K consistent with conclusions discussed above regarding the retinal configuration of *CrChR2*.

Bands in the region of weakly hydrogen bonded D<sub>2</sub>O from 2650-2700 cm<sup>-1</sup> (O–D stretch mode) have also been identified in the C1C2 chimera [72] (whose 3D structure has been solved at 2.3 Å resolution [5]). Particularly striking is the agreement of these bands in C1C2 and the spectra shown in Figure 4.12 for *CrChR2* (but not *CaChR1*) indicating that the waters giving rise to these bands must exist in very similar environments and undergo similar changes. Since the first 5 TM helices in C1C2 are derived from *CrChR1* and last two from *CrChR2*, the waters in both proteins giving rise to these bands are likely to be interacting with residues in the last two helices. One possibility is that this reflects a water molecule that bridges Asp292 and Lys 132 (*CrChR1* numbering) as predicted previously [72]. In contrast, this water is not expected to be present in *CaChR1* since Lys132 is replaced by Phe139 (*CaChR1* numbering) which, due to its hydrophobic properties, is not likely to interact with a water molecule.

#### 4.2.4 Asp299 protonates during the primary phototransition

An important goal of this study is to understand the role of the two residues Glu169 and Asp299 in *CaChR1* which are homologous to Asp85 and Asp212 in BR. In the case of BR these two residues exist in an ionized form in both the BR light and dark-adapted state and together serve along with a water molecule (W402) as a complex counterion to the Schiff base [6]. Both residues also exist in an ionized form in the K intermediate since no bands are assignable to these residues in the carboxylic acid region of the low-temperature BR→K FTIR-difference spectrum [80]. Instead, a protonated form of Asp115 (BR numbering) located near the β-ionone ring of BR [6] is perturbed giving rise to negative/positive bands at (-)1741 and (+)1736 cm<sup>-1</sup> (see Figure 4.1) [80].

#### 4.2.5 Interactions of Glu169 and Asp299: a Model for Early Photocycle Proton Transfer

A key question is whether Glu169 and Asp299 change their protonation state during the primary phototransition in *CaChR1*. This would not be unreasonable since other protein structural changes are observed (see above) that appear to be much larger than what occurs in BR. In this regard, it was concluded on the basis of visible absorption and RRS pH titrations that unlike Asp85 in BR, at neutral pH the homologous residue Glu169 is protonated (neutral). In contrast, Asp299 exists in an ionized form similar to its homologue Asp212 in BR. Thus, unlike BR, where both homologous residues are ionized in the ground state and K intermediate, and thus cannot contribute to the BR→K difference spectrum, it is possible that both residues could contribute to the *CaChR1* P<sub>0</sub>→P<sub>1</sub> difference spectrum. In particular, protonation of Asp299 would be expected to produce a positive band in the carboxylic acid region, whereas deprotonation of Glu169 would produce a negative band in this region. Alternatively, a perturbation of the hydrogen bonding of the protonated Glu169 would result in negative/positive bands in this region.

As described above, a positive band at 1703 cm<sup>-1</sup> was identified and assigned to the protonation of Asp299 on the basis of a downshift of this band in the mutant D299E and abolishment of this band in the mutant D299N. Thus we conclude that during the *CaChR1* P<sub>0</sub>→P<sub>1</sub> transition, this group accepts a proton from an as yet unidentified donor group.

A possible identity of the proton donor to Asp299 is also indicated from the results presented here, but not definitely established without further examination of mutants. This model, which is shown in Figure 4.16, envisions a proton transfer during the first step of the photocycle from Glu169 to Asp299. The basis for this model is the appearance of an increased negative band at 1710 cm<sup>-1</sup> in the mutant D299E due to the downshift of the 1703 cm<sup>-1</sup> band assigned to Asp299 along with a similar band at a 1700 cm<sup>-1</sup> in the case of D299E in D<sub>2</sub>O. In contrast, despite the disappearance of the positive band assigned to D299E in the mutants E169Q and D299N, an increase in intensity of a negative band at 1710 cm<sup>-1</sup> (1700 cm<sup>-1</sup> for the case of these mutants in D<sub>2</sub>O) does not occur. This is consistent

with at least part of the intensity of the negative band at  $1710\text{ cm}^{-1}$  originating from the deprotonation of Glu169.

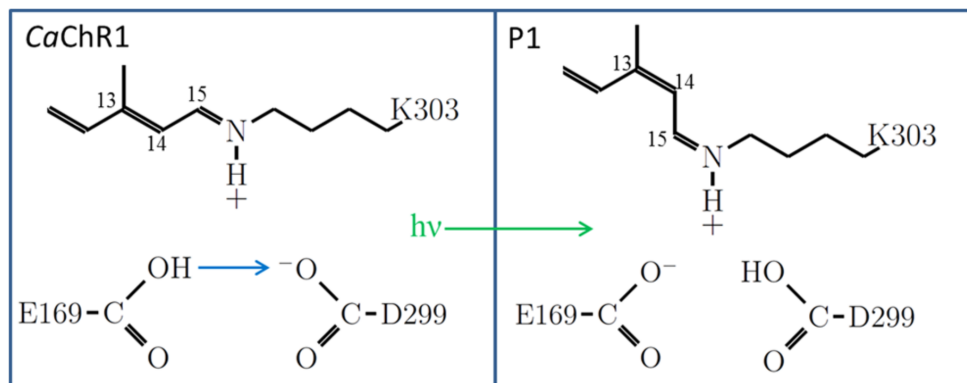


Figure 4.16: Schematic model showing Glu169 and Asp299 residues that interact with each other through a hydrogen bond formed by the carboxylic acid group of Glu169 and carboxylate group of Asp299. These residues together function as a counterion for the positively charged SB present in the unphotolyzed,  $P_0$  state of *CaChR1*. During the initial step in the *CaChR1* photocycle ( $P_0 \rightarrow P_1$ ) triggered by light absorption, an all-*trans* to 13-*cis* isomerization of the retinylidene chromophore occurs and a proton is transferred from Glu169 to Asp299.

The disappearance of both bands (positive  $1703\text{ cm}^{-1}$  and negative  $1710\text{ cm}^{-1}$ ) in the E169Q and D299N mutants is understandable on the basis of this model since the postulated proton transfer would be expected to be prevented between Glu169 and Asp299, thus abolishing all bands associated with transfer. In contrast proton transfer could still occur in D299E, where Glu299 can still function as a proton acceptor and Glu169 as a donor, thus preserving the bands (albeit with a downshifted band assigned to Glu299). It is also noted that Glu169 is predicted to exist in an ionized form in the D299N mutant [32,80] thus bands due to protonated Glu169 are not expected to contribute to the difference spectrum in this region.

The model also explains the nearly identical effects of the E169Q and D299N mutants on the FTIR-difference spectrum. In the carboxylic acid region, both mutants abolish the same bands associated with the postulated Glu169 to Asp299 difference spectrum since they

both prevent proton transfer. Furthermore, the more delocalized effects that occur due to this blocked proton transfer on chromophore and protein structural changes are expected to be similar.

Additional support for this model comes from the x-ray crystallographic structure of C1C2, which shows Glu169 and Asp299 are in a position to form an ionic interaction [5]. Such a strong interaction of a carboxylate group (ionized E169) with a carboxylic acid (protonated D299) would account for the relatively low frequency of the  $1703\text{ cm}^{-1}$  band assigned to Asp299 in the  $P_1$  state and Glu169 ( $1710\text{ cm}^{-1}$ ) in the ground state as previously shown for carboxylate groups which act as H-bond donor [104]. Importantly the overall proton transfer from Glu169 to Asp299 would also preserve charge neutrality of the active site which includes the protonated SB. In particular, the negative charge transfers from one residue (Asp299) to another (Glu169), both of which are located close to the Schiff base. It is possible that a small displacement of the positive charge due to all-*trans* to 13-*cis* isomerization of the chromophore could trigger such a redistribution of charge.

Interestingly, this model is supported by photoinduced channel currents measured for *CaChR1* and its mutants expressed in HEK293 cells [101]. For example, current generation measured during formation of the  $P_2$  intermediate is accelerated in the D299N mutant and slowed down significantly in the E169Q mutant. The interpretation of this data is that Glu169 serves as the primary acceptor group for the SB proton and Asp299 can act as an alternate acceptor [101] albeit much less efficiently. This model would then necessitate that Glu169 deprotonates prior to formation of  $P_2$ . In particular, since Glu169 is predicted to be protonated in the dark state of *CaChR1*, its deprotonation at  $P_1$  would allow it to act as a proton acceptor during  $P_2$  formation.

We also note that a critical feature which has been proposed to explain the difference between *CaChR1* and *CrChR2* is the existence of the neutral residue Phe132 in *CaChR1* (*CaChR1* numbering) which is replaced by the positively charged residue Lys132 in *CrChR2* (*CaChR1* numbering) [32]. Importantly, this residue is in a position to modulate the  $\text{pK}_a$  of Glu169 which, as discussed above, is predicted to be protonated at neutral pH in *CaChR1*.



The presence of a positively charged lysine at this position in *CrChR2* could lower the  $pK_a$  so that this group will exist in an ionized state in the unphotolyzed ground state of this protein, thereby altering the active site and subsequent protein conformational changes observed even during the primary phototransition as deduced in this work.

## Chapter 5

### The $P_0 \rightarrow P_2$ phototransition: a Model for Proton Transfer into the Conduction State of *CaChR1*.

#### 5.1 FTIR Difference Spectroscopy of the *CaChR1* $P_0 \rightarrow P_2^{380}$ phototransition

In order to measure the FTIR differences for the transition from the unphotolyzed *CaChR1*  $P_0$  state to the  $P_2^{380}$  intermediate, fully hydrated films of protein reconstituted in lipids (ECPL) were recorded at 270 K using static FTIR difference spectroscopy as described in the Methods Chapter. In addition, time-resolved Rapid Scan FTIR differences were also measured at 5 and 20 °C using a 532 nm Nd:YAG laser flash excitation, as described in the Methods Chapter. As seen in Figure 5.1 both static and time-resolved methods resulted in very similar difference spectra. For example, the rapid scan difference spectra averaged over the first 45 ms after the laser flash excitation at both 5 and 20 °C (278 and 293 K) are very similar to the static spectra obtained at -3 °C (270 K). A similar agreement was obtained by analyzing the rapid scan data using singular value decomposition (SVD) methods (see below and Figure 5.2). Although not identical, these spectra are also similar to recently reported FTIR difference spectra recorded at RT of *CaChR1* in detergent micelles [27, 29].

An SVD analysis of the rapid scan, time resolved data recorded at 293 K (20 °C) shown in Figure 5.1 results in a first (largest amplitude) basis spectrum that is in excellent agreement with the static FTIR-difference spectrum recorded at 270 K as shown in Figure 5.2. Note that the second largest basis spectrum, in each case, was ten times smaller than the primary spectrum. In addition, the time dependence associated with this first basis spectrum from the SVD analysis of both the 5 and 20 °C data are shown in the Figure 5.2 inset and are well fit by single exponential decays with time constants of approximately 65 ms and 170 ms, respectively. Importantly, these time constants correspond well with  $P_2^{380}$  decay time-constants measured at the same temperatures by time-resolved flash-laser visible absorption of suspensions of the *CaChR1* membranes used to form the FTIR films (Figure 5.4) [24]. The global fit difference spectrum determined from SVD analysis also agrees well

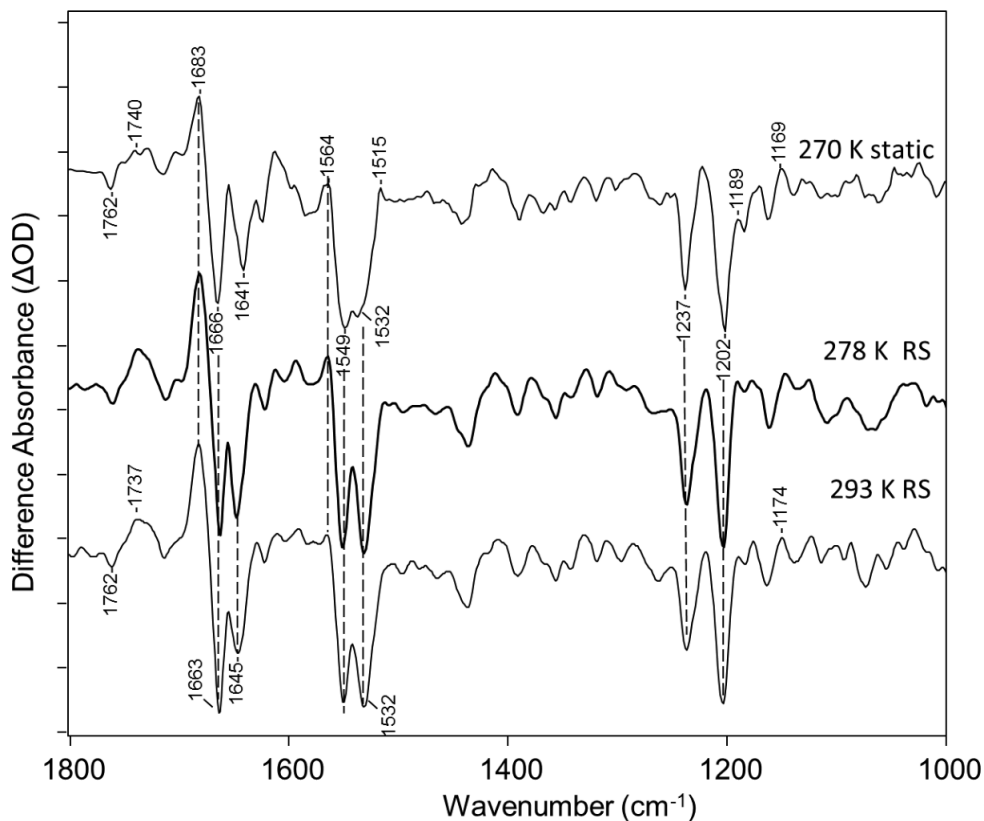


Figure 5.1: Comparison of FTIR-difference spectra of *CaChR1* for static recorded at 270 K and rapid scan recorded at both 278 and 293 K over the 1000–1800  $\text{cm}^{-1}$  region. Y-axis markers indicate 0.2 mOD for *CaChR1* static spectra and 0.2 mOD, 0.2 mOD, and 0.1 mOD for *CaChR1* 270 K static, 278 K RS, and 293 K RS spectra, respectively.

with the static measurements (Figure 5.2). These results strongly indicate that *CaChR1* decays almost exclusively back to the ground state from  $P_2^{380}$  under these low-temperature conditions.

The static difference spectrum shown in Figure 5.1 reflects the difference between 1 minute data acquisition before and 1 minute during photo-steady illumination with 505 nm light (steps 2-1 in standard steady state illumination conditions as described in the Materials and Methods chapter). Similar results were also obtained for the 3-1 difference reflecting changes occurring before and 1 minute after the 505 nm light is turned off (Figure 5.3. The smaller amplitude of the 3-1 vs. 2-1 differences reflects the thermal decay of *CaChR1* back

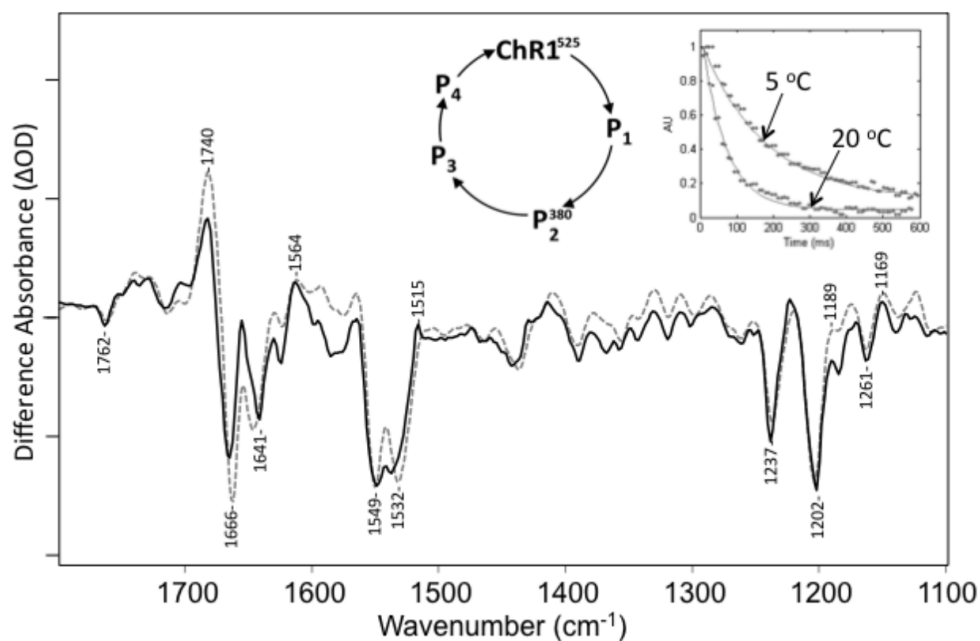


Figure 5.2: Comparison of time-resolved rapid scan FTIR-difference basis spectrum produced by SVD analysis (dashed) recorded at 20 °C and static FTIR-difference spectrum (solid) recorded at 270 K. Right Inset: SVD derived decays for time-resolved FTIR-difference spectra at 5 °C and 20 °C. Y-axis markers are approximately 0.8 mOD for both time-resolved and static difference spectra. A photocycle scheme is also shown which is typical for ChRs.

to the unphotolyzed  $P_0$  state. As expected, the subsequent 4-3 difference spectrum (shown inverted for clarity) matches well the 3-1 difference spectrum indicating that the residual photoproducts formed after one minute of thermal decay are fully photoreversed back to the dark state using 1 minute of 405 nm illumination, in agreement with the standard steady state procedure. Note that both these results support the conclusion (see below) that the transition from unphotolyzed state to  $P_2^{380}$  is reflected in the difference spectra shown in Figure 5.1.

The formation of the  $P_2^{380}$  intermediate and the absence of significant contributions from other photointermediate under these conditions can also be deduced from the absence of positive bands in the fingerprint region between 1180 and 1195  $\text{cm}^{-1}$  (Figure 5.1). Normally,

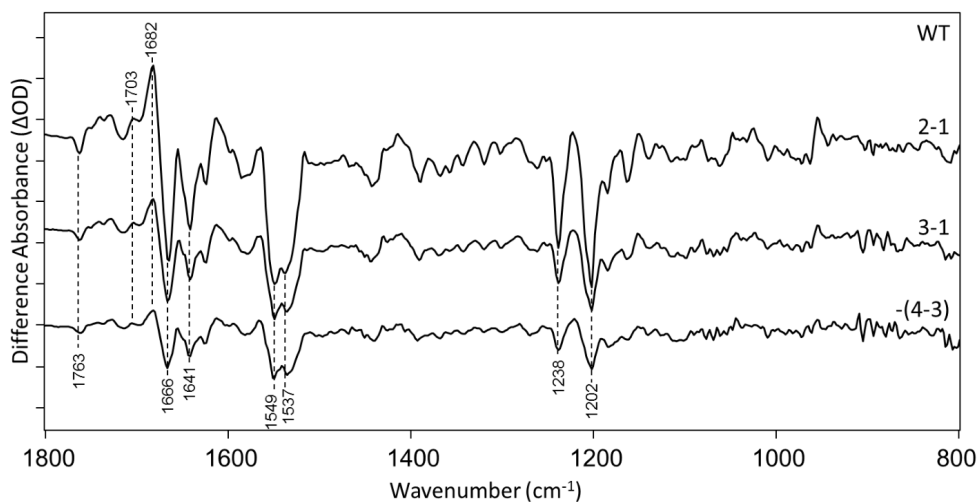


Figure 5.3: FTIR-difference spectra in the 800–1800  $\text{cm}^{-1}$  region of *CaChR1* recorded using the photoreversal methods at 270 K. Y-axis markers are approximately 0.2 mOD for all spectra

such positive bands appear due to formation of a species with a 13-*cis* retinal chromophore and protonated SB. For example, a strong positive band appears in the *CaChR1*  $P_0 \rightarrow P_1$  FTIR- difference spectrum measured at 80 K at 1196  $\text{cm}^{-1}$  [105] (see previous chapter). In contrast, the absence of positive bands in this region is characteristic of a photointermediate with a deprotonated retinylidene SB such as seen for the  $BR \rightarrow M_{412}$  transition, where the SB of  $M_{412}$  is deprotonated [106]. Since  $P_2^{380}$  is the only intermediate expected to have a deprotonated SB in the *CaChR1* photocycle, significant contributions from other intermediate are unlikely.

A positive band also appears at 1564  $\text{cm}^{-1}$  close to the expected frequency of the ethylenic stretch of the  $P_2^{380}$  measured by resonance Raman spectroscopy (RRS) [29]. Since no other strong positive band appears in this region, this further supports the conclusion that the  $P_2^{380}$  intermediate is the major contributor to the FTIR-difference spectra recorded under these conditions (Figure 5.1).

A corresponding negative band also appears in the ethylenic stretching region at 1532  $\text{cm}^{-1}$  which has previously been assigned by RRS to the unphotolyzed state of *CaChR1*

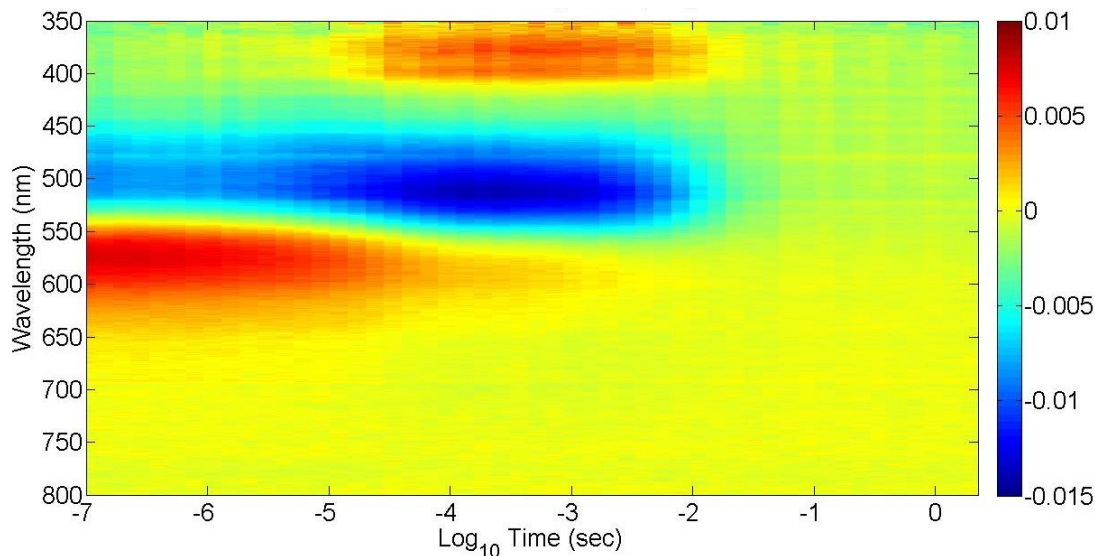


Figure 5.4: Laser Induced Transient Absorbance Spectroscopy of *CaChR1* solution in ECPL at 25 °C. Difference absorbance is shown by the color bar to the right of the plot. Buildup of  $P_1$  is seen at early timescales as well as depletion of  $P_0$ . Decay of  $P_1$  into  $P_2$  occurs nearly completely by  $10^{-4}$  s followed by a reset of the  $P_0$  state by 100 ms.

[29, 80]. Interestingly, a second prominent negative band appears at  $1549\text{ cm}^{-1}$  which is also seen as in the *CaChR1*  $P_0 \rightarrow P_1$  FTIR-difference spectrum [105]. While this band has been associated with a proposed blue-shifted intermediate present in the dark state of *CaChR1* [29], in the case of the *CaChR1*  $P_0 \rightarrow P_1$  difference spectrum it has been assigned to the amide II vibration on the basis of its insensitivity to isotope labeling and substitution of the analog A2 retinal (3,4-dehydroretinal) [105]. A similar insensitivity of this band is also observed for the *CaChR1*  $P_0 \rightarrow P_2^{380}$  FTIR-difference spectrum recorded at 230 K [107]. Strong bands are also observed in the amide I regions at  $1666\text{ cm}^{-1}$  (negative) and  $1683\text{ cm}^{-1}$  (positive) which, along with the amide II band, indicate significant structural changes of the protein backbone which occurs in the formation of  $P_2^{380}$ .

### 5.1.1 Band Assignments in the Carboxylic Acid C=O Stretch Region

The  $1700\text{-}1800\text{ cm}^{-1}$  region reflects alterations mainly in Asp/Glu residues which can undergo changes in hydrogen bonding or protonation state. Several bands appear in this

region as shown in Figure 5.5. Most prominently, a negative band is located at  $1763\text{ cm}^{-1}$  and positive bands at  $1770$ ,  $1753$ ,  $1741$ ,  $1729$  and  $1704\text{ cm}^{-1}$ . A broad negative band also appears near  $1715\text{ cm}^{-1}$  that resolves into two negative bands at  $1720$  and  $1713\text{ cm}^{-1}$  in the Fourier self-deconvolution (FSD) difference spectrum (dashed line, Figure 5.5).

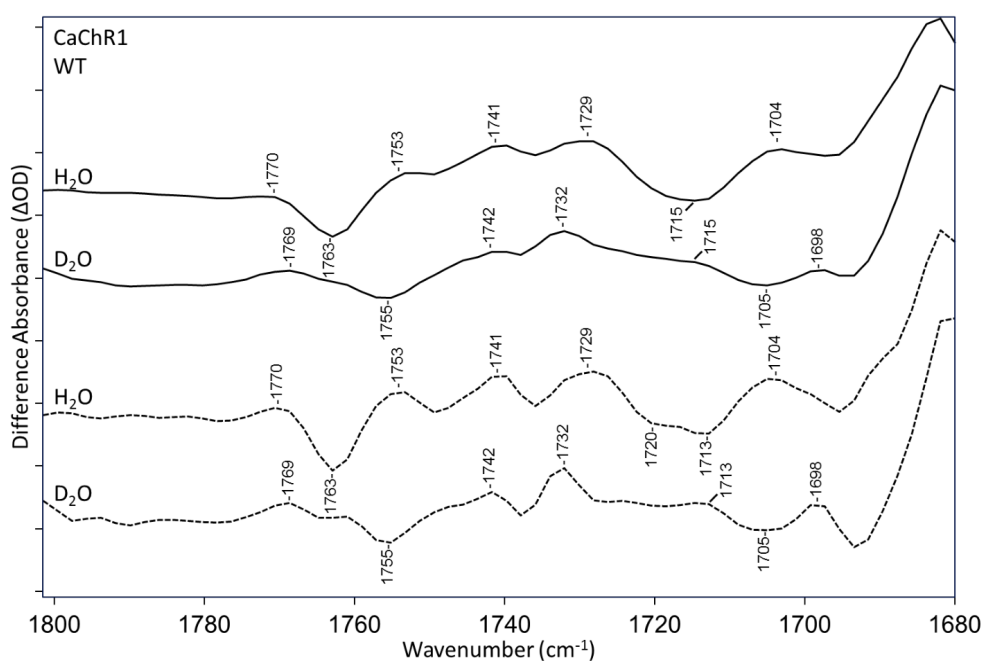


Figure 5.5: FTIR-difference spectra of *CaChR1* WT recorded at 270 K over the  $1680\text{--}1800\text{ cm}^{-1}$  region in both  $\text{H}_2\text{O}$  (first and third spectra) and  $\text{D}_2\text{O}$  (second and fourth spectra). Spectra were acquired using static methods and differences show are the average of 2-1 in the photoreversal cycle. Dashed plots show FSD processed spectra. Y-axis markers are approximately 0.1 mOD and 0.05 mOD for  $\text{H}_2\text{O}$  and  $\text{D}_2\text{O}$  spectra, respectively.

Depending on the strength of the hydrogen bonding, bands due to the C=O stretch of carboxylic acids downshift  $5\text{--}12\text{ cm}^{-1}$  due to H–D exchange, as shown in previous chapters [92]. As seen in Figure 5.5, all of the difference bands identified in this region for *CaChR1* in  $\text{H}_2\text{O}$ , undergo a downshift to a corresponding band in  $\text{D}_2\text{O}$ , although not by the same amount. For example, the negative  $1763\text{ cm}^{-1}$  band downshifts approximately  $8\text{ cm}^{-1}$ , whereas the  $1753$  and  $1741\text{ cm}^{-1}$  bands downshift  $12$  and  $9\text{ cm}^{-1}$ , respectively.

In order to assign bands in this region, the effects of substitutions of the residue Glu169,

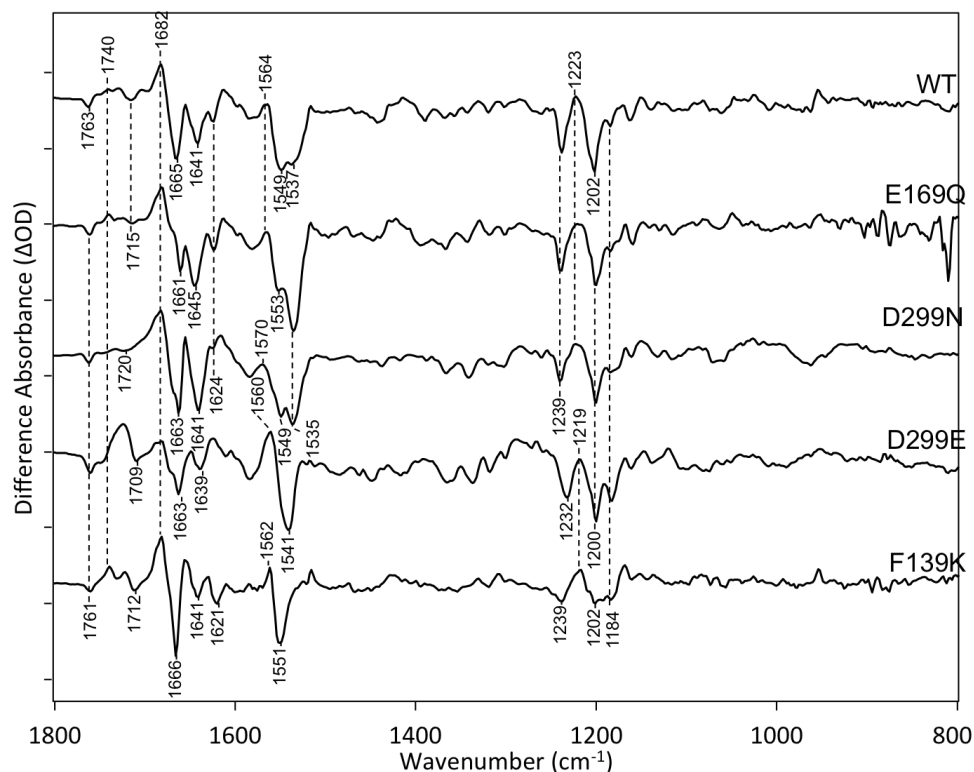


Figure 5.6: FTIR-difference spectra in the 800-1800  $\text{cm}^{-1}$  region of *CaChR1* and mutants recorded at 270 K. The y-axis tick marks are approximately 0.5, 0.3, 0.8, 0.7, and 0.5 mOD for the spectra from top to bottom.

Asp299 and Phe139 (Positions shown in Figure 5.7) were measured at 270 K (Figure 5.6). All of these mutants appear to form predominantly  $\text{P}_2^{380}$  based on the appearance of the 1564  $\text{cm}^{-1}$  band assigned to the ethylenic mode of  $\text{P}_2^{380}$ . All of these mutations also have similar band structures in the fingerprint region which as discussed above reflects an all-*trans* to 13-*cis* isomerization. Two exceptions however are the mutants F139K and D299E. In these cases, the appearance of a more negative band relative to WT appears near 1184  $\text{cm}^{-1}$ , indicative of the co-existence of a 13-*cis* retinal configuration in the unphotolyzed state (Figure 5.6) [80]. These 13-*cis* containing states are likely to also produce photocycle intermediates, although the photoproducts may exhibit weak positive bands if associated with a deprotonated SB species similar to  $\text{P}_2^{380}$  as noted above. Resonance Raman spectra also shows such a band in the dark state of F139K and D299E relative to WT. Interestingly,



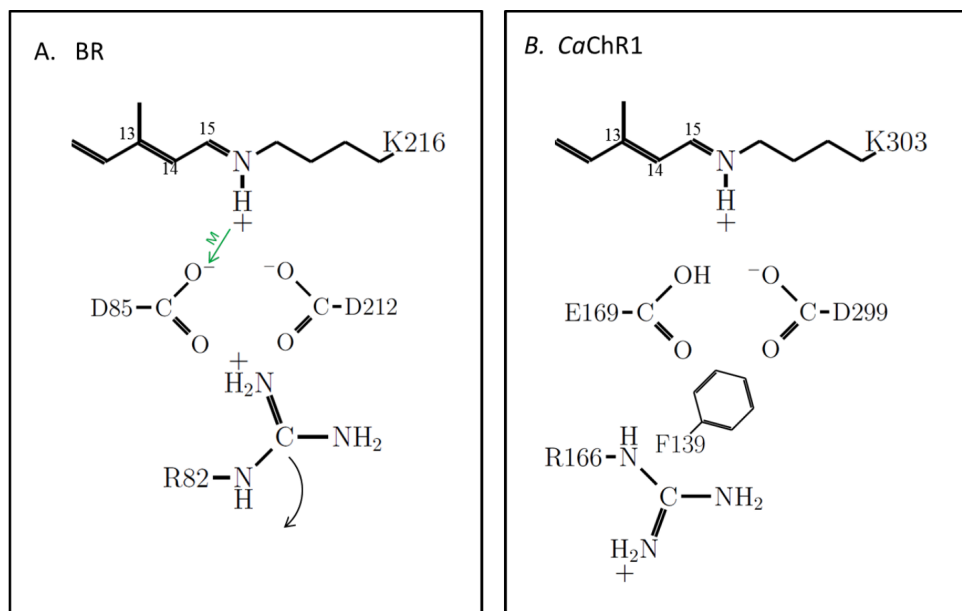


Figure 5.7: Schematic showing key residues and their ionization states in the photoactive site of light-adapted BR and *CaChR1*. A. BR: The positioning of residues is guided by known high resolution x-ray structure [108]. Green arrow indicates role of Asp85 as SB proton acceptor during  $M_{412}$  formation [91]. Curved arrow indicates repositioning of R82 towards extracellular side of membrane that triggers proton release by proton release group. B. *CaChR1*: The positioning of the residues is guided by the high resolution x-ray structure of the C1C2 chimera [79]. Ionization states are inferred from recent pH titrations on various *CaChR1* mutants [32, 101]. F139 is replaced by a positively charged lysine in most high-efficiency ChRs [32]

as discussed below, this mixed retinal composition is similar to what is observed in *CrChR2* [80] and may be a consequence in the case of F139K of ionization of Glu169 which can interact with the nearby Lys residue instead a neutral phenylalanine [28, 80].

All of these mutants also display an increase in frequency of the negative band assigned to the ethylenic C=C stretch vibrations near  $1532\text{ cm}^{-1}$  (see above) consistent with their blue-shifted visible absorption  $\lambda_{\text{max}}$  [32]. This effect agrees with the observed inverse linear correlation between  $\nu_{C=C}$  and  $\lambda_{\text{max}}$  for other rhodopsins [77–79] and as observed previously and shown in the Raman chapter of this thesis with measurements of the E169Q and D299N

mutants of *CaChR1* [80]. The most dramatic example of this effect is the upshift of this band to around  $1551\text{ cm}^{-1}$  in F139K and  $1541\text{ cm}^{-1}$  in D299E (Figure 5.6) consistent with the upshifted ethylenic frequency measured by RRS [80]. Note that these upshifts most likely hide the second negative band at  $1549\text{ cm}^{-1}$  assigned to the amide II vibration in the previous chapter.

Bands near  $1665\text{ cm}^{-1}$  (negative) and  $1682\text{ cm}^{-1}$  (positive) assigned in WT to the amide I mode also appear in all the mutants examined although somewhat shifted in frequency. One exception is the mutant D299N where the negative band at  $1666\text{ cm}^{-1}$  is absent (Figure 5.6).

Below is a description of the results produced by FTIR Steady State Difference Spectroscopy performed on each of the mutants discussed at 270 K with a specific eye toward the C=O stretch region in an attempt to understand the protonation/deprotonation events occurring in the *CaChR1*  $P_0 \rightarrow P_2$  in terms of the amino acid groups present in the binding pocket.

#### **E169Q mutant:**

The mutant E169Q exhibits most of the bands observed in the carboxylic C=O stretch region for WT (Figure 5.8). A small  $2\text{ cm}^{-1}$  downshift in the positive/negative band at  $1770/1763\text{ cm}^{-1}$  in WT is found indicating the corresponding COOH group is not from E169 but its hydrogen bonding is slightly altered. The largest change occurs for the positive  $1728\text{ cm}^{-1}$  band that drops in intensity relative to other bands in this region. In addition, there is a loss of intensity of the broad negative band seen in WT at  $1715\text{ cm}^{-1}$  possibly due to disappearance of the higher frequency component near  $1720\text{ cm}^{-1}$  seen using FSD. Instead a small positive band appears near  $1723\text{ cm}^{-1}$ . Thus, it is concluded that this mutant causes a drop-out of positive/negative bands near  $1728/1720\text{ cm}^{-1}$  which are assigned to E169 and are consistent with a weakening of the hydrogen bonding of the E169 COOH group during the *CaChR1*  $P_0 \rightarrow P_2$ <sup>380</sup> transition.

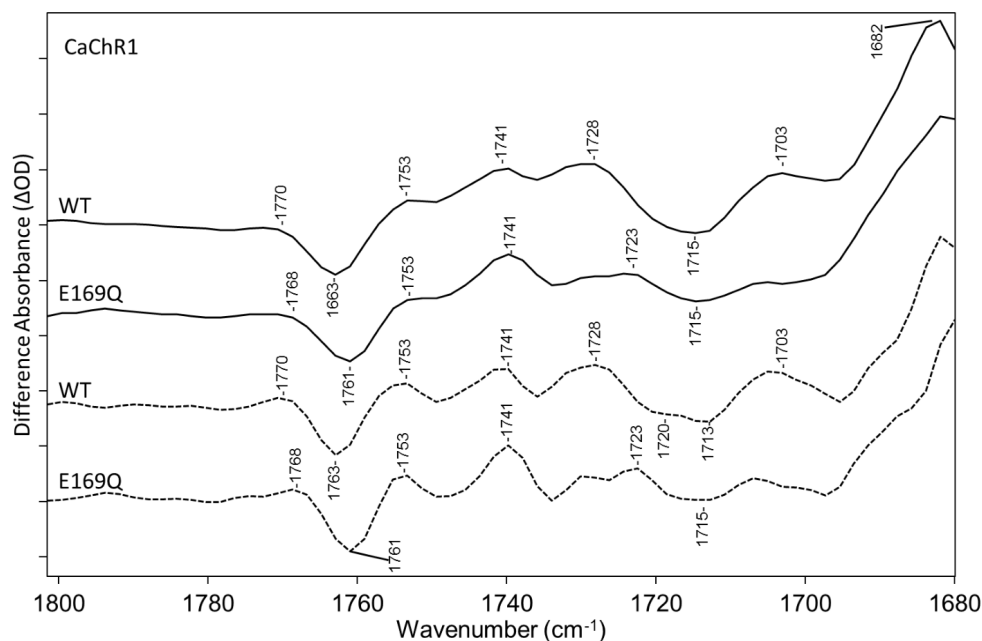


Figure 5.8: FTIR-difference spectra in the  $1680\text{-}1800\text{ cm}^{-1}$  region of *CaChR1* WT (first and third spectra) and the mutant E169Q (second and fourth spectra) recorded at 270 K. Dashed plots show FSD processed spectra. Y-axis markers are approximately 0.1 mOD and 0.06 mOD for WT and E169Q spectra, respectively.

#### **D299E mutant:**

Although as noted above, a *13-cis* retinal species is present in the D299E mutant, its contribution to the *CaChR1*  $P_0 \rightarrow P_2^{380}$  difference spectrum could be minimized by using the decay protocol instead of photoreversal method described in Materials and Methods chapter. In this case the negative band at  $1183\text{ cm}^{-1}$  and a high frequency shoulder on the negative ethylenic located at  $1541\text{ cm}^{-1}$ , both reflective of the *13-cis* species, was reduced. Importantly, in either case of photoreversal or decay, the  $1680\text{-}1800\text{ cm}^{-1}$  region was very similar. The largest change observed for this mutant is a decrease in intensity in the region  $1740\text{-}1753\text{ cm}^{-1}$  (Figure 5.9). Along with these changes a significant increase in intensity occurs near  $1722\text{ cm}^{-1}$ . The bands near  $1741$  and  $1728\text{ cm}^{-1}$  in WT may also be present as part of the broad positive high-frequency shoulder of the  $1722\text{ cm}^{-1}$  band as seen most clearly in the D299E FSD difference spectrum. The positive band at

1703  $\text{cm}^{-1}$  also disappears in the D299E mutant which, in the case of WT may be due to residual contributions from the  $P_1$  intermediate and assigned in previous chapters to D299 protonation [105]. It is also noted that negative bands still appear near 1761  $\text{cm}^{-1}$  but downshifted by 2  $\text{cm}^{-1}$  similar to E169Q. Overall, the most likely explanation for these changes is that a positive band located in the region between 1740-1750  $\text{cm}^{-1}$ , assigned to D299, downshifts 20-30  $\text{cm}^{-1}$  due to the longer side-chain (one carbon extra) in Glu compared to Asp. Such a downshift due to a Asp→Glu substitution is not unusual and occurs in the BR mutant D85E where the positive 1761  $\text{cm}^{-1}$  band assigned to Asp85 downshifts approximately 30  $\text{cm}^{-1}$  in the BR→M<sub>412</sub> difference spectrum [91].

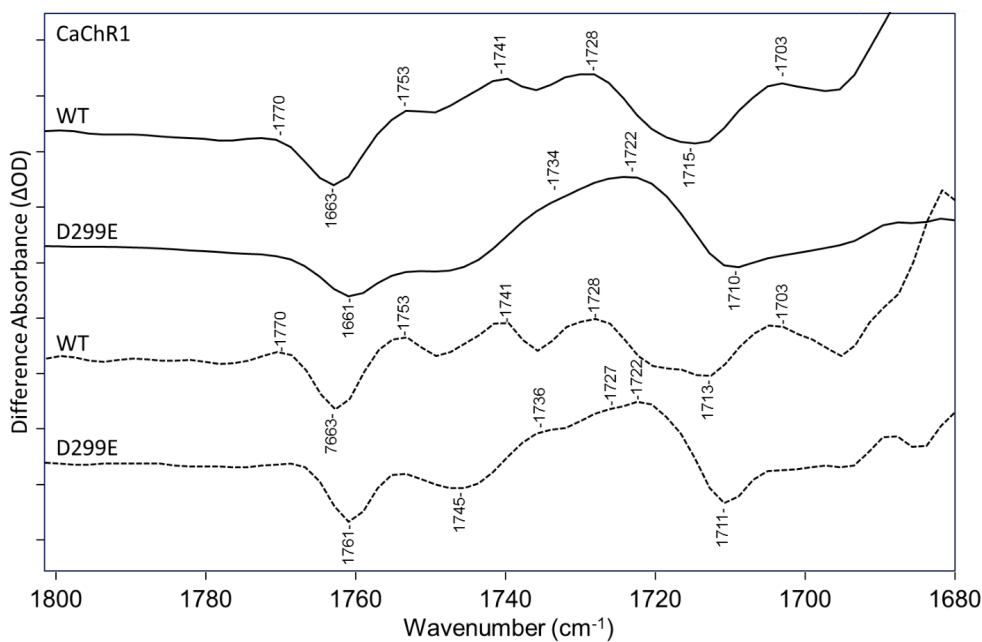


Figure 5.9: FTIR-difference spectra in the 1680-1800  $\text{cm}^{-1}$  region of *CaChR1* WT (first and third spectra) and the mutant D299E (second and fourth spectra) recorded at 270 K. Dashed plots show FSD processed spectra. Y-axis markers are approximately 0.1 mOD and 0.03 mOD for WT and D299E spectra, respectively.

**D299N mutant:**

Similar to D299E, a drop in positive intensity occurs from 1740-1753  $\text{cm}^{-1}$  again consistent with contributions from Asp299 protonation in the WT spectrum in this region (Figure 5.10). For example, band appearing near 1741  $\text{cm}^{-1}$  in WT is no longer present in D299N, replaced by a positive band near 1732  $\text{cm}^{-1}$  similar to the shoulder in D299E. However, the larger band at 1722  $\text{cm}^{-1}$  appearing in D299E is not present as expected since it was attributed to a downshift of the D299 band due to the Asp to Glu substitution. In addition, the negative 1720  $\text{cm}^{-1}$  band, which is resolved in the FSD of WT and assigned to deprotonation of E169, disappears in D299N spectrum. This is consistent with the earlier conclusion that E169 is ionized in the unphotolyzed state of D299N [101,105]. A positive band also appears in D299N at 1732  $\text{cm}^{-1}$ , upshifted from the WT positive band at 1728  $\text{cm}^{-1}$  consistent with E169 still becoming protonated upon  $\text{P}_2^{380}$  formation in this mutant but with a slightly weaker hydrogen bonding.

**F139K mutant:**

The changes induced are very similar to the mutant E169Q in this region (Figure 5.11). For example, the positive 1728  $\text{cm}^{-1}$  band in WT drops in intensity relative to other bands in this region revealing a less intense positive band at 1722  $\text{cm}^{-1}$ . The negative band at 1763  $\text{cm}^{-1}$  is also downshifted by 2  $\text{cm}^{-1}$  as observed in E169Q, D299N, and D299E but also reduced significantly in intensity relative to these other mutants. There may also be an absence of the positive 1753  $\text{cm}^{-1}$  bands observed in WT and other mutants.

## 5.2 Conclusions from 270 K FTIR Difference Spectroscopy and a Model for the *CaChR1* $\text{P}_0 \rightarrow \text{P}_1 \rightarrow \text{P}_2^{380}$ Phototransition

This chapter investigates proton transfers occurring in the low-efficiency channelrhodopsin-1 from *Chlamydomonas augustae*, *CaChR1*. *CaChR1* exhibits several properties such as red-shifted visible absorption maximum and slow light-inactivation which makes it of interest as a optogenetic controlled cation channel [66]. In addition, many of its properties including

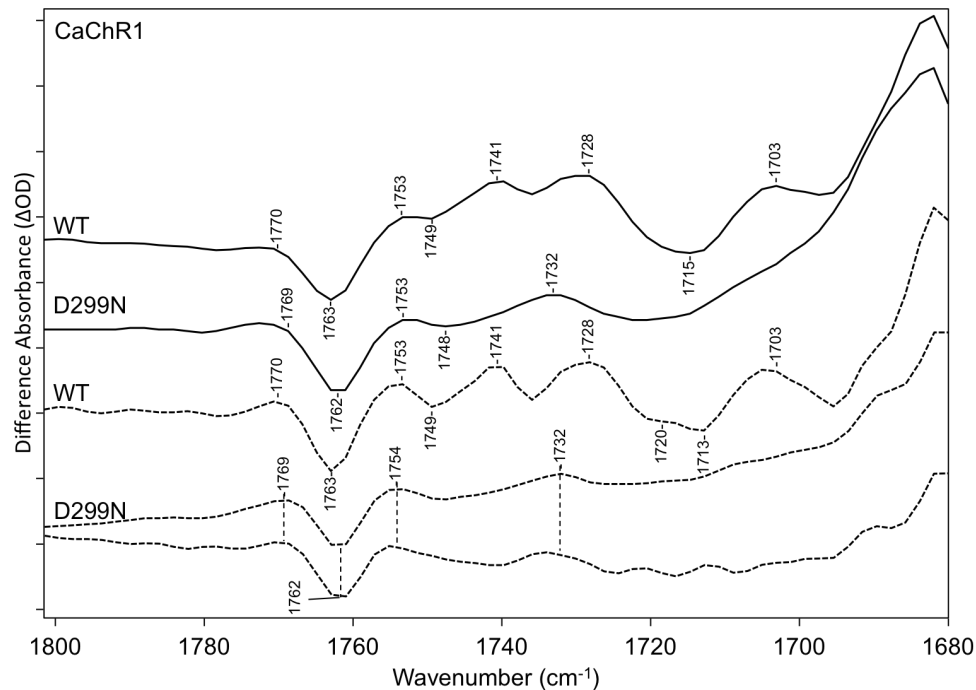


Figure 5.10: FTIR-difference spectra in the  $1680\text{-}1800\text{ cm}^{-1}$  region of *CaChR1* WT (first and third spectra) and the mutant D299N (second and fourth spectra) recorded at 270 K. Dashed plots show FSD processed spectra. Y-axis markers are approximately 0.1 mOD and 0.2 mOD for WT and D299N spectra, respectively.

the presence of a fast outward directed photocurrent and absence of a red-shift at low pH or when the Asp85 is replaced by a neutral residue appear to be common to other low-efficiency ChRs [80,101]. Although less is known about the molecular properties of *CaChR1* relative to the more extensively studied *CrChR2*, RRS from previous chapters showed that in the unphotolyzed state  $P_0$ , at least under our conditions, retinal is completely all-*trans* similar to other microbial rhodopsins including BR and *NpSR11* [80]. In contrast, a significant level of 13-*cis* retinal is found in the unphotolyzed state of *CrChR2* which can complicate analysis of its photocycle [28,80].

Previous chapters show that in contrast to BR, where both SB counterions Asp85 and Asp212 are ionized, in *CaChR1* the homologs Glu169 and Asp299 exist in a neutral and ionized state, respectively [32,80,101] (Figure 5.7). One possible explanation for this differ-

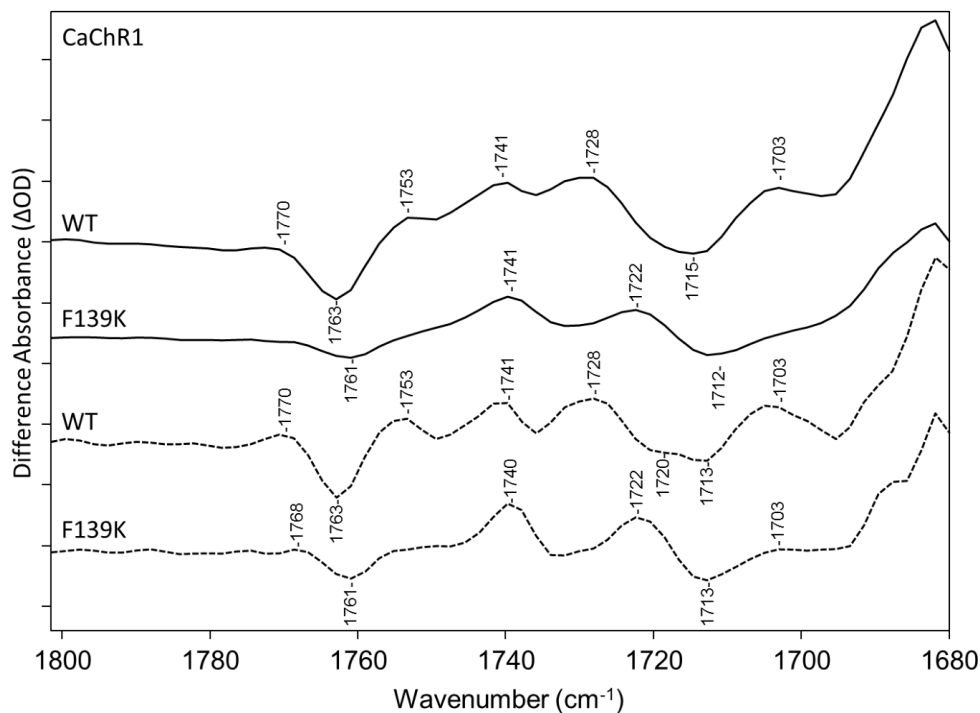


Figure 5.11: FTIR-difference spectra in the 1680-1800  $\text{cm}^{-1}$  region of *CaChR1* WT (first and third spectra) and the mutant F139K (second and fourth spectra) recorded at 270 K. Dashed plots show FSD processed spectra. Y-axis markers are approximately 0.1 mOD for both WT and D299N spectra

ence relates to Arg166, which is the homolog of Arg82 in BR. As shown in Figure 5.7–A, the positive charge on the guanidinium group of Arg82 is oriented towards the intracellular side of the bilayer membrane so that it interacts closely with Asp85. In contrast, in the case of *CaChR1*, its orientation may be directed towards the extracellular side of the membrane, thereby weakening its interaction with the homolog Glu169. The loss of this salt bridge interaction could result in an increase in the  $\text{pK}_a$  of Glu169 so that it remains protonated above pH 7 as observed [32].

In support of this explanation, substitution of Arg166 with the neutral residue Ala does not significantly shift the *CaChR1*  $\lambda_{\text{max}}$  [32] as would be expected if it interacted closely with Glu169. Interestingly, in the case of the chimera C1C2, a positively charged residue, Lys132 located on the B Helix is found to interact closely with the Asp85 homolog Glu162

(C1C2 sequence numbering) (Figure 5.12) [5, 32]. Other high-efficiency ChRs including *CrChR1* and *CrChR2* also retain a similar Lys at this position. However, in contrast, *CaChR1* and other low-efficiency ChRs have a neutral residue in this position (Phe139 in case of *CaChR1*) [32]. Thus, unlike BR, *CaChR1* and most likely other low-efficiency ChRs have an unphotolyzed state photoactive site in which the electrostatic interactions mainly occur between the positively charged SB and the Asp212 homolog, Asp299, while Asp85 homolog, Glu169, is neutral (i.e. protonated).

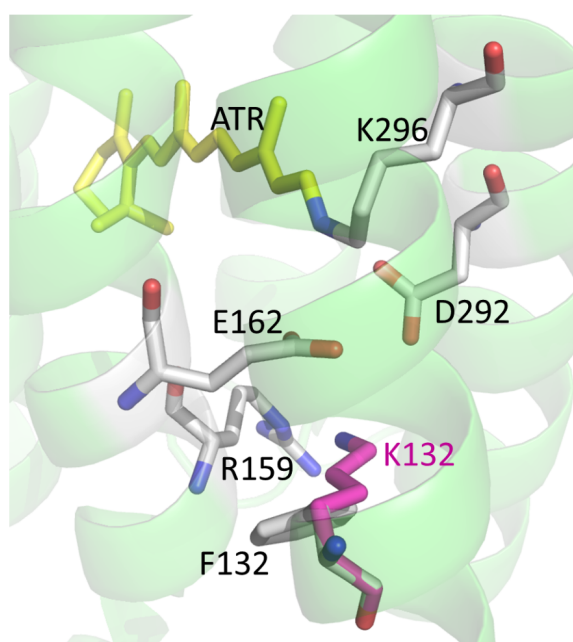


Figure 5.12: 3UG9 Structure of C1C2 chimera from Kato et al. [5] showing position of the residues homologous to the SB counterions E169 and D299 along with the positively charged residue R166 in *CaChR1*. The residue K132 (shown in pink) is the homolog to F139 in *CaChR1*. Both residues are shown as a superposition. The numbering is based on the *CrChR1* sequence.

### 5.2.1 A Proton Transfer Model

In order to further investigate the proton transfers that are involved in formation of the open (e.g. conducting) channel  $P_2^{380}$  state of *CaChR1*, FTIR-difference spectroscopy was used along with site-directed mutagenesis. It is important to stress that this approach



depends to a large extent on understanding the effects of point mutations on the overall structure and function of the protein. For this reason, the model proposed below takes into account results such as the effects of point mutations on visible absorption pH titration and photoinduced channel currents.

Since Glu169 is protonated in the unphotolyzed state of *CaChR1*, it does not appear to be a SB proton acceptor in acidic or neutral conditions, in contrast to the homolog Asp85 in BR, but Glu169 is expected to play this role at alkaline pH [32]. Photoinduced channel current measurements of *CaChR1* in the D299N mutant in HEK293 cells indicated that Glu169, when ionized, is a far more efficient acceptor than Asp299 during  $P_2^{380}$  formation. Asp299 was proposed as an alternative proton acceptor in neutral and acidic conditions and also was reported to play more of a role in channel opening than Glu169 [101].

This chapter, in addition to the two chapters present previously describing RRS and 80K FTIR difference spectroscopy suggests a model of the proton transfers in the early photocycle of *CaChR1* that is consistent with the biophysical studies [66, 80, 101, 105]. The model postulates that a proton transfer relay mechanism exists between the SB and Asp299 involving two steps (Figure 5.13): (i) A proton is transferred from Glu169 to Asp299 during the formation of the  $P_1$  intermediate leaving the Glu169 in an ionized state and Asp299 neutral and (ii) Glu169, now in an ionized state in  $P_1$ , accepts a proton from the SB upon its deprotonation and formation of  $P_2^{380}$ . Thus, as discussed below, in the  $P_2^{380}$  both SB counterions are neutral, possibly triggering channel opening and the flow of cations.

Evidence supporting this model based on the FTIR-difference and the effects of mutagenesis is summarized below:

### **Asp299 is protonated in $P_2^{380}$**

As described in Section 5.1.1, positive intensity appears in the *CaChR1*  $P_0 \rightarrow P_2^{380}$  difference spectrum between 1740-1753  $\text{cm}^{-1}$  which is assigned to Asp299. This is consistent with either a net protonation of the Asp299 carboxylate or hydrogen bond alteration of the Asp299 carboxylic acid group which occurs between the unphotolyzed state and  $P_2^{380}$ .

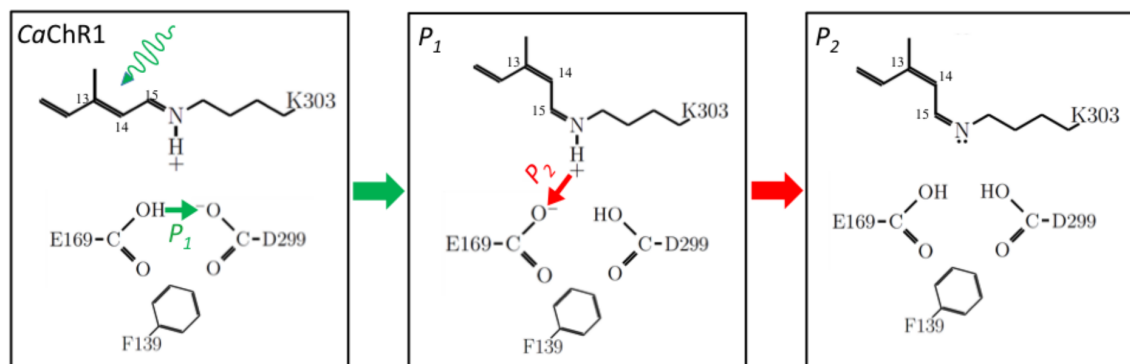


Figure 5.13: Schematic model showing the proposed protonation of the unphotolyzed  $P_0$  state,  $P_1$ , and  $P_2^{380}$  intermediates in *CaChR1* along with proposed proton transfers. Large green arrow indicates the photon absorption by the unphotolyzed *CaChR1*. Smaller arrows indicating proton transfers that occur during the  $P_0 \rightarrow P_1$  light-driven transition (green) and  $P_1 \rightarrow P_2^{380}$  thermal transition (red).

However, as described above independent evidence establishes that at neutral pH Asp299 is ionized in the unphotolyzed state [101] ruling out the second possibility (a hydrogen bond alteration of a neutral carboxyl group). In addition, a positive band at  $1703 \text{ cm}^{-1}$  was assigned to the protonation of Asp299 during  $P_1$  formation in the 80 K FTIR studies of the previous chapter [105]. It is unknown if this protonation of Asp299 occurs during or after 13-*cis* isomerization of the retinal chromophore in  $P_1$  formation. However, ultrafast infrared spectroscopy on *CrChR2* reveal a fast deactivation of the excited state followed quickly within 0.5 ps of protein structural changes [109]. These findings strongly argue against the possibility that Asp299 functions as the primary SB proton acceptor during  $P_2^{380}$  formation. Instead, the upshift in frequency of the Asp299 bands assigned in  $P_1$  ( $1703 \text{ cm}^{-1}$ ) and  $P_2^{380}$  (near  $1741 \text{ cm}^{-1}$ ) indicates that its COOH group undergoes a significant weakening in hydrogen bonding between these two states. This is consistent with a loss of the carboxyl-carboxylate interaction formed between Glu169 and Asp299 in the unphotolyzed  $P_0$  and  $P_1$  states but lost in  $P_2^{380}$  as shown in Figure 5.13.

### **Glu169 acts as SB proton acceptor during formation of $P_2^{380}$**

A negative band between 1710-1720  $\text{cm}^{-1}$  was assigned to Glu169 during the *CaChR1*  $P_0 \rightarrow P_1$  primary transition indicating that this residue deprotonates during this step of the photocycle [105] (Figure 5.13). Consistent with this original assignment, a negative band is now assigned to Glu169 near 1720  $\text{cm}^{-1}$  in the *CaChR1*  $P_0 \rightarrow P_2^{380}$  difference spectrum. In addition a positive band assigned to Glu169 appears near 1728  $\text{cm}^{-1}$  indicating the reprotonation of Glu169 from the SB upon  $P_2^{380}$  formation. The upshift in frequency from approximately 1720 to 1728  $\text{cm}^{-1}$  is consistent with a loss of the strong carboxylate/carboxylic acid (Asp299/Asp169) interaction postulated to exist in the ground state and replaced by two neutral forms of these residues in  $P_2^{380}$  (Figure 5.13).

### **F139K has similar effect as E169Q in the carboxylic acid stretch region**

The band assigned to the protonated form of Glu169 at 1728  $\text{cm}^{-1}$  disappears in both the E169Q and F139K difference spectra. This observation is consistent with the proposed model since like, the mutant E169Q, substitution of Phe139 with a Lys could prevent Glu169 from functioning as the SB acceptor group and abolish the band assigned to the protonation of this group. This might occur for example, if the SB proton transferred directly to Asp299.

One unusual feature of this model of  $P_2^{380}$  is that both SB counterions exist in a neutral state along with a non-protonated SB. For example, in the case of the  $M_{412}$  intermediate of BR, Asp85 is neutral but Asp212 still has a full or partially negative charge (Figure 5.7-A). Similar results have also been deduced from FTIR studies of proteorhodopsin and *NpSR*II [110]. One possible explanation for this feature is that the region near these two residues and the SB functions as a type of selectivity filter for the *CaChR1* cation channel which opens at  $P_2^{380}$ . For example, many  $\text{K}^+$  channels contain a selectivity filter consisting of a narrow pore lined by electronegative carbonyl groups which are positioned to replace the inner solvation shell of the permeating cation [111]. In contrast, it is unlikely that a fully

ionized carboxylate group would mimic solvation waters surrounding a cation and in fact might constitute an effective block for passive permeation. In support of this possibility, the chimeric C1C2 structure [5] reveals a putative cation pore which involves electronegative surfaces formed by helices A, B, C, and G including Glu162 and Asp299 (homologs of Glu169 and Asp299 in *CaChR1*) which are aligned along the pore surface and thus might be in a position to help control cation permeation. In fact, the presence of the positively charged SB and negatively charged Asp299 in the *CaChR1* unphotolyzed P<sub>0</sub> (Figure 5.12) could act as an effective block for cation permeation in contrast to the P<sub>2</sub><sup>380</sup> state where both Glu169 and Asp299 are neutral.

The presence of a neutral residue (Glu169) in *CaChR1* as opposed to a negative charge for the homologous residue in *CrChR2* [72] could also account for the red-shifted  $\lambda_{\max}$  (525 nm vs. 470 nm). Such a red-shift is predicted on the basis of a simple point charge model for the SB counterion [58] and supported by earlier studies. For example, neutralization of Asp85 in BR at low pH accounts for its observed red-shift [63]. The red-shifted  $\lambda_{\max}$  of sensory rhodopsin I at pH below 7 is also accounted for by neutralization of the Asp76 SB proton counterion [112]. However, other factors such the existence of an internal water molecule(s) positioned near the SB as in the case of W402 in BR [6] are also likely to play a role in the determination of the wavelength of visible absorption .

Another difference between BR, *CaChR1* and *CrChR2* is the isomer content in light and dark-adapted states. In *CaChR1* , both RRS and FTIR evidence indicates the chromophore remains in an almost pure all-*trans* isomer form [80,105]. In contrast, upon dark-adaptation, BR reverts to approximately a 50/50 mixture of all-*trans* and 13-*cis* retinal [39, 113, 114]. In addition, *CrChR2* has a mixture of all-*trans* and 13-*cis* retinal in both light and dark-adapted states [28]. This may indicate that the retinal binding pocket of *CaChR1* , unlike BR and *CrChR2* , does not easily accommodate a 13-*cis* retinal isomeric state. This would not be entirely unprecedented since a similar conclusion was reached for *NpSR11* on the basis of measurements on the rate of 13-*cis* retinal regeneration [41].

Further studies including additional FTIR- difference spectroscopy, kinetic visible ab-

sorption and mutagenesis experiments along with isotope labeling of residues will be necessary to test the suggested proton transfer model in *CaChR1* as well as in other low- efficiency ChRs. In this regard, it is interesting to note that the presence of a positively charged residue (e.g. Lys132) nearby the Asp85 homolog in *CrChR2* and other high-efficiency ChRs [101] is likely to result in a different dark state photoactive site and altered proton transfers compared to *CaChR1* and other low-efficiency ChRs.

## Bibliography

- [1] Yoshinori Shichida and Take Matsuyama. Evolution of opsins and phototransduction. *Philosophical Transactions of the Royal Society B: Biological Sciences*, 364(1531):2881–2895, 2009.
- [2] Burton J Litman and Drake C Mitchell. Rhodopsin structure and function. *Biomembranes: A Multi-Volume Treatise*, 2:1–32, 1996.
- [3] Walther Stoeckenius, Richard H Lozier, and Roberto A Bogomolni. Bacteriorhodopsin and the purple membrane of halobacteria. *Biochimica et Biophysica Acta (BBA)-Reviews on Bioenergetics*, 505(3):215–278, 1979.
- [4] Dieter Oesterhelt and Walther Stoeckenius. Rhodopsin-like protein from the purple membrane of halobacterium halobium. *Nature*, 233(39):149–152, 1971.
- [5] Hideaki E Kato, Feng Zhang, Ofer Yizhar, Charu Ramakrishnan, Tomohiro Nishizawa, Kunio Hirata, Jumpei Ito, Yusuke Aita, Tomoya Tsukazaki, Shigehiko Hayashi, et al. Crystal structure of the channelrhodopsin light-gated cation channel. *Nature*, 482(7385):369–374, 2012.
- [6] Hartmut Luecke, Brigitte Schobert, Hans-Thomas Richter, Jean-Philippe Cartailier, and Janos K Lanyi. Structure of bacteriorhodopsin at 1.55 Å resolution. *Journal of Molecular Biology*, 291(4):899–911, 1999.
- [7] Paula J Booth. Folding  $\alpha$ -helical membrane proteins: kinetic studies on bacteriorhodopsin. *Folding and Design*, 2(6):R85–R92, 1997.
- [8] Mark P Krebs and Thomas A Isenbarger. Structural determinants of purple membrane assembly. *Biochimica et Biophysica Acta (BBA)-Bioenergetics*, 1460(1):15–26, 2000.
- [9] Janos K Lanyi. Bacteriorhodopsin as a model for proton pumps. *Nature*, 375(6531):461–463, 1995.

- [10] David G Nicholls and Stuart Ferguson. *Bioenergetics*. Academic Press, 2013.
- [11] Janos K Lanyi. Bacteriorhodopsin. *Annual Review of Physiology*, 66:665–688, 2004.
- [12] Erik Freier, Steffen Wolf, and Klaus Gerwert. Proton transfer via a transient linear water-molecule chain in a membrane protein. *Proceedings of the National Academy of Sciences*, 108(28):11435–11439, 2011.
- [13] KJ Rothschild and S Sonar. Bacteriorhodopsin: New biophysical perspectives. *CRC handbook of organic photochemistry and photobiology*. Horspool WM and PS. Song, editors. CRC Press, Inc, London, pages 1521–1544, 1995.
- [14] Marcel Baer, Gerald Mathias, I Kuo, W Feng, Douglas J Tobias, Christopher J Mundy, and Dominik Marx. Spectral signatures of the pentagonal water cluster in bacteriorhodopsin. *ChemPhysChem*, 9(18):2703–2707, 2008.
- [15] Yasuhiro Matsui, Keisuke Sakai, Midori Murakami, Yoshitsugu Shiro, Shin-ichi Adachi, Hideo Okumura, and Tsutomu Kouyama. Specific damage induced by x-ray radiation and structural changes in the primary photoreaction of bacteriorhodopsin. *Journal of molecular biology*, 324(3):469–481, 2002.
- [16] Hendrik Naumann. *The NpSR II photocycle and its dependence on the electric field—a combined quantum chemical and Raman spectroscopic study*. PhD thesis, PhD thesis, Technische Universität Berlin, 2009.
- [17] Antoine Royant, Peter Nollert, Karl Edman, Richard Neutze, Ehud M Landau, Eva Pebay-Peyroula, and Javier Navarro. X-ray structure of sensory rhodopsin ii at 2.1- $\text{\AA}$  resolution. *Proceedings of the National Academy of Sciences*, 98(18):10131–10136, 2001.
- [18] Hideki Kandori, Kazumi Shimono, Yuki Sudo, Masayuki Iwamoto, Yoshinori Shichida, and Naoki Kamo. Structural changes of pharaonis phoborhodopsin upon photoiso-

- merization of the retinal chromophore: infrared spectral comparison with bacteriorhodopsin. *Biochemistry*, 40(31):9238–9246, 2001.
- [19] Yuki Sudo and John L Spudich. Three strategically placed hydrogen-bonding residues convert a proton pump into a sensory receptor. *Proceedings of the National Academy of Sciences*, 103(44):16129–16134, 2006.
- [20] Daisuke Suzuki, Hiroki Irieda, Michio Homma, Ikuro Kawagishi, and Yuki Sudo. Phototactic and chemotactic signal transduction by transmembrane receptors and transducers in microorganisms. *Sensors*, 10(4):4010–4039, 2010.
- [21] Vladislav Bergo, Elena N Spudich, Kenneth L Scott, John L Spudich, and Kenneth J Rothschild. Ftir analysis of the sii540 intermediate of sensory rhodopsin ii: Asp73 is the schiff base proton acceptor. *Biochemistry*, 39(11):2823–2830, 2000.
- [22] Jun Sasaki and John L Spudich. Proton circulation during the photocycle of sensory rhodopsin ii. *Biophysical Journal*, 77(4):2145–2152, 1999.
- [23] Ming Ming, Miao Lu, Sergei P Balashov, Thomas G Ebrey, Qingguo Li, and Jiandong Ding. ph dependence of light-driven proton pumping by an archaerhodopsin from tibet: comparison with bacteriorhodopsin. *Biophysical Journal*, 90(9):3322–3332, 2006.
- [24] Oleg A Sineshchekov, Kwang-Hwan Jung, and John L Spudich. Two rhodopsins mediate phototaxis to low-and high-intensity light in chlamydomonas reinhardtii. *Proceedings of the National Academy of Sciences*, 99(13):8689–8694, 2002.
- [25] John Y Lin. A user’s guide to channelrhodopsin variants: features, limitations and future developments. *Experimental physiology*, 96(1):19–25, 2011.
- [26] David W Ball. Theory of raman spectroscopy. *Spectroscopy*, 16(11):32–34, 2001.
- [27] V A Lorenz-Fonfria, V Muders, R Schlesinger, and J Heberle. Changes in the hydrogen-bonding strength of internal water molecules and cysteine residues in the conductive state of channelrhodopsin-1. *Journal of Physical Chemistry*, 141, 2014.



- [28] Melanie Nack, Ionela Radu, Christian Bamann, Ernst Bamberg, and Joachim Heberle. The retinal structure of channelrhodopsin-2 assessed by resonance raman spectroscopy. *FEBS letters*, 583(22):3676–3680, 2009.
- [29] Vera Muders, Silke Kerruth, Víctor A Lórenz-Fonfría, Christian Bamann, Joachim Heberle, and Ramona Schlesinger. Resonance raman and ftir spectroscopic characterization of the closed and open states of channelrhodopsin-1. *FEBS letters*, 2014.
- [30] Steven J Milder, Thorgeir E Thorgeirsson, Larry JW Miercke, Robert M Stroud, and David S Kliger. Effects of detergent environments on the photocycle of purified monomeric bacteriorhodopsin. *Biochemistry*, 30(7):1751–1761, 1991.
- [31] Annela M Seddon, Paul Curnow, and Paula J Booth. Membrane proteins, lipids and detergents: not just a soap opera. *Biochimica et Biophysica Acta (BBA)-Biomembranes*, 1666(1):105–117, 2004.
- [32] Hai Li, Elena G Govorunova, Oleg A Sineshchekov, and John L Spudich. Role of a helix b lysine residue in the photoactive site in channelrhodopsins. *Biophysical Journal*, 106(8):1607–1617, 2014.
- [33] Christian Bamann, Ronnie Gueta, Sonja Kleinlogel, Georg Nagel, and Ernst Bamberg. Structural guidance of the photocycle of channelrhodopsin-2 by an interhelical hydrogen bond. *Biochemistry*, 49(2):267–278, 2009.
- [34] Peter R Griffiths and John M Chalmers. *Handbook of vibrational spectroscopy*. J. Wiley., 2002.
- [35] Peter R Griffiths and James A De Haseth. *Fourier transform infrared spectrometry*, volume 171. John Wiley & Sons, 2007.
- [36] Kenneth J Rothschild, Hector Marrero, Mark Braiman, and Richard Mathies. Primary photochemistry of bacteriorhodopsin: comparison of fourier transform infrared

- difference spectra with resonance raman spectra. *Photochemistry and photobiology*, 40(5):675–679, 1984.
- [37] Steven O Smith, AB Myers, RA Mathies, JA Pardoen, C Winkel, EM van den Berg, and J Lugtenburg. Vibrational analysis of the all-trans retinal protonated schiff base. *Biophysical Journal*, 47(5):653–664, 1985.
- [38] Steven O Smith, Johan Lugtenburg, and Richard A Mathies. Determination of retinal chromophore structure in bacteriorhodopsin with resonance raman spectroscopy. *Journal of Membrane Biology*, 85(2):95–109, 1985.
- [39] Steven O Smith, Johannes A Pardoen, Johan Lugtenburg, and Richard A Mathies. Vibrational analysis of the 13-cis-retinal chromophore in dark-adapted bacteriorhodopsin. *Journal of Physical Chemistry*, 91(4):804–819, 1987.
- [40] Steven O Smith, Huub JM De Groot, Ronald Gebhard, Jacques ML Courtin, Johan Lugtenburg, Judith Herzfeld, and Robert G Griffin. Structure and protein environment of the retinal chromophore in light-and dark-adapted bacteriorhodopsin studied by solid-state nmr. *Biochemistry*, 28(22):8897–8904, 1989.
- [41] Junichi Hirayma, Naoki Kamo, Yasushi Imamoto, Yoshinori Shichida, and Toru Yoshizawa. Reason for the lack of light-dark adaptation in pharaonis phoborhodopsin: reconstitution with 13- cis-retinal. *FEBS letters*, 364(2):168–170, 1995.
- [42] Steven O Smith, Irene Hornung, Rob Van Der Steen, Johannes A Pardoen, Mark S Braiman, Johan Lugtenburg, and Richard A Mathies. Are c14-c15 single bond isomerizations of the retinal chromophore involved in the proton-pumping mechanism of bacteriorhodopsin? *Proceedings of the National Academy of Sciences*, 83(4):967–971, 1986.
- [43] Erica C Saint Clair, John I Ogren, Sergey Mamaev, Daniel Russano, Joel M Kralj, and Kenneth J Rothschild. Near-ir resonance raman spectroscopy of archaerhodopsin

- 3: effects of transmembrane potential. *The Journal of Physical Chemistry B*, 116(50):14592–14601, 2012.
- [44] Joel M Kralj, Elena N Spudich, John L Spudich, and Kenneth J Rothschild. Raman spectroscopy reveals direct chromophore interactions in the leu/gln105 spectral tuning switch of proteorhodopsins. *The Journal of Physical Chemistry B*, 112(37):11770–11776, 2008.
- [45] Víctor A Lórenz-Fonfría, Tom Resler, Nils Krause, Melanie Nack, Michael Gossing, Gabriele Fischer von Mollard, Christian Bamann, Ernst Bamberg, Ramona Schlesinger, and Joachim Heberle. Transient protonation changes in channelrhodopsin-2 and their relevance to channel gating. *Proceedings of the National Academy of Sciences*, 110(14):E1273–E1281, 2013.
- [46] Ionela Radu, Christian Bamann, Melanie Nack, Georg Nagel, Ernst Bamberg, and Joachim Heberle. Conformational changes of channelrhodopsin-2. *Journal of the American Chemical Society*, 131(21):7313–7319, 2009.
- [47] O Bousché, M Braiman, YW He, T Marti, HG Khorana, and KJ Rothschild. Vibrational spectroscopy of bacteriorhodopsin mutants. evidence that asp-96 deprotonates during the m—n transition. *Journal of Biological Chemistry*, 266(17):11063–11067, 1991.
- [48] Olaf Bousché, Sanjay Sonar, Mark P Krebs, H Gobind Khorana, and Kenneth J Rothschild. Time-resolved fourier transform infrared spectroscopy of the bacteriorhodopsin mutant tyr-185 e: Asp-96 reprotonates during o formation; asp-85 and asp-212 deprotonate during o decay. *Photochemistry and photobiology*, 56(6):1085–1095, 1992.
- [49] Stephen PA Fodor, James B Ames, Ronald Gebhard, Ellen MM Van den Berg, Walther Stoeckenius, Johan Lugtenburg, and Richard A Mathies. Chromophore structure in bacteriorhodopsin’s n intermediate: implications for the proton-pumping mechanism. *Biochemistry*, 27(18):7097–7101, 1988.

- [50] Mark Braiman and Richard Mathies. Resonance raman evidence for an all-trans to 13-cis isomerization in the proton-pumping cycle of bacteriorhodopsin. *Biochemistry*, 19(23):5421–5428, 1980.
- [51] H Deng, C Pande, RH Callender, and TG Ebrey. A detailed resonance raman study of the m412 intermediate in the bacteriorhodopsin photocycle. *Photochemistry and photobiology*, 41(4):467–470, 1985.
- [52] SP Fodor, R Gebhard, J Lugtenburg, RA Bogomolni, and RA Mathies. Structure of the retinal chromophore in sensory rhodopsin i from resonance raman spectroscopy. *Journal of Biological Chemistry*, 264(31):18280–18283, 1989.
- [53] Igor Chizhov, Georg Schmies, Ralf Seidel, Jens R Sydor, Beate Lüttenberg, and Martin Engelhard. The photophobic receptor from natronobacterium pharaonis: Temperature and ph dependencies of the photocycle of sensory rhodopsin ii. *Biophysical Journal*, 75(2):999–1009, 1998.
- [54] Tetsuo Takahashi, Bing Yan, Paul Mazur, Fadila Derguini, Koji Nakanishi, and John L Spudich. Color regulation in the archaeobacterial phototaxis receptor phoborhodopsin (sensory rhodopsin ii). *Biochemistry*, 29(36):8467–8474, 1990.
- [55] Pramod V Argade and Kenneth J Rothschild. Quantitative analysis of resonance raman spectra of purple membrane from halobacterium halobium: L550 intermediate. *Biochemistry*, 22(14):3460–3466, 1983.
- [56] SP Fodor, Walter T Pollard, Ronald Gebhard, EM van den Berg, Johan Lugtenburg, and Richard A Mathies. Bacteriorhodopsin’s l550 intermediate contains a c14-c15 s-trans-retinal chromophore. *Proceedings of the National Academy of Sciences*, 85(7):2156–2160, 1988.
- [57] Kenneth J Rothschild, WJ De Grip, HE Stanley, et al. Opsin structure probed by raman spectroscopy of photoreceptor membranes. *Science*, 191(4232):1176–1178, 1976.

- [58] Barry Honig, Uri Dinur, Koji Nakanishi, Valeria Balogh-Nair, Mary Ann Gawinowicz, Maria Arnaboldi, and Michael G Motto. An external point-charge model for wavelength regulation in visual pigments. *Journal of the American Chemical Society*, 101(23):7084–7086, 1979.
- [59] Aaron Lewis, John Spoonhower, Roberto A Bogomolni, Richard H Lozier, and Walther Stoeckenius. Tunable laser resonance raman spectroscopy of bacteriorhodopsin. *Proceedings of the National Academy of Sciences*, 71(11):4462–4466, 1974.
- [60] Timor Baasov, Noga Friedman, and Mordechai Sheves. Factors affecting the c: N stretching in protonated retinal schiff base: a model study for bacteriorhodopsin and visual pigments. *Biochemistry*, 26(11):3210–3217, 1987.
- [61] Cristina Gellini, Beate Lüttenberg, Jens Sydor, Martin Engelhard, and Peter Hildebrandt. Resonance raman spectroscopy of sensory rhodopsin ii from natronobacterium pharaonis. *FEBS letters*, 472(2):263–266, 2000.
- [62] Steven O Smith and RA Mathies. Resonance raman spectra of the acidified and deionized forms of bacteriorhodopsin. *Biophysical Journal*, 47(2):251–254, 1985.
- [63] Parshuram Rath, T Marti, Sanjay Sonar, H Gobind Khorana, and KJ Rothschild. Hydrogen bonding interactions with the schiff base of bacteriorhodopsin. resonance raman spectroscopy of the mutants d85n and d85a. *Journal of Biological Chemistry*, 268(24):17742–17749, 1993.
- [64] Vladislav B Bergo, Maria Ntefidou, Vishwa D Trivedi, Jason J Amsden, Joel M Kralj, Kenneth J Rothschild, and John L Spudich. Conformational changes in the photocycle of anabaena sensory rhodopsin absence of the schiff base counterion protonation signal. *Journal of Biological Chemistry*, 281(22):15208–15214, 2006.
- [65] Peter Hegemann and Georg Nagel. From channelrhodopsins to optogenetics. *EMBO molecular medicine*, 5(2):173–176, 2013.

- [66] Sing-Yi Hou, Elena G Govorunova, Maria Ntefidou, C Elizabeth Lane, Elena N Spudich, Oleg A Sineshchekov, and John L Spudich. Diversity of chlamydomonas channelrhodopsins. *Photochemistry and photobiology*, 88(1):119–128, 2012.
- [67] Eglof Ritter, Katja Stehfest, Andre Berndt, Peter Hegemann, and Franz J Bartl. Monitoring light-induced structural changes of channelrhodopsin-2 by uv-visible and fourier transform infrared spectroscopy. *Journal of Biological Chemistry*, 283(50):35033–35041, 2008.
- [68] Istvan Szundi and Walther Stoeckenius. Effect of lipid surface charges on the purple-to-blue transition of bacteriorhodopsin. *Proceedings of the National Academy of Sciences*, 84(11):3681–3684, 1987.
- [69] Lóránd Kelemen, Péter Galajda, Sándor Száraz, and Pál Ormos. Chloride ion binding to bacteriorhodopsin at low ph: an infrared spectroscopic study. *Biophysical Journal*, 76(4):1951–1958, 1999.
- [70] Daisuke Suzuki, Yuji Furutani, Keiichi Inoue, Takashi Kikukawa, Makoto Sakai, Masaaki Fujii, Hideki Kandori, Michio Homma, and Yuki Sudo. Effects of chloride ion binding on the photochemical properties of salinibacter sensory rhodopsin i. *Journal of molecular biology*, 392(1):48–62, 2009.
- [71] Louisa Reissig, Tatsuya Iwata, Takashi Kikukawa, Makoto Demura, Naoki Kamo, Hideki Kandori, and Yuki Sudo. Influence of halide binding on the hydrogen bonding network in the active site of salinibacter sensory rhodopsin i. *Biochemistry*, 51(44):8802–8813, 2012.
- [72] Shota Ito, Hideaki E Kato, Reiya Taniguchi, Tatsuya Iwata, Osamu Nureki, and Hideki Kandori. Water-containing hydrogen-bonding network in the active center of channelrhodopsin. *Journal of the American Chemical Society*, 136(9):3475–3482, 2014.

- [73] K Bagley, G Dollinger, L Eisenstein, AK Singh, and L Zimanyi. Fourier transform infrared difference spectroscopy of bacteriorhodopsin and its photoproducts. *Proceedings of the National Academy of Sciences*, 79(16):4972–4976, 1982.
- [74] Kenneth J Rothschild and Hector Marrero. Infrared evidence that the schiff base of bacteriorhodopsin is protonated: br570 and k intermediates. *Proceedings of the National Academy of Sciences*, 79(13):4045–4049, 1982.
- [75] Kenneth J Rothschild, Paul Roepe, Johan Lugtenburg, and Johannes A Pardoën. Fourier transform infrared evidence for schiff base alteration in the first step of the bacteriorhodopsin photocycle. *Biochemistry*, 23(25):6103–6109, 1984.
- [76] Friedrich SIEBERT and Werner MÄNTELE. Investigation of the primary photochemistry of bacteriorhodopsin by low-temperature fourier-transform infrared spectroscopy. *European journal of biochemistry*, 130(3):565–573, 1983.
- [77] Vladislav Bergo, Jason J Amsden, Elena N Spudich, John L Spudich, and Kenneth J Rothschild. Structural changes in the photoactive site of proteorhodopsin during the primary photoreaction. *Biochemistry*, 43(28):9075–9083, 2004.
- [78] V Bergo, E N Spudich, J L Spudich, and K J Rothschild. A fourier transform infrared study of neurospora rhodopsin: similarities with archaeal rhodopsins. *Photochem Photobiol*, 76:341–349, 2002.
- [79] Vladislav Bergo, Elena N Spudich, John L Spudich, and Kenneth J Rothschild. Conformational changes detected in a sensory rhodopsin ii-transducer complex. *Journal of Biological Chemistry*, 278(38):36556–36562, 2003.
- [80] John I Ogren, Sergey Mamaev, Daniel Russano, Hai Li, John L Spudich, and Kenneth J Rothschild. Retinal chromophore structure and schiff base interactions in the red-shifted channelrhodopsin-1 from *chlamydomonas augustae*. *Biochemistry*, 2014.

- [81] Steven O Smith, Mark S Braiman, Anne B Myers, Johannes A Pardoën, Jacques ML Courtin, Chris Winkel, Johan Lugtenburg, and Richard A Mathies. Vibrational analysis of the all-trans-retinal chromophore in light-adapted bacteriorhodopsin. *Journal of the American Chemical Society*, 109(10):3108–3125, 1987.
- [82] Erica C Saint Clair, John I Ogren, Sergey Mamaev, Joel M Kralj, and Kenneth J Rothschild. Conformational changes in the archaerhodopsin-3 proton pump: detection of conserved strongly hydrogen bonded water networks. *Journal of biological physics*, 38(1):153–168, 2012.
- [83] Jason J Amsden, Joel M Kralj, Vladislav B Bergo, Elena N Spudich, John L Spudich, and Kenneth J Rothschild. Different structural changes occur in blue- and green-proteorhodopsins during the primary photoreaction. *Biochemistry*, 47(44):11490–11498, 2008.
- [84] M Engelhard, B Scharf, and F Siebert. Protonation changes during the photocycle of sensory rhodopsin ii from *Natronobacterium pharaonis*. *FEBS letters*, 395(2):195–198, 1996.
- [85] Kenneth J Rothschild, Olaf Bousche, Mark S Braiman, CA Hasselbacher, and John L Spudich. Fourier transform infrared study of the halorhodopsin chloride pump. *Biochemistry*, 27(7):2420–2424, 1988.
- [86] Oleg A Sineshchekov, Elena G Govorunova, Jihong Wang, and John L Spudich. Enhancement of the long-wavelength sensitivity of optogenetic microbial rhodopsins by 3, 4-dehydroretinal. *Biochemistry*, 51(22):4499–4506, 2012.
- [87] Frank S Parker. *Applications of infrared, Raman, and resonance Raman spectroscopy in biochemistry*. Springer, 1983.
- [88] Steven O Smith, Anne B Myers, Johannes A Pardoën, Chris Winkel, Patrick PJ Mulder, Johan Lugtenburg, and Richard Mathies. Determination of retinal schiff base



- configuration in bacteriorhodopsin. *Proceedings of the National Academy of Sciences*, 81(7):2055–2059, 1984.
- [89] Tilmann Kluge, Jerzy Olejnik, Laura Smilowitz, and Kenneth J Rothschild. Conformational changes in the core structure of bacteriorhodopsin. *Biochemistry*, 37(28):10279–10285, 1998.
- [90] Kenneth J Rothschild, Mark Zagaeski, and William A Cantore. Conformational changes of bacteriorhodopsin detected by fourier transform infrared difference spectroscopy. *Biochemical and biophysical research communications*, 103(2):483–489, 1981.
- [91] Mark S Braiman, Tatsushi Mogi, Thomas Marti, Lawrence J Stern, H Gobind Khorana, and Kenneth J Rothschild. Vibrational spectroscopy of bacteriorhodopsin mutants: light-driven proton transport involves protonation changes of aspartic acid residues 85, 96, and 212. *Biochemistry*, 27(23):8516–8520, 1988.
- [92] Akio Maeda, Jun Sasaki, Yoshinori Shichida, Toru Yoshizawa, Man Chang, Baofu Ni, Richard Needleman, and Janos K Lanyi. Structures of aspartic acid-96 in the l and n intermediates of bacteriorhodopsin: analysis by fourier transform infrared spectroscopy. *Biochemistry*, 31(19):4684–4690, 1992.
- [93] Hideki Kandori. Role of internal water molecules in bacteriorhodopsin. *Biochimica et Biophysica Acta (BBA)-Bioenergetics*, 1460(1):177–191, 2000.
- [94] Wolfgang B Fischer, Sanjay Sonar, Thomas Marti, H Gobind Khorana, and Kenneth J Rothschild. Detection of a water molecule in the active-site of bacteriorhodopsin: hydrogen bonding changes during the primary photoreaction. *Biochemistry*, 33(43):12757–12762, 1994.
- [95] Hartmut Luecke, Brigitte Schobert, Hans-Thomas Richter, Jean-Philippe Cartailler, and Janos K Lanyi. Structural changes in bacteriorhodopsin during ion transport at 2 angstrom resolution. *Science*, 286(5438):255–260, 1999.

- [96] Florian Garczarek and Klaus Gerwert. Functional waters in intraprotein proton transfer monitored by ftir difference spectroscopy. *Nature*, 439(7072):109–112, 2005.
- [97] Mikihiro Shibata and Hideki Kandori. Ftir studies of internal water molecules in the schiff base region of bacteriorhodopsin. *Biochemistry*, 44(20):7406–7413, 2005.
- [98] George H Bare, James O Alben, and Philip A Bromberg. Sulfhydryl groups in hemoglobin. new molecular probe at the  $\alpha 1/\beta 1$  interface studied by fourier transform infrared spectroscopy. *Biochemistry*, 14(8):1578–1583, 1975.
- [99] Huimin Li, Charles J Wurrey, and GJ Thomas. Cysteine conformation and sulfhydryl interactions in proteins and viruses. ii. normal coordinate analysis of the cysteine side chain in model compounds. *Journal of the American Chemical Society*, 114(19):7463–7469, 1992.
- [100] Parshuram Rath, PH Bovee-Geurts, Willem J DeGrip, and Kenneth J Rothschild. Photoactivation of rhodopsin involves alterations in cysteine side chains: detection of an sh band in the meta i–i meta ii ftir difference spectrum. *Biophysical Journal*, 66(6):2085–2091, 1994.
- [101] Oleg A Sineshchekov, Elena G Govorunova, Jihong Wang, Hai Li, and John L Spudich. Intramolecular proton transfer in channelrhodopsins. *Biophysical Journal*, 104(4):807–817, 2013.
- [102] Mirka-Kristin Verhoeven, Christian Bamann, Rene Blöcher, Ute Förster, Ernst Bamberg, and Josef Wachtveitl. The photocycle of channelrhodopsin-2: Ultrafast reaction dynamics and subsequent reaction steps. *ChemPhysChem*, 11(14):3113–3122, 2010.
- [103] Frank Scholz, Ernst Bamberg, Christian Bamann, and Josef Wachtveitl. Tuning the primary reaction of channelrhodopsin-2 by imidazole, ph, and site-specific mutations. *Biophysical Journal*, 102(11):2649–2657, 2012.

- [104] Georgios Iliadis, Georg Zundel, and Bogumil Brzezinski. Aspartic proteinasesfourier transform ir studies of the aspartic carboxylic groups in the active site of pepsin. *FEBS letters*, 352(3):315–317, 1994.
- [105] John Isaac Ogren, Adrian Sonjong Yi, Sergey Mamaev, Hai Li, Johan Lugtenburg, Willem J DeGrip, John L Spudich, and Kenneth J Rothschild. Comparison of the structural changes occurring during the primary phototransition of two different channelrhodopsins from chlamydomonas algae. *Biochemistry*, 2015.
- [106] Paul Roepe, Patrick L Ahl, SK Das Gupta, Judith Herzfeld, and Kenneth J Rothschild. Tyrosine and carboxyl protonation changes in the bacteriorhodopsin photocycle. 1. m412 and l550 intermediates. *Biochemistry*, 26(21):6696–6707, 1987.
- [107] Feng Zhang, Johannes Vierock, Ofer Yizhar, Lief E Fenno, Satoshi Tsunoda, Arash Kianianmomeni, Matthias Prigge, Andre Berndt, John Cushman, Jürgen Polle, et al. The microbial opsin family of optogenetic tools. *Cell*, 147(7):1446–1457, 2011.
- [108] H Luecke, B Schobert, J P Cartailler, H T Richter, A Rosengarth, R Needleman, and J K Lanyi. Coupling photoisomerization of retinal to directional transport in bacteriorhodopsin. *Journal of Molecular Biology*, 300:1237–1255, 2000.
- [109] M K Neumann-Verhoefen, K Neumann, C Bamann, I Radu, J Heberle, E Bamberg, and J Wachtveitl. Ultrafast infrared spectroscopy on channelrhodopsin-2 reveals efficient energy transfer from the retinal chromophore to the protein. *Journal of the American Chemical Society*, 135:6968–6976, 2013.
- [110] Joel M Kralj, Vladislav B Bergo, Jason J Amsden, Elena N Spudich, John L Spudich, and Kenneth J Rothschild. Protonation state of glu142 differs in the green-and blue-absorbing variants of proteorhodopsin. *Biochemistry*, 47(11):3447–3453, 2008.
- [111] D A Doyle, Morais Cabral, J Pfuetzner, R A, A Kuo, J M Gulbis, S L Cohen, B T Chait, and R MacKinnon. The structure of the potassium channel: molecular basis of k<sup>+</sup> conduction and selectivity. *Science*, 280:69–77, 1998.

- [112] P Rath, E Spudich, D D Neal, J L Spudich, and K J Rothschild. Asp76 is the schiff base counterion and proton acceptor in the proton-translocating form of sensory rhodopsin. *Biochemistry*, 35:6690–6696, 1996.
- [113] Michael J Pettei, Anthony P Yudd, Koji Nakanishi, Robert Henselman, and Walther Stoeckenius. Identification of retinal isomers isolated from bacteriorhodopsin. *Biochemistry*, 16(9):1955–1959, 1977.
- [114] Paul D Roepe, PL Ahl, J Herzfeld, J Lugtenburg, and KJ Rothschild. Tyrosine protonation changes in bacteriorhodopsin. a fourier transform infrared study of br548 and its primary photoproduct. *Journal of Biological Chemistry*, 263(11):5110–5117, 1988.

## Curriculum Vitae

### John I. Ogren

Boston University, Physics Department  
590 Commonwealth Avenue  
Boston, Massachusetts 02215 USA

Telephone: 617-353-2600  
Facsimile: 617-353-9393  
E-mail: jiogren@bu.edu

## EDUCATION

- 2015, Ph.D. Physics, Boston University, Boston, MA, USA

Advisor: Kenneth J. Rothschild

Thesis: *Vibrational Spectroscopy of Optogenetic Rhodopsins: A Biophysical Study of Molecular Mechanisms*

- 2010, M.A. Physics, Boston University, Boston, MA, USA
- 2008, B.S. Physics, University of New Mexico, NM, USA

## RESEARCH AND TEACHING EXPERIENCE

- Jan '10 – Present, Research assistant, Boston Univ., Rothschild Molecular Biophysics Laboratory.
- Jan '11 – May '11, Associate Professor at Eastern Nazarene College, Quincy, MA; Introduction to Astronomy.
- Sep '08 – Jan '10, Teaching assistant, Boston University, Boston, MA; Introductory Physics I and II with Prof. Andrew Dufy.

## AWARDS

- 2013, BPS Educational Travel Award to attend the Biophysical Society Annual Meeting.
- 2010, Physics Department Teaching Fellow of the Year.

**COMPUTER SKILLS**

- L<sup>A</sup>T<sub>E</sub>X
- Matlab
- LabView
- Opus Spectroscopy Software
- Grams AI Spectroscopy Software

## TALKS

- May '14 Departmental Seminar, *Vibrational Studies of Optogenetic Rhodopsins: Elucidating Molecular Mechanisms*, Boston University
- Dec '12, NSF - I/UCRC Biannual Meeting FRP Presentation, Sacramento, CA.
- Apr '12 Preliminary Oral Examination *Neurophotonic Rhodopsins: Spectroscopic Characterization of Neuronal Triggers, Silencers, and in vivo Voltage Sensors*, Boston University

## POSTERS

- Feb '14, Biophysical Society 58th Annual Meeting, San Francisco, CA.
- Feb '13, Biophysical Society 57th Annual Meeting, Philadelphia, PA.
- Mar '12, American Physical Society Annual Meeting, Boston, MA.
- Feb '12, Biophysical Society 56th Annual Meeting, San Diego, CA.
- Dec '11, BU's Future of Light Symposium, Boston, MA
- Apr '11, NSF - I/UCRC Technical Forum, Boston, MA

## PUBLICATIONS

1. **John I. Ogren**, Adrian Yi, Sergey Mamaev, Hai Li, Johan Lugtenburg, Willem DeGrip, John L. Spudich, and Kenneth J. Rothschild, *Proton transfers in a Channelrhodopsin-1 studied by FTIR-Difference spectroscopy and site-directed mutagenesis*, J. Biol. Chem 2015, Mar 23; M114.634840.
2. **John .I Ogren**, Adrian Yi, Sergey Mamaev, Hai Li, Johan Lugtenburg, Willem DeGrip, John L. Spudich, and Kenneth J. Rothschild, *Comparison of Structural Changes Occurring During the Primary Phototransition of Two Different Channelrhodopsins from Chlamydomonas Alga*, Biochemistry 2015, 54; 377-388

3. **John .I Ogren**, Sergey Mamaev, Daniel Russano, Hai Li, John Spudich, Kenneth Rothschild, *Retinal Chromophore Structure and Schiff Base Interactions in Red-Shifted Channelrhodopsin-1 from Chlamydomonas augustae*, *Biochemistry*, 2014; 53(24): 3961-70
4. Bill Pedrini, et al. *7 Å resolution in protein tow-dimensional-crystal X-ray diffraction at Linac Coherent Light Source*, *Phyl. Trans. R. Soc. B* 17 July 2014; vol 369 no. 1647 20130500
5. Erica Saint Clair, **John I. Ogren**, Sergey Mamaev, Joel Kralj, Kenneth Rothschild. *Conformational changes in the archaerhodopsin-3 proton pump: detection of conserved strongly hydrogen bonded water networks*, *J Biol Phys.* 2012 Jan; 38(1): 153-68
6. Erica Saint Clair, **John I. Ogren**, Sergey Mamaev, Daniel Russano, Joel Kralj, Kenneth Rothschild. *Near-IR resonance Raman spectroscopy of archaerhodopsin-3: effects of transmembrane potential*, *J. Phys Chem B.* 2012 Dec 20; 116(50): 14592-601